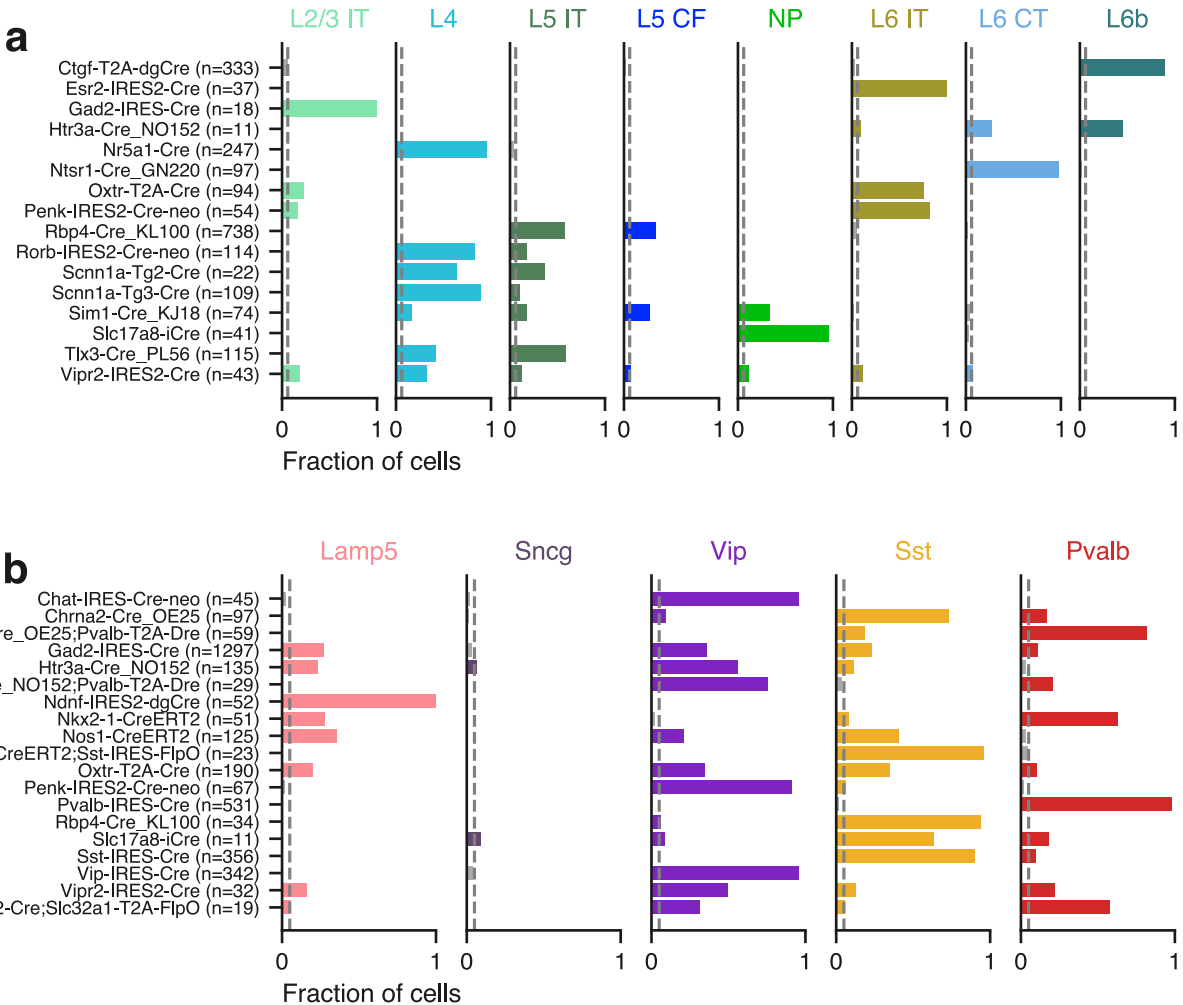


In the format provided by the authors and unedited.

# Classification of electrophysiological and morphological neuron types in the mouse visual cortex

Nathan W. Gouwens<sup>1,2</sup>, Staci A. Sorensen<sup>1,2</sup>, Jim Berg<sup>1,2</sup>, Changkyu Lee<sup>1</sup>, Tim Jarsky<sup>1</sup>, Jonathan Ting<sup>1</sup>, Susan M. Sunkin<sup>1</sup>, David Feng<sup>1</sup>, Costas A. Anastassiou<sup>1</sup>, Eliza Barkan<sup>1</sup>, Kris Bickley<sup>1</sup>, Nicole Blesie<sup>1</sup>, Thomas Braun<sup>1</sup>, Krissy Brouner<sup>1</sup>, Agata Budzillo<sup>1</sup>, Shiella Caldejon<sup>1</sup>, Tamara Casper<sup>1</sup>, Dan Castelli<sup>1</sup>, Peter Chong<sup>1</sup>, Kirsten Crichton<sup>1</sup>, Christine Cuhaciyan<sup>1</sup>, Tanya L. Daigle<sup>1</sup>, Rachel Dalley<sup>1</sup>, Nick Dee<sup>1</sup>, Tsega Desta<sup>1</sup>, Song-Lin Ding<sup>1</sup>, Samuel Dingman<sup>1</sup>, Alyse Doperalski<sup>1</sup>, Nadezhda Dotson<sup>1</sup>, Tom Egdorf<sup>1</sup>, Michael Fisher<sup>1</sup>, Rebecca A. de Frates<sup>1</sup>, Emma Garren<sup>1</sup>, Marissa Garwood<sup>1</sup>, Amanda Gary<sup>1</sup>, Nathalie Gaudreault<sup>1</sup>, Keith Godfrey<sup>1</sup>, Melissa Gorham<sup>1</sup>, Hong Gu<sup>1</sup>, Caroline Habel<sup>1</sup>, Kristen Hadley<sup>1</sup>, James Harrington<sup>1</sup>, Julie A. Harris<sup>1</sup>, Alex Henry<sup>1</sup>, DiJon Hill<sup>1</sup>, Sam Josephsen<sup>1</sup>, Sara Kebede<sup>1</sup>, Lisa Kim<sup>1</sup>, Matthew Kroll<sup>1</sup>, Brian Lee<sup>1</sup>, Tracy Lemon<sup>1</sup>, Katherine E. Link<sup>1</sup>, Xiaoxiao Liu<sup>1</sup>, Brian Long<sup>1</sup>, Rusty Mann<sup>1</sup>, Medea McGraw<sup>1</sup>, Stefan Mihalas<sup>1</sup>, Alice Mukora<sup>1</sup>, Gabe J. Murphy<sup>1</sup>, Lindsay Ng<sup>1</sup>, Kiet Ngo<sup>1</sup>, Thuc Nghi Nguyen<sup>1</sup>, Philip R. Nicovich<sup>1</sup>, Aaron Oldre<sup>1</sup>, Daniel Park<sup>1</sup>, Sheana Parry<sup>1</sup>, Jed Perkins<sup>1</sup>, Lydia Potekhina<sup>1</sup>, David Reid<sup>1</sup>, Miranda Robertson<sup>1</sup>, David Sandman<sup>1</sup>, Martin Schroedter<sup>1</sup>, Cliff Slaughterbeck<sup>1</sup>, Gilberto Soler-Llavina<sup>1</sup>, Josef Sulc<sup>1</sup>, Aaron Szafer<sup>1</sup>, Bosiljka Tasic<sup>1</sup>, Naz Taskin<sup>1</sup>, Corinne Teeter<sup>1</sup>, Nivretta Thatra<sup>1</sup>, Herman Tung<sup>1</sup>, Wayne Wakeman<sup>1</sup>, Grace Williams<sup>1</sup>, Rob Young<sup>1</sup>, Zhi Zhou<sup>1</sup>, Colin Farrell<sup>1</sup>, Hanchuan Peng<sup>1</sup>, Michael J. Hawrylycz<sup>1</sup>, Ed Lein<sup>1</sup>, Lydia Ng<sup>1</sup>, Anton Arkhipov<sup>1</sup>, Amy Bernard<sup>1</sup>, John W. Phillips<sup>1</sup>, Hongkui Zeng<sup>1\*</sup> and Christof Koch<sup>1</sup>

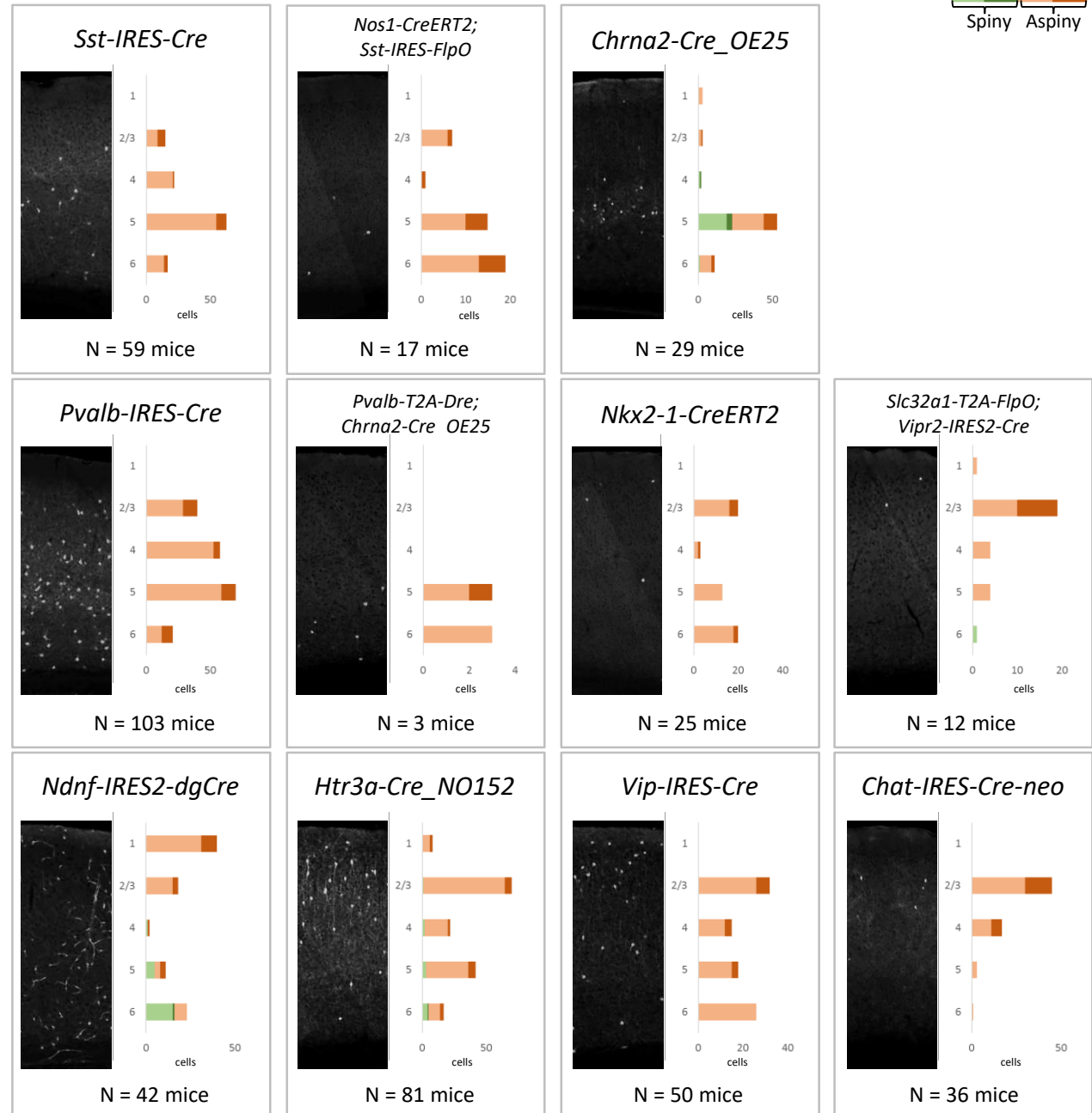
<sup>1</sup>Allen Institute for Brain Science, Seattle, Washington, USA. <sup>2</sup>These authors contributed equally: Nathan W. Gouwens, Staci A. Sorensen, Jim Berg.  
\*e-mail: [hongkuiz@alleninstitute.org](mailto:hongkuiz@alleninstitute.org)



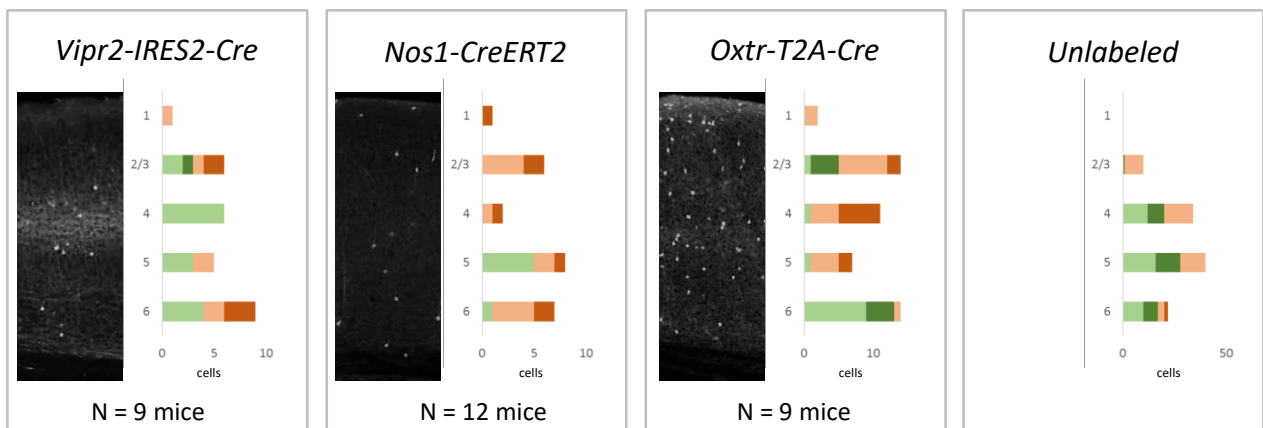
**Supplementary Figure 1:** Transgenic line-based sampling strategy. Based on FACS data contained in Tasic et. al<sup>1</sup>, expression pattern of different transgenic lines. Numbers in the figure are the number of cells from that study. Transgenic lines are shown that were both used in this study and also had at least 10 FACS cells classified in either excitatory or inhibitory classes. Transgenic lines were considered to be consistent with a given transcriptomic subclass (colored bars) if at least 5% of FACS cells (dotted vertical lines) were in that subclass. **(a)** Expression patterns across excitatory transcriptomic subclasses for transgenic lines used in this study. Excitatory-dominant lines tended to be more selective and were enriched in specific cortical layers. IT: intratelencephalic, CF: corticofugal, NP: near-projecting, CT: corticothalamic. **(b)** Expression patterns across inhibitory transcriptomic subclasses for transgenic lines used in this study. Broad lines (e.g. *Htr3a-Cre\_NO152*, *Sst-IRES-Cre*, *Pvalb-IRES-Cre*) were chosen to cover the majority of inhibitory transcriptomic types in VISp. Additional lines were chosen to fill in missing types and to label specific types more selectively.

## a. Inhibitory Cre line sampling

Somatostatin family  
Parvalbumin family  
5Htr3Ar family



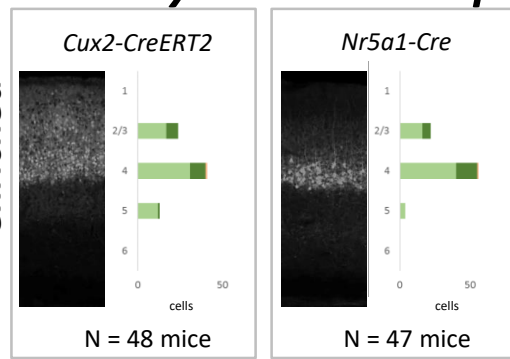
## b. Cre lines with mixed expression, Unlabeled cells



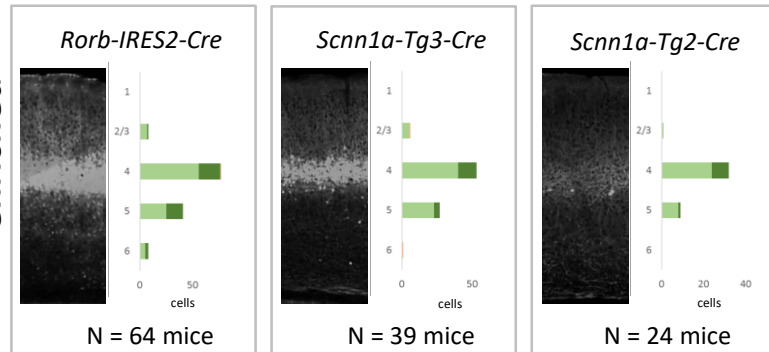
### c. Excitatory Cre line sampling

Reconstructed? N Y N Y  
Spiny Aspyny

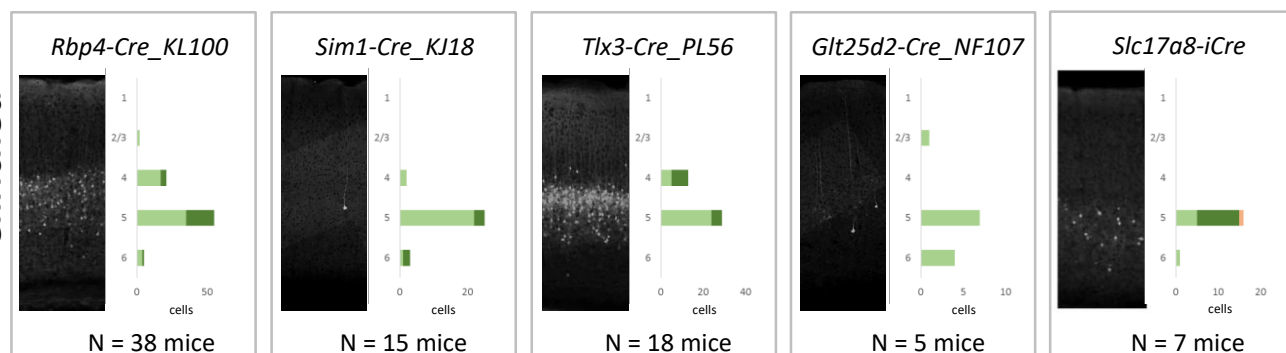
Layers 2/3, 4  
enriched



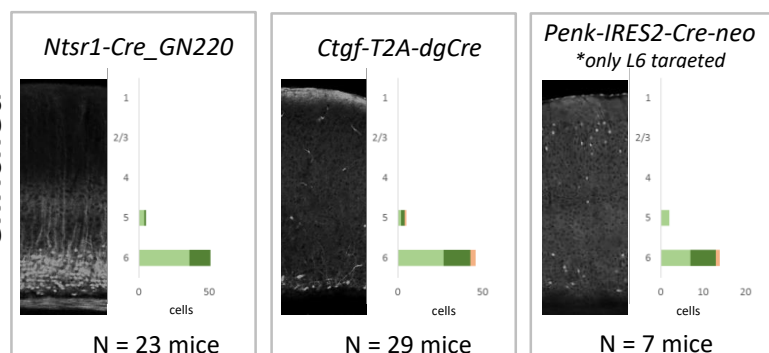
Layer 4, 5  
enriched



Layer 5  
enriched



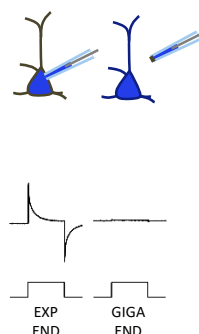
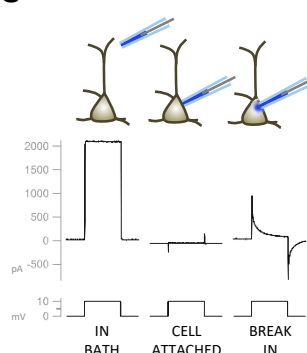
Layer 6  
enriched



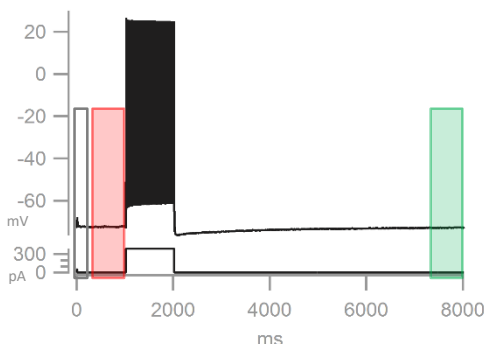
### d. Additional lines

	mice	Cells	Reconstructions
Gad2-IRES-Cre	9	19	3
Gng7-Cre_KH71	1	1	0
PhiC31-neo;Esr2-IRES2-Cre	2	4	1
Pvalb-T2A-CreERT2	2	3	0
Pvalb-T2A-Dre;Htr3a-Cre_NO152	5	10	3
Pvalb-T2A-FlpO;Vipr2-IRES2-Cre	1	2	2
Slc17a6-IRES2-FlpO;Penk-IRES2-Cre-neo	2	2	2
Slc17a6-IRES-Cre	1	3	2
Slc17a8-IRES2-Cre	1	1	0

**Supplementary Figure 2: Sampling results per transgenic line.** **(a), (b), and (c)** A summary of the layer distribution of cells recorded from each inhibitory (a), mixed (b), and excitatory (c) transgenic line. For each transgenic line: *Left*, 2-photon composite image of coronal slice of VISp showing distribution of fluorescent neurons. Images were obtained and processed as described in Oh et al.<sup>2</sup> *Column 2*, Stacked histogram of spiny (green) and aspiny (brown) cells sampled. Darker bars indicate those cells that were also morphologically reconstructed. Total number of mice used per line indicated below. **(d)** Table of mice, cells, and reconstructions from additional lines that contributed small amounts of data to the study.

**a. Cell – level QC**
**Voltage clamp experiment metadata**  
**'Test Pulses'**
**QC criteria**

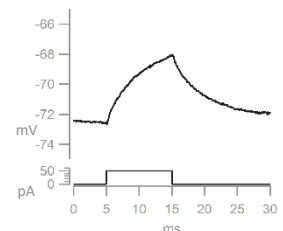
- Electrode must be 'zeroed' before recording.
- A  $\text{G}\Omega$  seal must have been reached prior to break-in.
- Initial access resistance must be  $< 20 \text{ M}\Omega$  and  $< 15\%$  of the  $R_{\text{input}}$ .
- Electrode drift: The final voltage recording must be within 1 mV of the original voltage for every 10 minutes of data recording.

**b. Sweep – level QC****Pre-stimulus (red)**

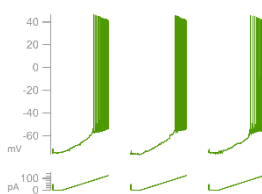
- Bridge balance:  $< 20 \text{ M}\Omega$  and 15% of the  $R_{\text{input}}$
- Bias current:  $0 \pm 100 \text{ pA}$
- High frequency noise/patch instability: RMS noise in 1.5 ms and 500 ms windows  $< 0.07 \text{ mV}$  and  $0.5 \text{ mV}$ , respectively

**Post-stimulus (green)**

- $V_m$  within 1 mV of pre- $V_m$

**Standard 'test pulse'****c. A typical electrophysiology experiment**

- Current clamp stimuli and responses from specimen 557252022 (same cell featured in Fig1).
- Full dataset (including a .nwb raw electrophysiology file detailing the comprehensive stimuli and responses for each cell) is publicly available at: <http://celltypes.brain-map.org/experiment/electrophysiology/557252022>
- Additional methods details available in the form of technical white papers can also be found under 'Documentation' at <http://celltypes.brain-map.org>

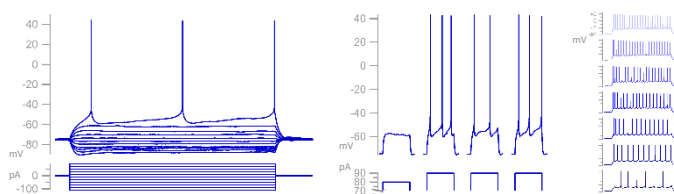
**Ramp Stimulus**

Current injection of increasing intensity at a rate much slower than neuron's time constant.

Details: Ramp of 25 pA per 1 second, terminated after a series of APs are acquired.

Typical order: First

Repeats: 3

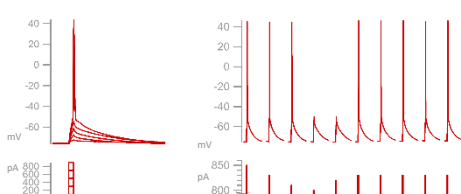
**Long Square Stimulus**

Square pulse of a duration to allow the neuron to come to steady-state.

Details: 1 s current injections from  $-110 \text{ pA}$  to  $+160 \text{ pA}$ , in  $20 \text{ pA}$  increments.

Typical order: Third

Repeats: Single sweep for each sub / suprathreshold pulse,  $\geq 3$  sweeps at rheobase

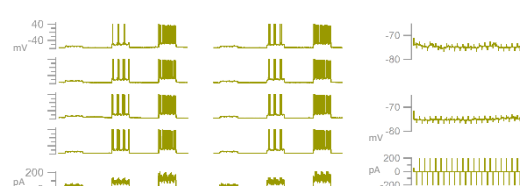
**Short Square Stimulus**

Square pulse brief enough to elicit a single action potential.

Details: 3 ms current injections used to find the action potential threshold within 10 pA.

Typical order: Second

Repeats:  $\geq 3$  sweeps at threshold

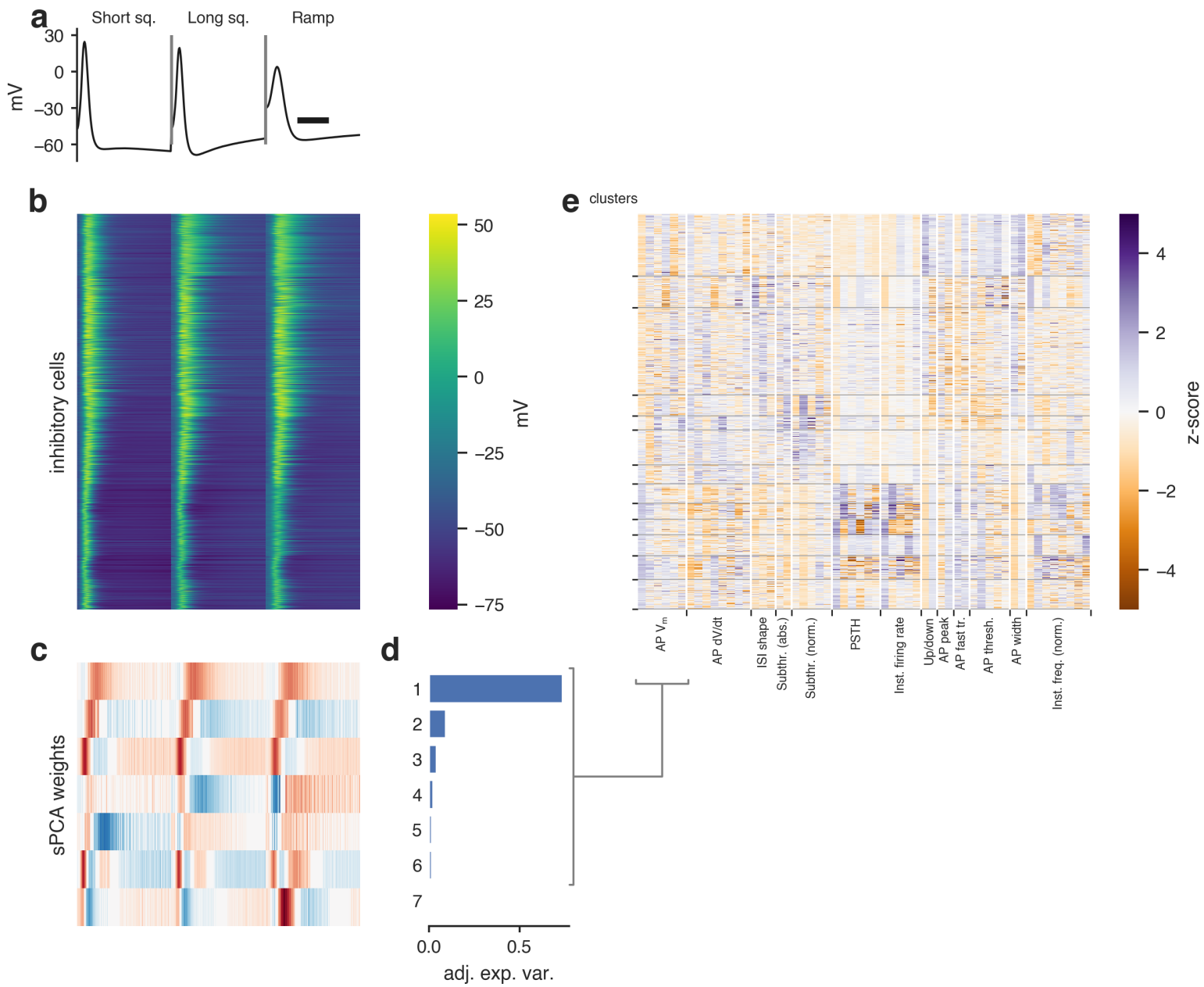
**Additional stimuli (not used in ephys type clustering)**

The cell is stimulated with additional pulses to support single cell modeling studies.

See Teeter et al., Nat Commun. 2018 Feb 19;9(1):709 and

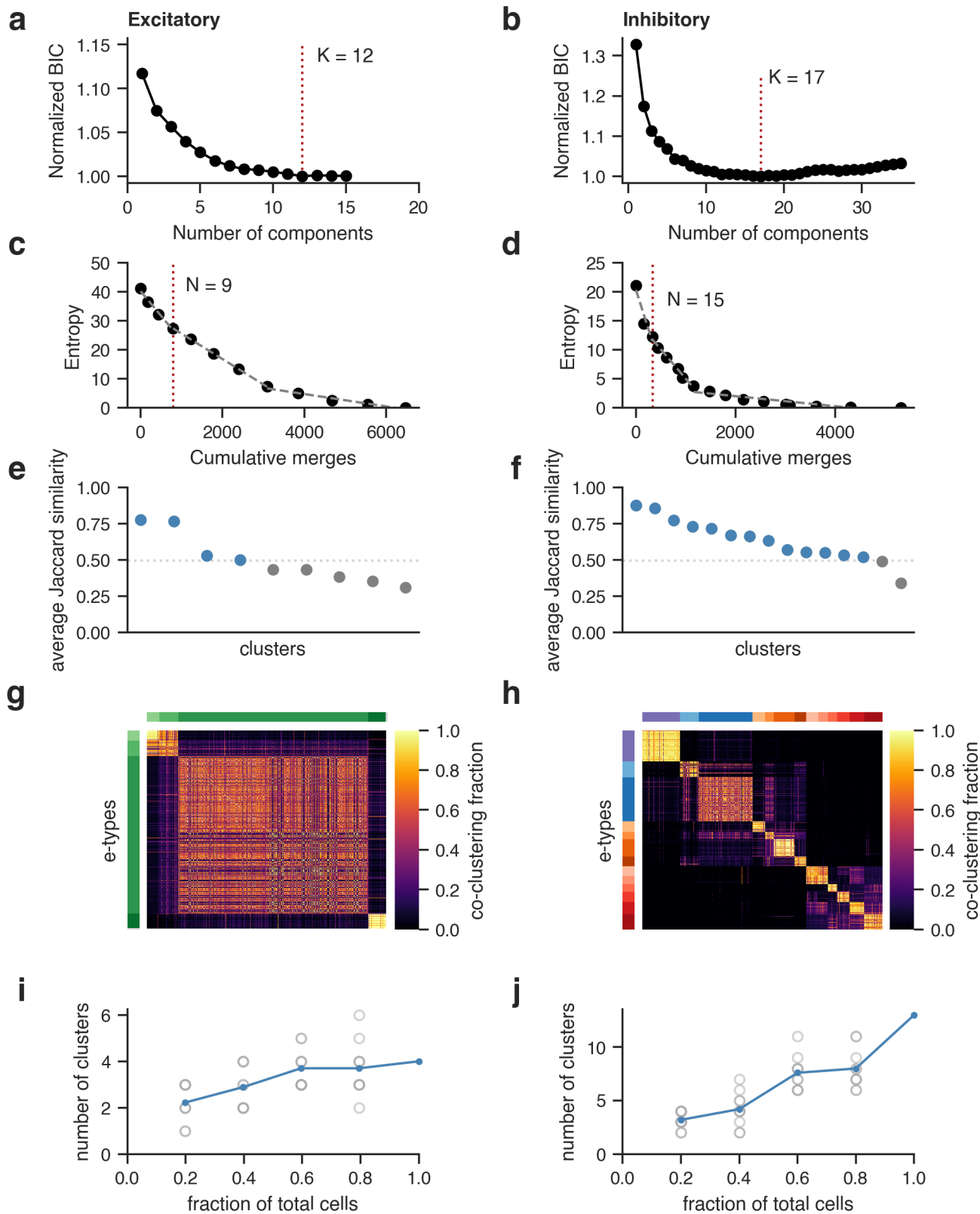
Gouwens et al., Nat Commun. 2018 Feb 19;9(1):710

**Supplementary Figure 3: Electrophysiology quality control and stimuli.** (a) Metadata voltage clamp test pulses were delivered at specific points during the experiment to assist in evaluating data quality. Each cell was subject to a number of gates to insure stable quality recordings. (b) Sweeps were manually inspected for artifacts and for correct bridge balance settings using a short standard test pulse preceding the stimulus. In addition, poor quality sweeps were automatically rejected from analysis using a series of criteria before and after the stimulus. (c) The electrophysiology properties of each cell were probed using standard stimuli: long and short square steps, as well as a ramp current injection.

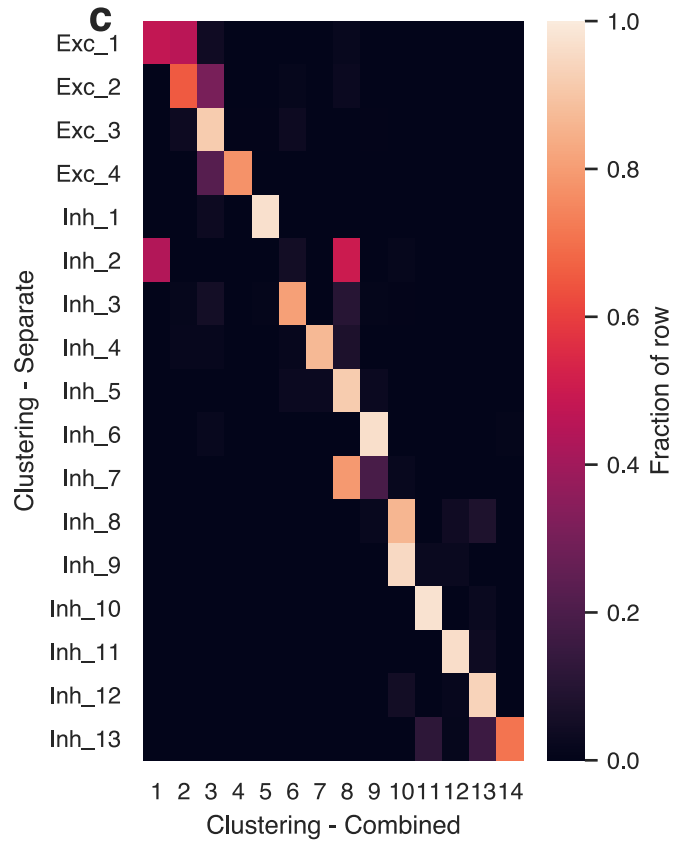
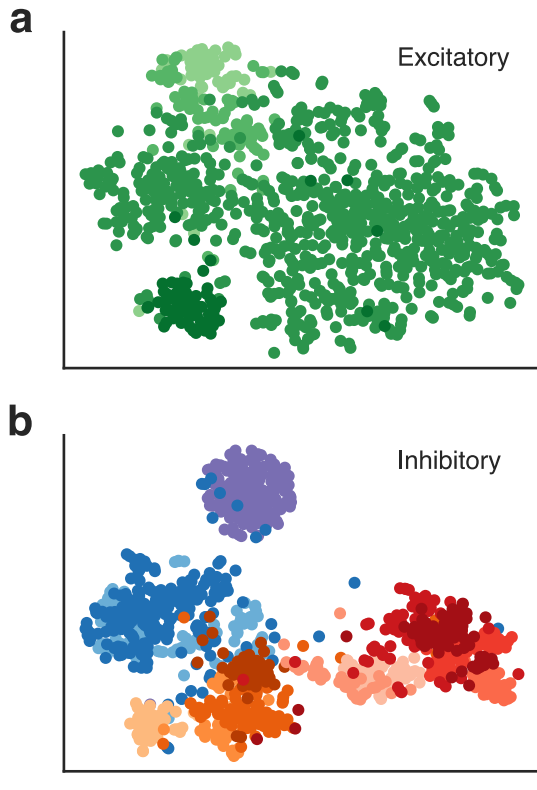


**Supplementary Figure 4:** Electrophysiology dimensionality reduction. **(a)** Example action potential waveforms of an example cell evoked by a short (3 ms) current pulse, a long square (one second) current step, and a slow current ramp (25 pA/s). **(b)** Heat map of all action potential waveforms from inhibitory cells ( $n = 1,010$  cells). **(c)** Sparse principal component weights of the data in **(b)**. Time scale is the same in **(a-c)**. **(d)** Adjusted explained variances of sparse principal components shown in **(c)**. **(e)** Sparse principal component values collected from each data type, indicated by labels at the bottom. For example, the seven sparse principal components obtained from the action potential waveforms populate the first seven columns of the matrix in **(d)**. Component values were transformed into a z-score. Rows are sorted into clusters indicated by left tick marks (Methods).

**Supplementary Figure 5**



**Supplementary Figure 5: Merging GMM components and cluster stability.** (a-b) Bayesian information criteria (BIC) values (normalized to the minimum) for Gaussian mixture models fit using the excitatory (a) and inhibitory (b) neuron data with different numbers of components. The model with the lowest BIC ( $K = 12$  components in (a),  $K = 17$  components in (b)) was selected as the best representation of the data. (c-d) Entropy as Gaussian mixture model components were merged, plotted against the cumulative number of samples merged. Merging was stopped when the rate of entropy decrease slowed (excitatory:  $N = 9$  clusters in (c); inhibitory:  $N = 15$  clusters in (d)), determined by the first change point of a three-part piecewise linear fit (Methods). (e-f) Average Jaccard similarities determined by repeating the clustering procedure on 100 90% subsamples for excitatory (e) and inhibitory (f) cells. Clusters with similarities below 0.5 (dotted line) were deemed unstable (gray) and merged into other clusters (blue). (g-h) Pairwise co-clustering results for excitatory (e) and inhibitory (f) cells. 100 random subsamples containing 90% of the data were generated and clustered by GMM fit, merging, and stability analysis. Heatmap shows the fraction of times a given pair of cells were in the same cluster. Cells are ordered by e-types determined from the full data set, indicated by row and column colors. (i-j) Number of clusters resulting from the described procedure performed on subsamples of 20%, 40%, 60%, and 80% of the data (10 repeats each, open circles) for excitatory (i) and inhibitory (j) cells. Average cluster numbers indicated by the connected line. Note that only discrete integer cluster numbers are possible for individual runs, so points are partially transparent to indicate when they are overplotted.



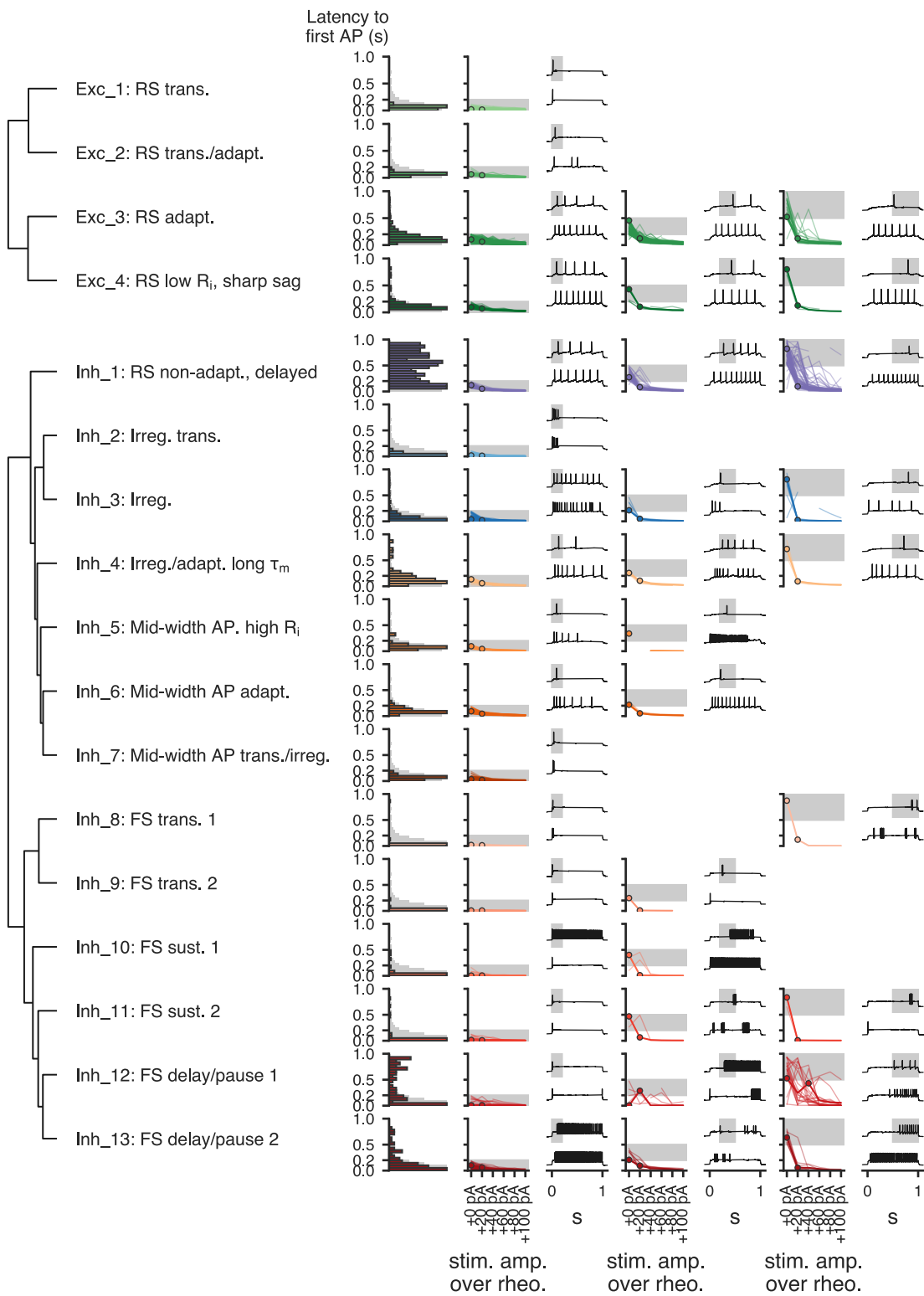
**Supplementary Figure 6:** Comparison of separate and combined electrophysiology clustering analyses. **(a)** t-SNE projection of electrophysiological data from only excitatory (spiny) neurons ( $n = 928$  cells). Colors indicate excitatory e-types (see Fig. 2). **(b)** t-SNE projection of electrophysiological data from only inhibitory (aspiny) neurons ( $n = 1,010$  cells). Colors indicate inhibitory e-types. **(c)** Comparison of e-types obtained by separate analyses of excitatory and inhibitory neurons (rows) and a combined analysis of all cells together (columns).

**Supplementary Figure 7**



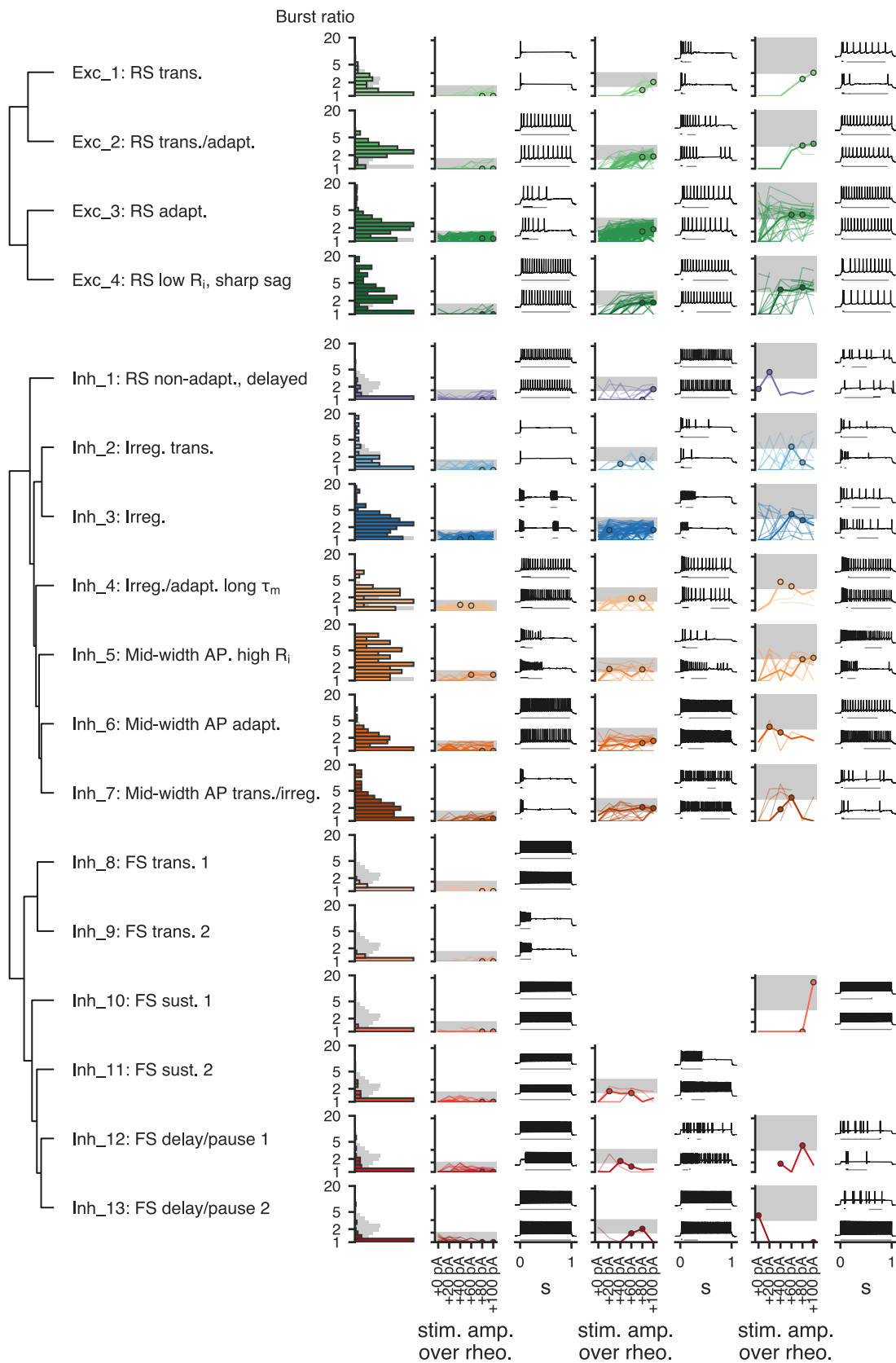
**Supplementary Figure 7: Transgenic lines on the electrophysiological projection.**

Electrophysiology-based t-SNE plots ( $n = 1,938$  cells) with cells from different transgenic lines highlighted. Colors indicate electrophysiological cluster labels (see Fig. 2). Cells that were fluorescent-reporter positive with a given transgenic driver are indicated with black circles.



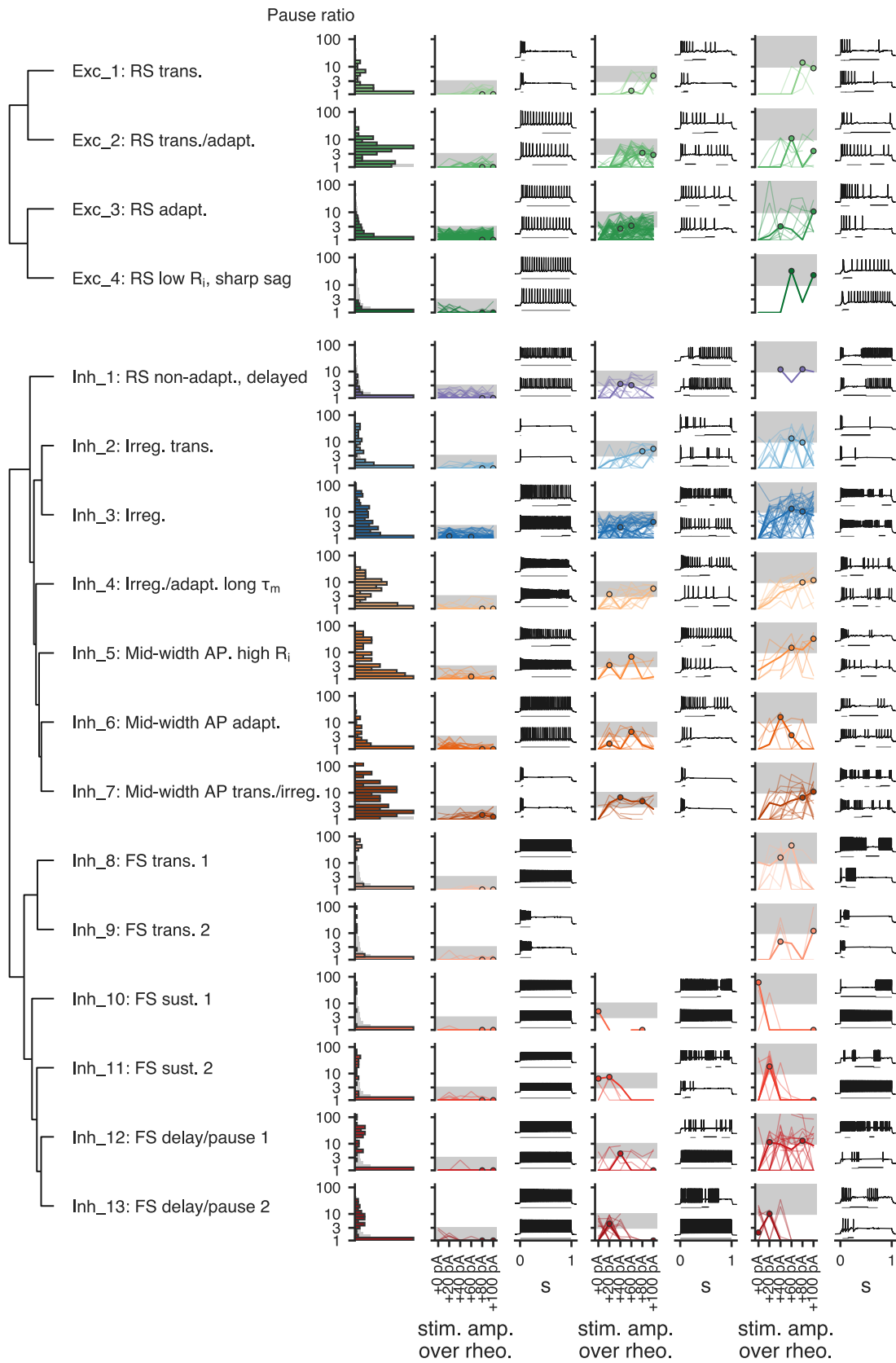
**Supplementary Figure 8:** Latency to first action potential. Each row presents information from a different electrophysiological cluster. Dendrogram on left based on distances between cluster centroids (see Fig. 2). Histogram shows the maximum latency to the first spike observed per cell across six long square current steps (from rheobase to rheobase + 100 pA). Gray histogram is all cells, colored histograms are cells of that cluster. Histograms are normalized to their maximum values. On the right, cells in each cluster have been divided into groups based on their maximum latency: 0 s to 0.2 s, 0.2 s to 0.5 s, and 0.5 to 1 s (indicated by shaded regions on line plots and upper example traces). Line plots show how the latency per sweep changes as the stimulus amplitude is varied. Example traces show a representative cell for each cluster/category combination; upper trace is the one with the longest latency from a cell, lower trace is the next longest from the same cell. Selected examples are indicated on the line plots by thicker lines and circles.

**Supplementary Figure 9**

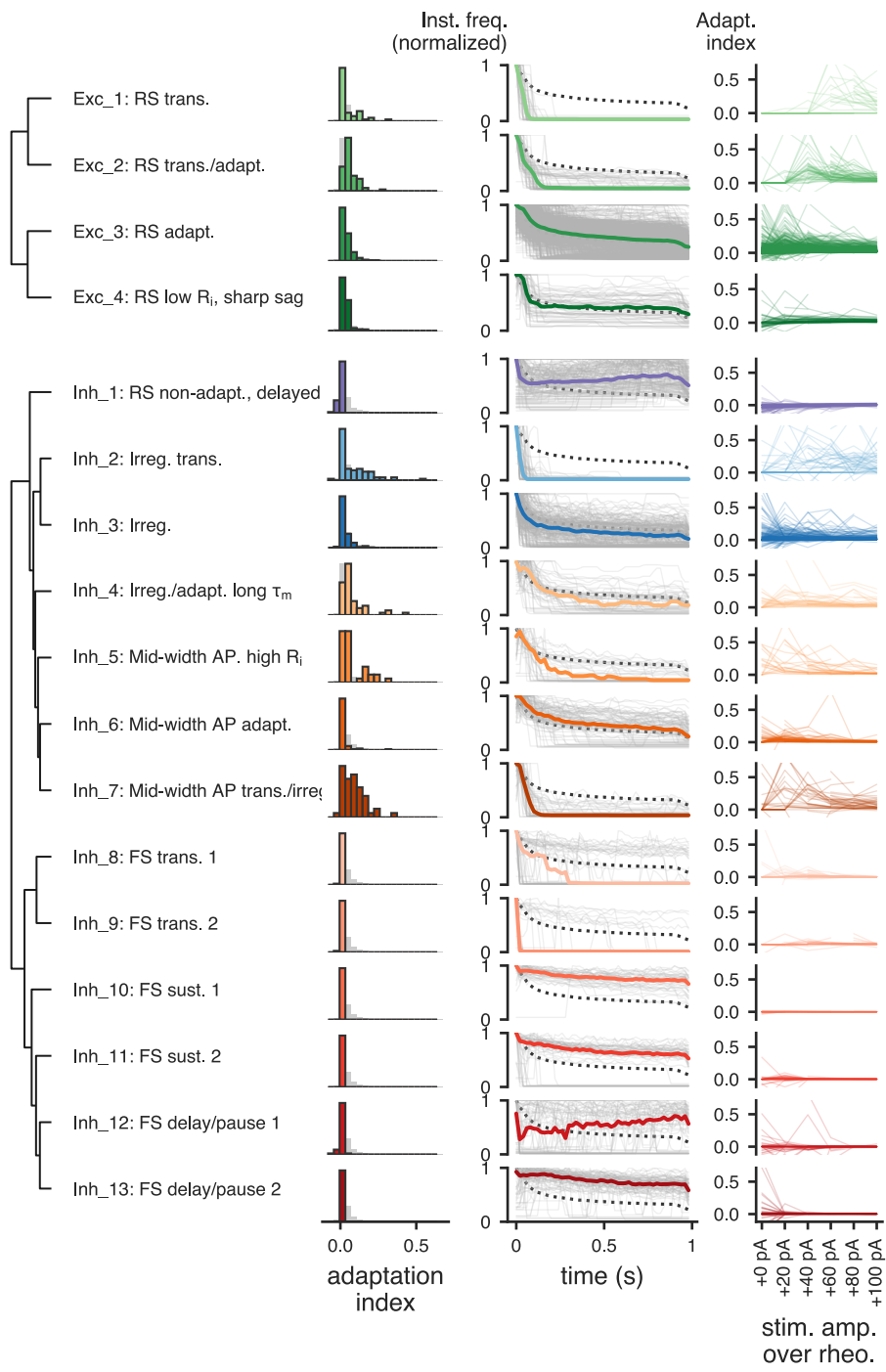


**Supplementary Figure 9: Bursting firing patterns.** Each row presents information from a different electrophysiological cluster. Dendrogram on left based on distances between cluster centroids (see Fig. 2). Histogram shows the maximum burst ratio observed per cell across six long square current steps (from rheobase to rheobase + 100 pA). The burst ratio is defined as the firing rate of the fastest segment divided by the firing rate of the segment(s) with the most action potentials (Methods); the median across segments was used for the latter in the case of ties. Gray histogram is all cells, colored histograms are cells of that cluster. Histograms are normalized to their maximum values. On the right, cells in each cluster have been divided into groups based on their maximum burst ratio: 1 to 2, 2 to 5, and 5 or more (indicated by shaded regions on line plots). Line plots show how the maximum burst ratio per sweep changes as the stimulus amplitude is varied. Example traces show a representative cell for each cluster/category combination; upper trace is the one with the highest burst ratio, lower trace is the next highest from the same cell. Lines underneath the traces indicate the segment with highest firing rate (black) and the segment(s) with the most action potentials (gray). Selected examples are indicated on the line plots by thicker lines and circles.

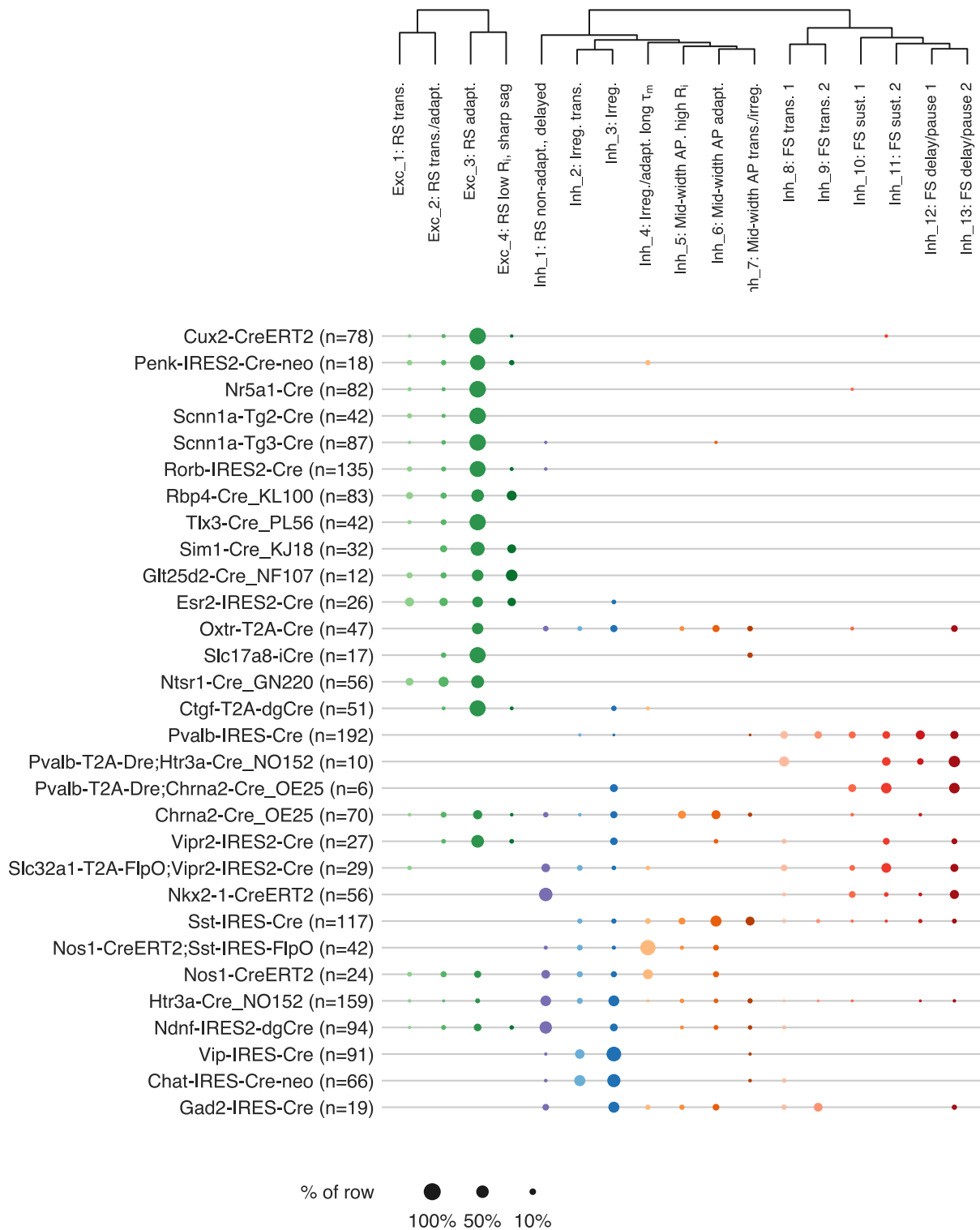
Supplementary Figure 10



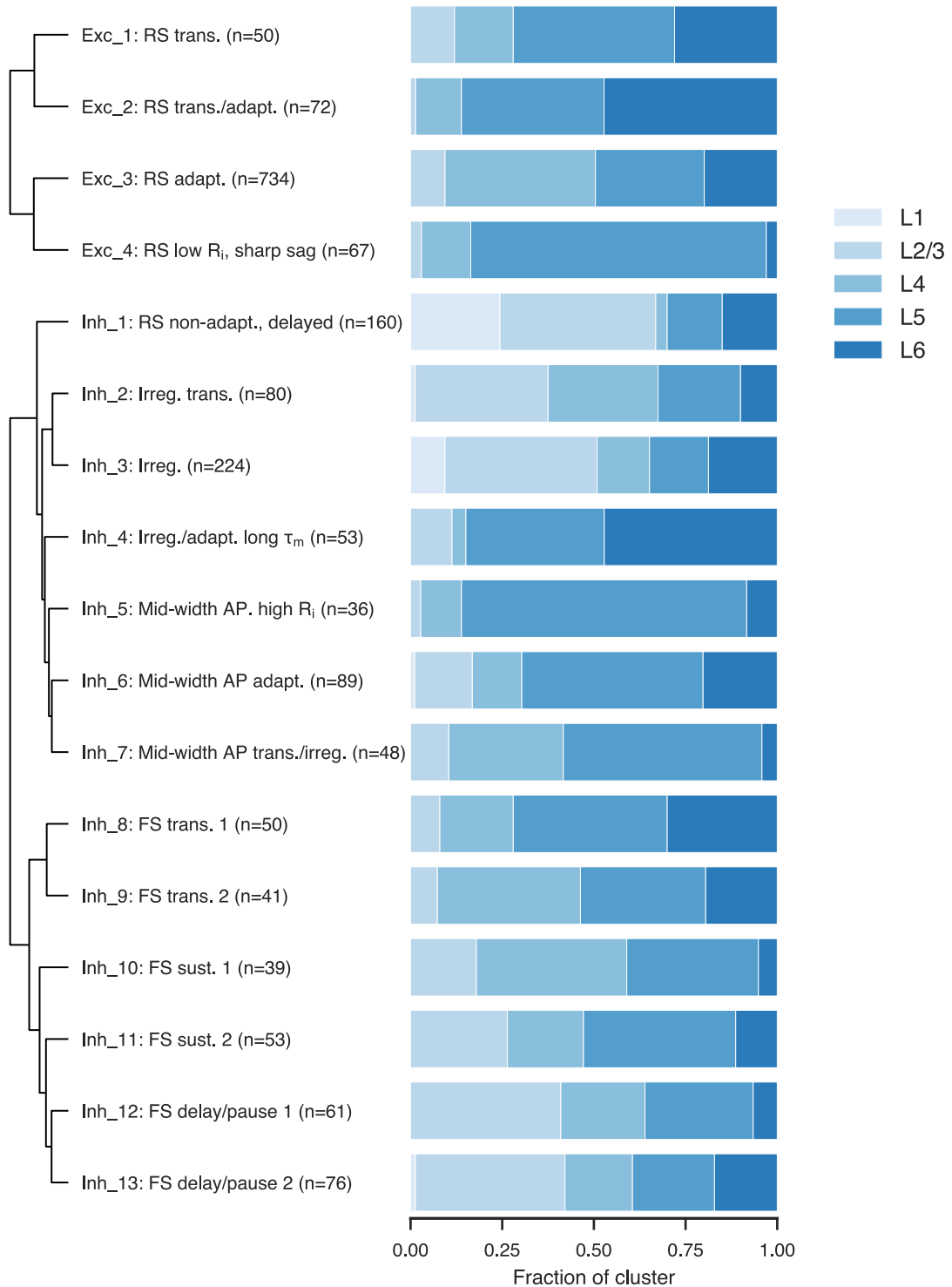
**Supplementary Figure 10: Pausing firing patterns.** Each row presents information from a different electrophysiological cluster. Dendrogram on left based on distances between cluster centroids (see Fig. 2). Histogram shows the maximum pause ratio observed per cell across six long square current steps (from rheobase to rheobase + 100 pA). The pause ratio is defined as the average interspike interval duration of the segment with the slowest firing divided by the average interspike interval of the segment(s) with the most action potentials (Methods); the median across segments was used for the latter in the case of ties. Gray histogram is all cells, colored histograms are cells of that cluster. Histograms are normalized to their maximum values. On the right, cells in each cluster have been divided into groups based on their maximum pause ratio: 1 to 3, 3 to 10, and 10 or more (indicated by shaded regions on line plots). Line plots show how the maximum pause ratio per sweep changes as the stimulus amplitude is varied. Example traces show a representative cell for each cluster/category combination; upper trace is the one with the highest pause ratio, lower trace is the next highest from the same cell. Lines underneath the traces indicate the segment with highest firing rate (black) and the segment(s) with the most action potentials (gray). Selected examples are indicated on the line plots by thicker lines and circles.



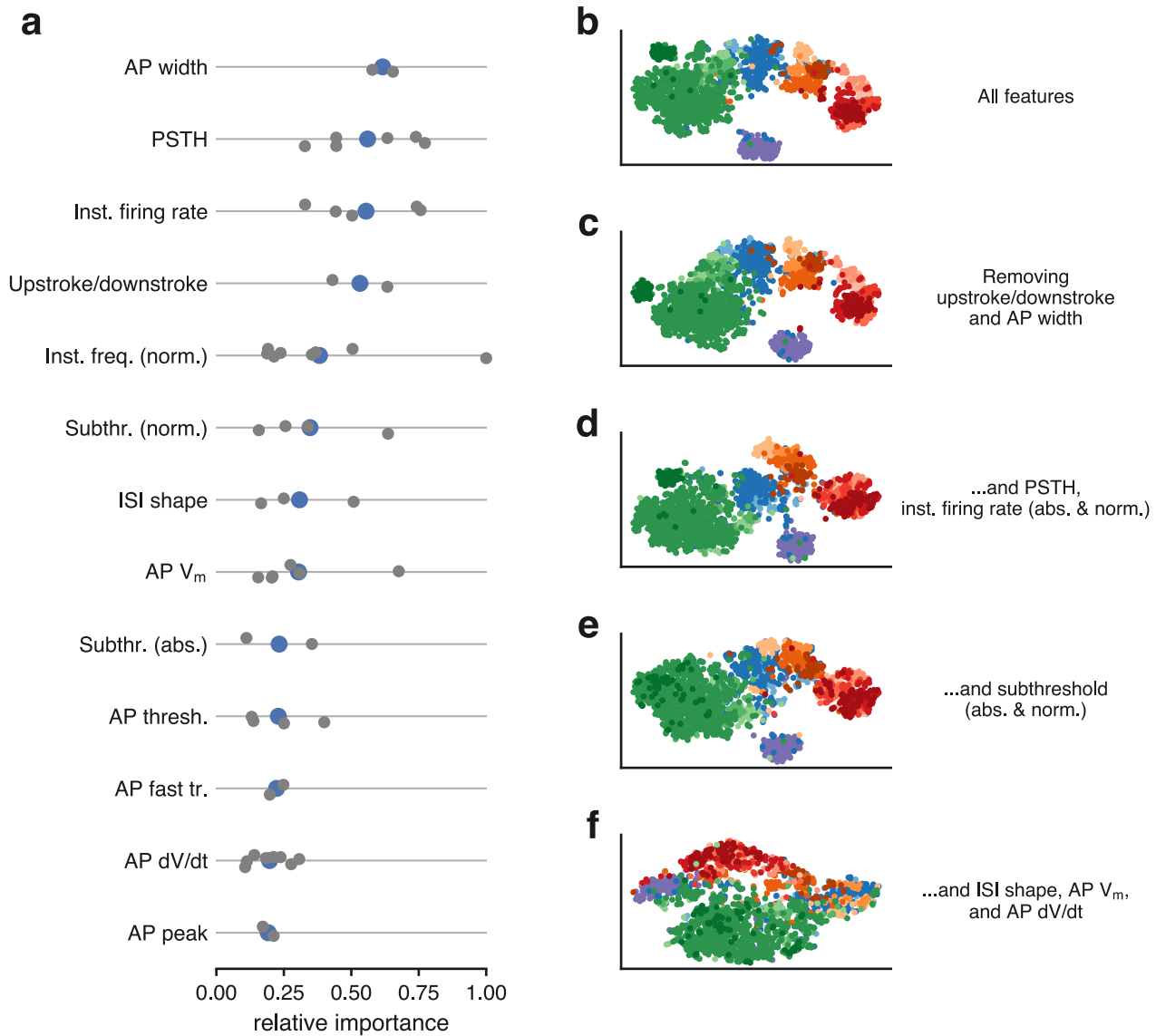
**Supplementary Figure 11: Firing frequency adaptation.** Each row presents information from a different electrophysiological cluster. Dendrogram on left based on distances between cluster centroids (see Fig. 2). Histogram shows the median adaptation index observed per cell across six long square current steps (from rheobase to rheobase + 100 pA). Center plots show the firing rates (calculated in 20 ms bins) from the sweep at the median adaptation index, normalized to the highest firing rate of the sweep. All cells from the cluster are shown as gray lines, the cluster medians are shown as the thick colored lines, and the grand median across all cells is shown as a dotted line. Note that the non-monotonic median of Inh\_4 is due to many cells in that cluster exhibiting pauses in firing (where the instantaneous firing rate falls to zero) toward the start of the stimulus period. Right plots show how the adaptation index varied across six long square current steps (from rheobase to rheobase + 100 pA).



**Supplementary Figure 12:** Transgenic lines and e-types. Fraction of cells from each transgenic line examined (rows) that fall into each e-type (columns). Dot size indicates the fraction of the row falling into a given column, and color indicates e-type.

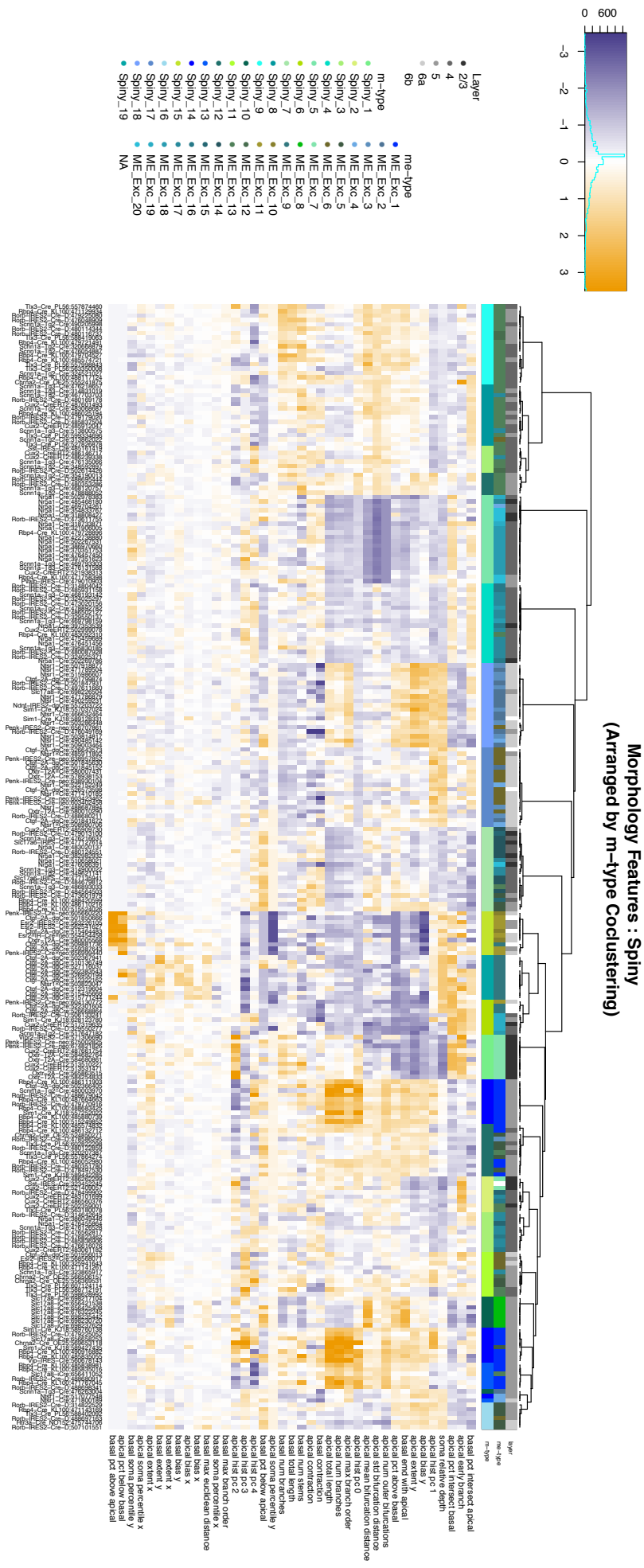


**Supplementary Figure 13: Cortical layer distribution of e-types.** Distribution of cells from each e-type across the cortical layers.



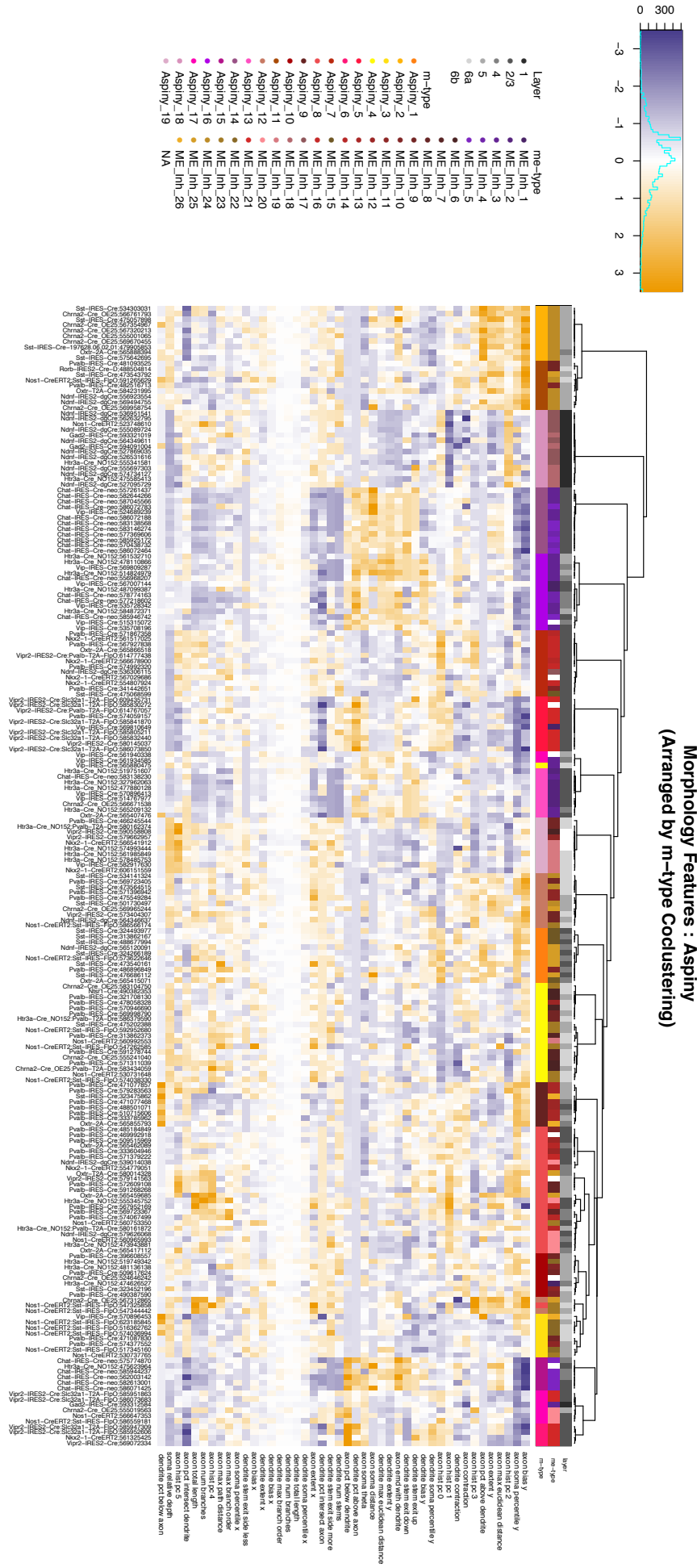
**Supplementary Figure 14:** Electrophysiology feature importance. **(a)** Relative feature importances of electrophysiological features as determined by a random-forest classifier. Gray dots are importances of individual components from each feature set, and blue circles are averages. Importances are scaled to the highest value across all components. **(b-f)** t-SNE projections ( $n = 1,938$  cells) based on the full electrophysiological feature matrix **(b)** and subsets of that matrix as additional features are removed. Removing the feature sets with highest average importance in **(a)** (AP width and upstroke/downstroke ratio) had relatively little effect on the projection **(c)**, and removing additional features first mixed various fast-spiking e-types **(d)**, then the e-types associated with *Vip* and *Sst* cells, as well as excitatory cells **(e)**. The overall structure, though, was maintained until most features were removed **(f)**.

## Supplementary Figure 15



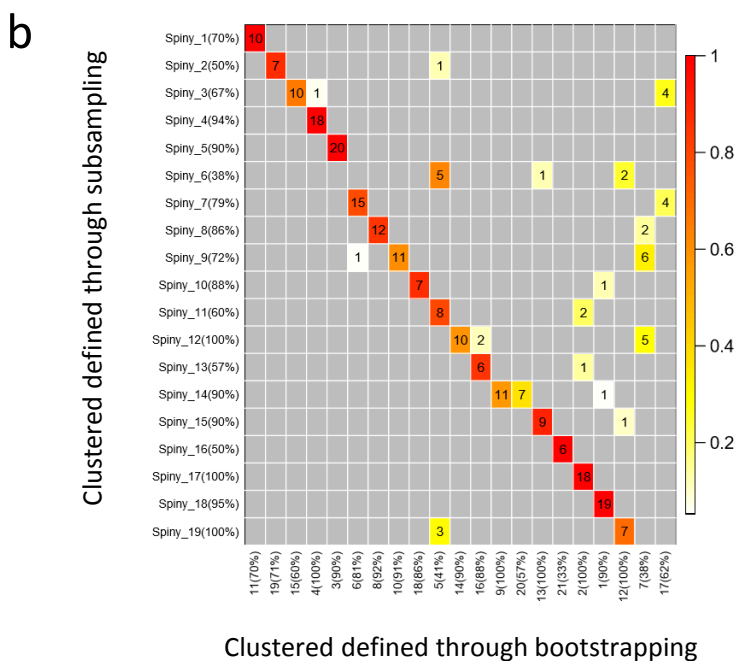
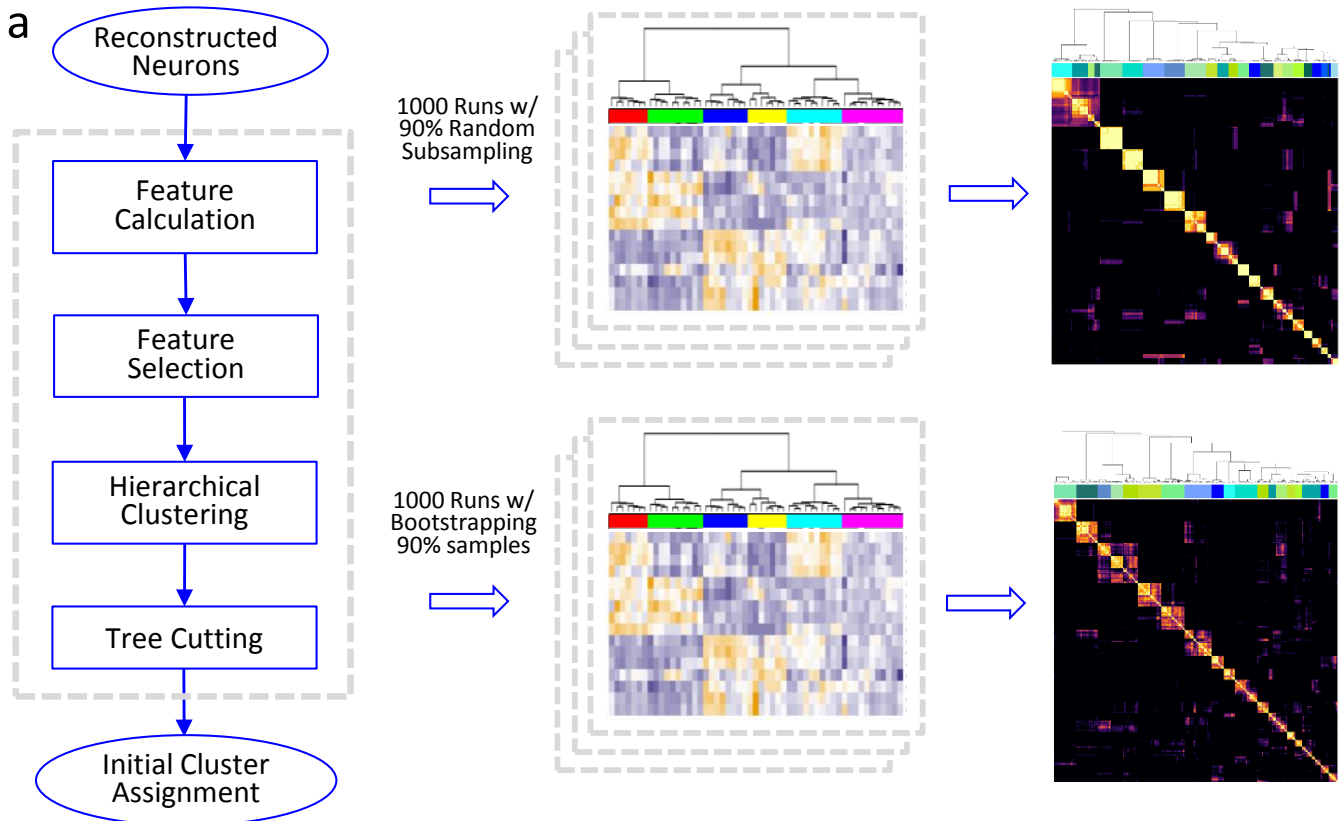
**Supplementary Figure 15: Spiny feature heatmap and dendrogram.** Dendrogram generated by hierarchical clustering with Ward's agglomeration method using Euclidean distances in the high-dimensional feature space. 19 spiny m-types are indicated by the m-type-specific color bar. Layer is also indicated by the gray-scale color bar. Heatmap shows values for 39 morphological features by m-type. Features were first converted to z-scores for the analysis.

## Supplementary Figure 16

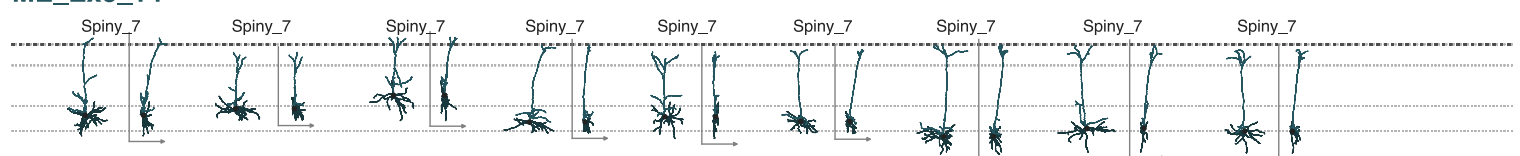
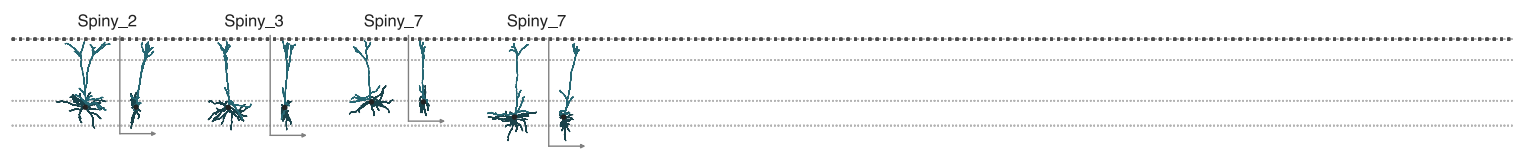
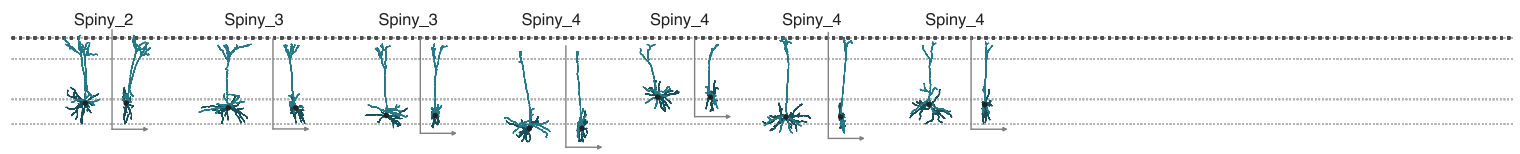
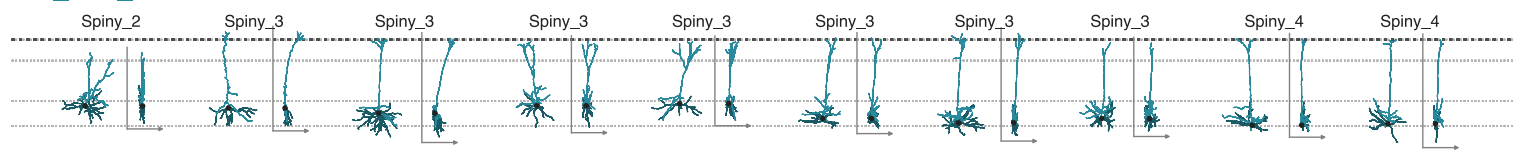
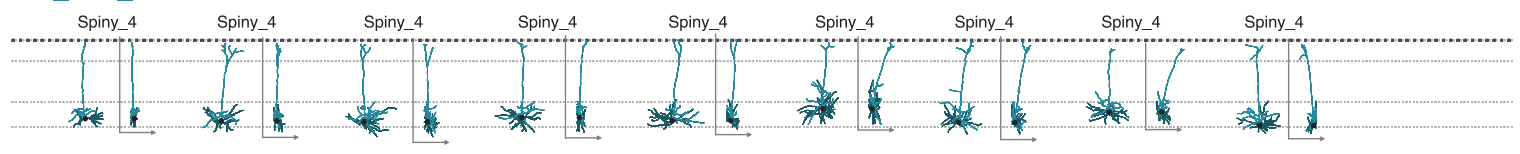


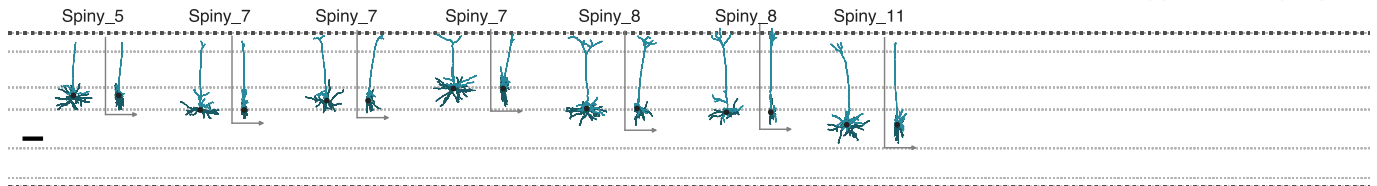
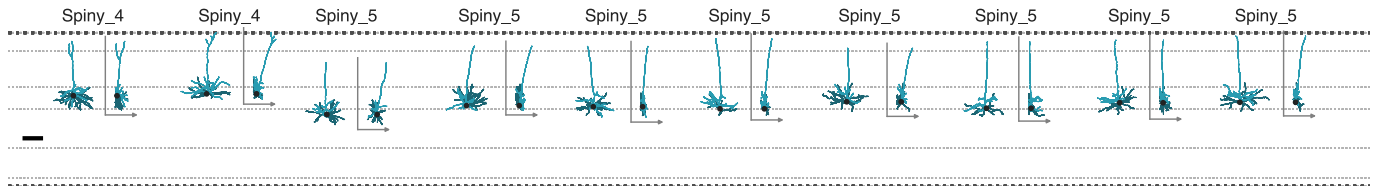
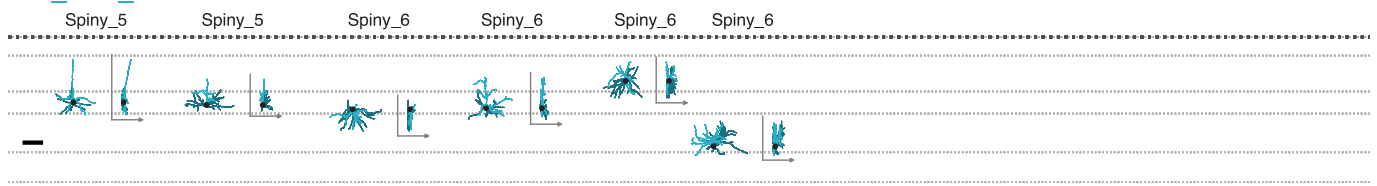
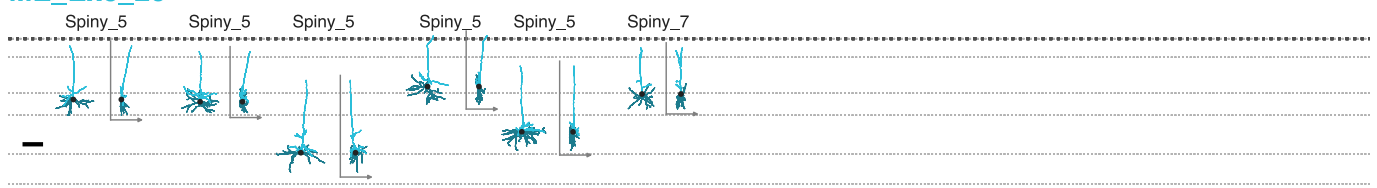
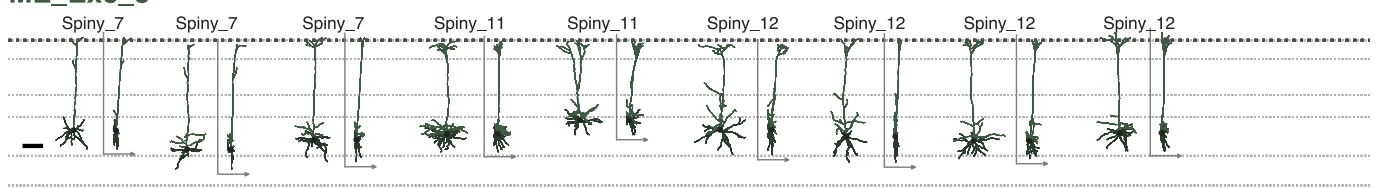
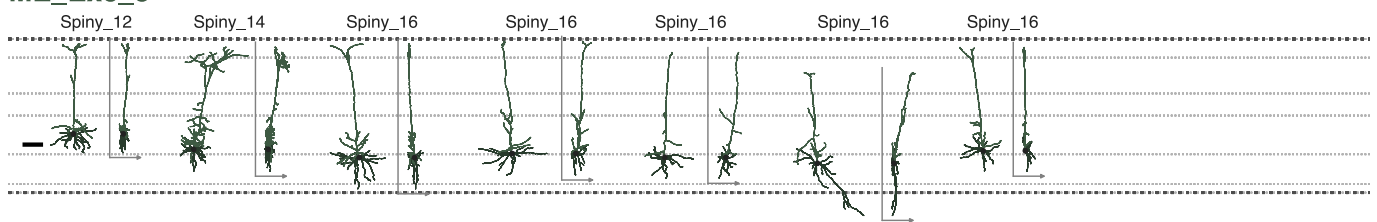
**Supplementary Figure 16: Aspiny feature heatmap and dendrogram.** Dendrogram generated by hierarchical clustering with Ward's agglomeration method using Euclidean distances in the high-dimensional feature space. 19 aspiny m-types are indicated by the m-type-specific color bar. Layer is also indicated by the gray-scale color bar. Heatmap shows values for 45 features by m-type. Features were first converted to z-scores for the analysis.

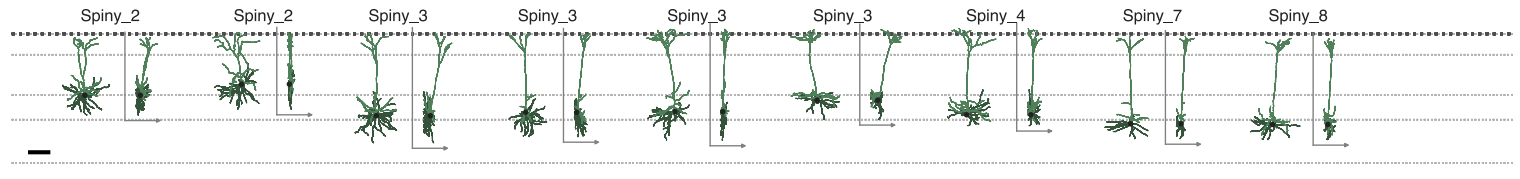
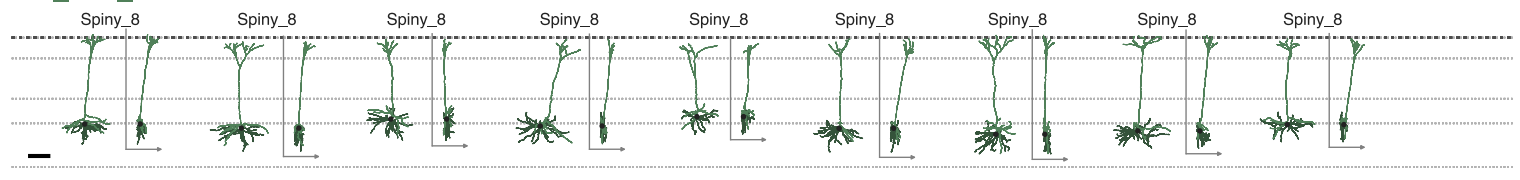
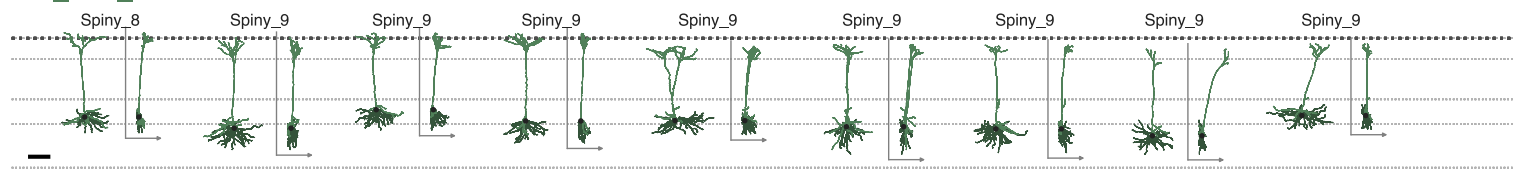
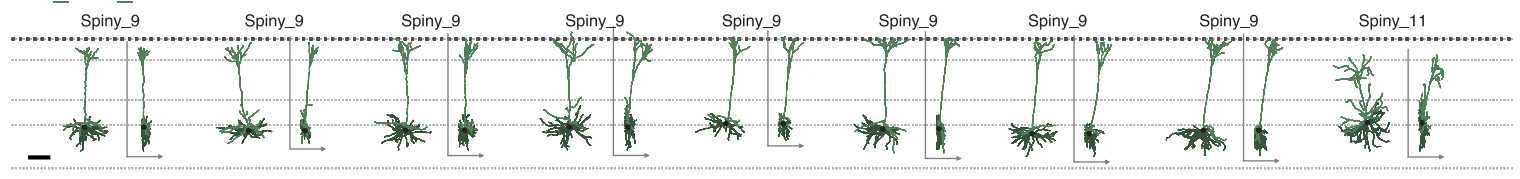
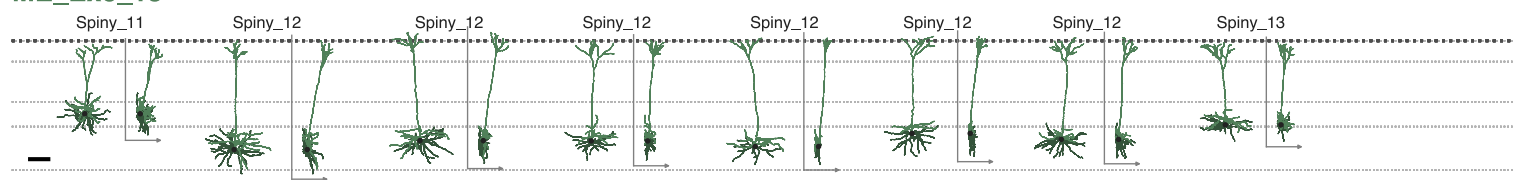
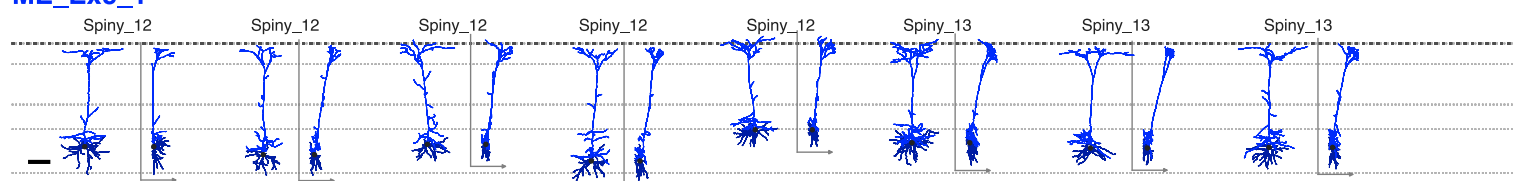
## Supplementary Figure 17

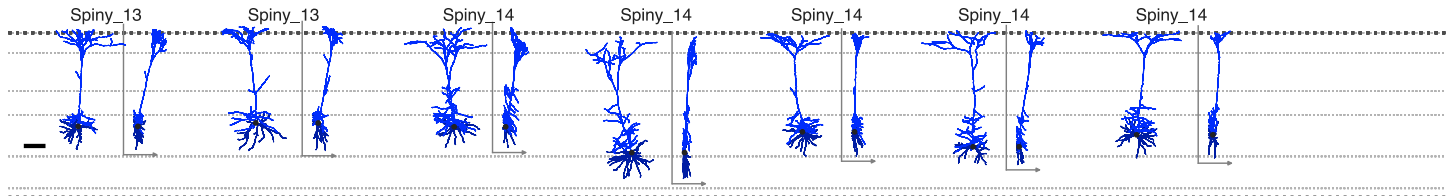
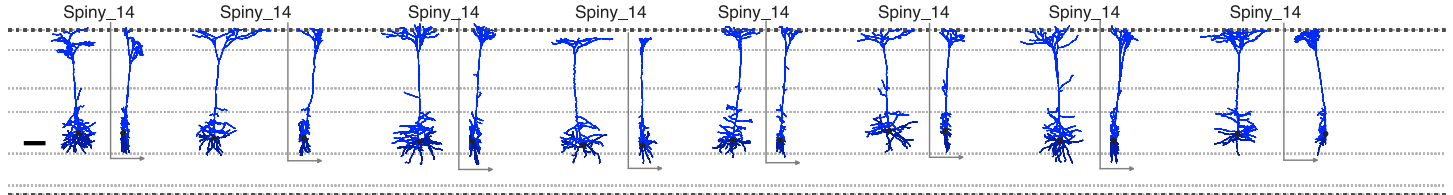
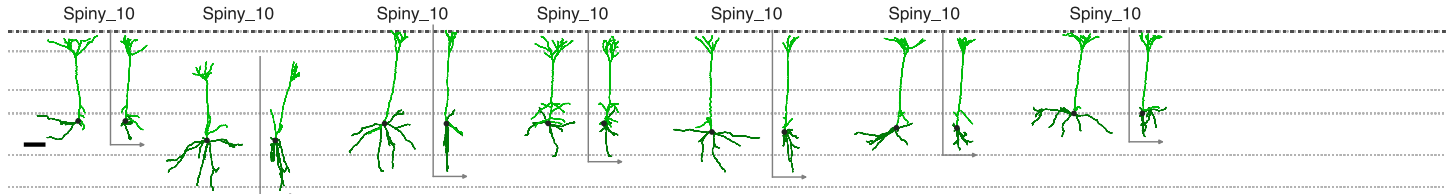
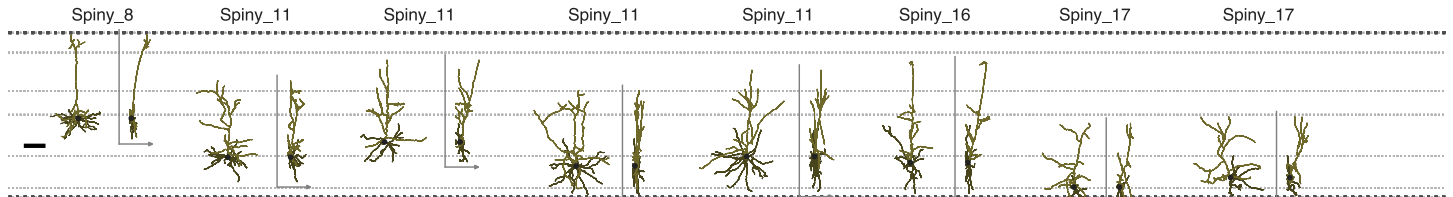
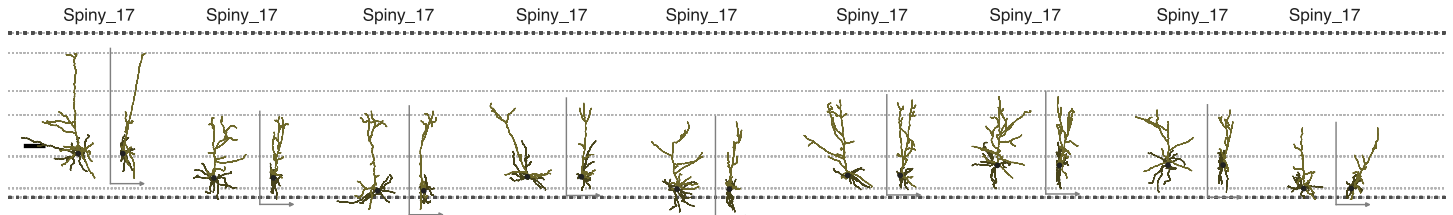
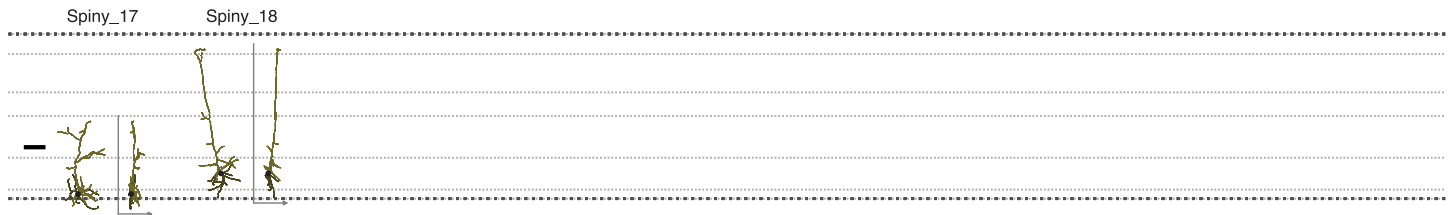


**Supplementary Figure 17: Morphology clustering schematic.** (a) Neurons were reconstructed as described (methods) and feature calculation was performed. Features with low variance (coefficient of variance < 0.25) were removed and a representative feature was chosen among highly correlated features (correlation > 0.95). These features were scaled by z-transform to form a feature set on which a standard hierarchical clustering with Ward's agglomeration method using Euclidean distance was applied. The initial cluster assignment was made by cutting this hierarchical tree using the `cutreehybrid()` function in R package WGCNA<sup>3</sup>, which determined the number of clusters by maximizing between-cluster variation and minimizing within-cluster variation while considering branching structures of the dendrogram. In order to identify robust clusters, a co-clustering analysis was done<sup>4</sup>. This clustering step was run 1000 times with a randomly subsampled 90% of the data in a 10 fold manner and the proportion of all runs that every pair were grouped in the same cluster was recorded in the co-clustering diagram (Figs. 3a and 4a and Fig. 17a). Consensus clusters were found by building a Ward linkage hierarchical tree and cutting the tree by the same `cutreehybrid()` function. If the size of cluster is  $n \leq 3$ , individual samples were assigned to the highest correlated cluster. If any pair of clusters did not have features significantly different (adjusted t-test pvalue <0.01 & fold change > 1.25) between the two, these two clusters were merged. The same co-clustering analysis was run with bootstrapping 90% of samples with replacement for spiny data set. The two co-clustering results demonstrated strong correspondences among highly predictable clusters. (b) Nineteen clusters were found with the subsampling method and 21 clusters were found with the bootstrapping method. A confusion matrix was generated and the Adjusted Rand index was calculated ( $RI = 0.75$ ) to show the correspondence between the two. There were very strong one-to-one correspondences between these two sets of clusters with a few exceptions. For example, boot-strapping-defined cluster 9 and 20 both mapped to Spiny\_14 (Thick Tufted L5 2). Highly related types defined through sub-sampling (Spiny\_3, Tufted L4 and Spiny\_7, Sparse Tufted L4; Spiny\_9, Tufted, L4, 5 1 and Spiny\_12, Tufted, L5,4) had smaller groups of cells that clustered together into a third group when bootstrapping was used (cluster 17; cluster 7). The poor correspondence of Spiny\_6 and cluster 7 was understandable with their low predictability. With additional samples, each cluster's predictability would improve.

**ME\_Exc\_7****ME\_Exc\_7****ME\_Exc\_14****ME\_Exc\_15****ME\_Exc\_16****ME\_Exc\_17****ME\_Exc\_17**

**ME\_Exc\_17****ME\_Exc\_18****ME\_Exc\_18****ME\_Exc\_19****ME\_Exc\_20****ME\_Exc\_5****ME\_Exc\_5**

**ME\_Exc\_12****ME\_Exc\_13****ME\_Exc\_13****ME\_Exc\_13****ME\_Exc\_13****ME\_Exc\_13****ME\_Exc\_1**

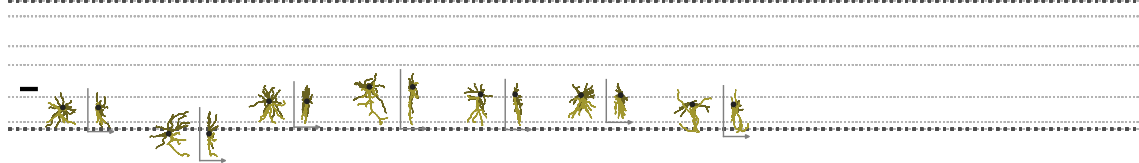
**Supplementary Figure 18 (4)****ME\_Exc\_1****ME\_Exc\_1****ME\_Exc\_1****ME\_Exc\_8****ME\_Exc\_6****ME\_Exc\_6****ME\_Exc\_6**

**ME\_Exc\_10**

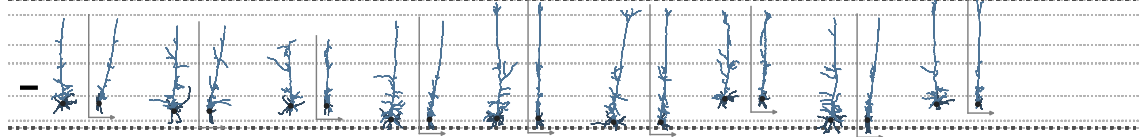
Spiny\_15 Spiny\_15 Spiny\_15

**ME\_Exc\_11**

Spiny\_6 Spiny\_15 Spiny\_15 Spiny\_15 Spiny\_15 Spiny\_15 Spiny\_15

**ME\_Exc\_2**

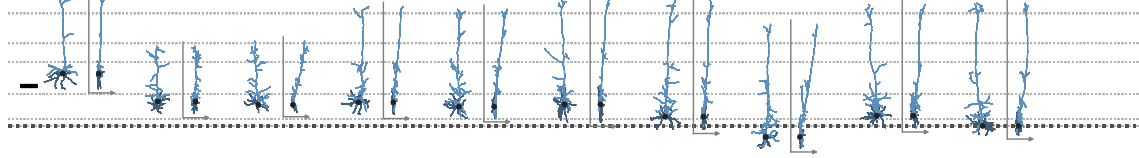
Spiny\_10 Spiny\_17 Spiny\_17 Spiny\_18 Spiny\_18 Spiny\_18 Spiny\_18 Spiny\_18 Spiny\_18

**ME\_Exc\_2**

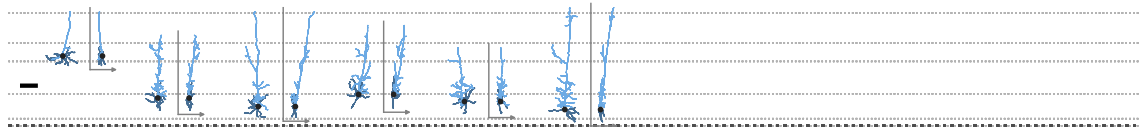
Spiny\_18 Spiny\_18 Spiny\_18 Spiny\_18

**ME\_Exc\_3**

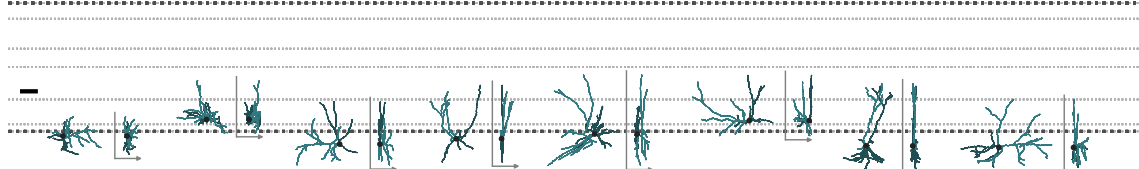
Spiny\_12 Spiny\_17 Spiny\_17 Spiny\_18 Spiny\_18 Spiny\_18 Spiny\_18 Spiny\_18 Spiny\_18

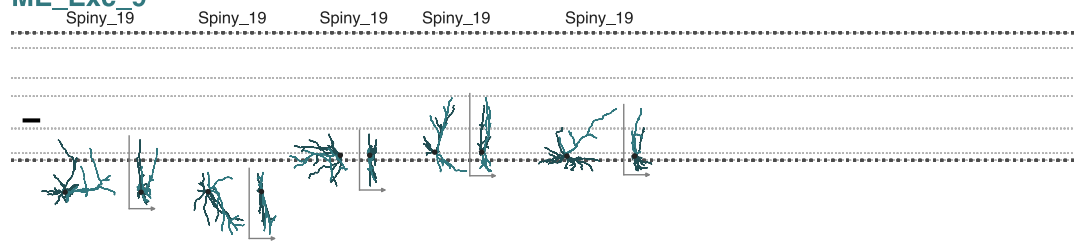
**ME\_Exc\_4**

Spiny\_5 Spiny\_13 Spiny\_14 Spiny\_17 Spiny\_17 Spiny\_18

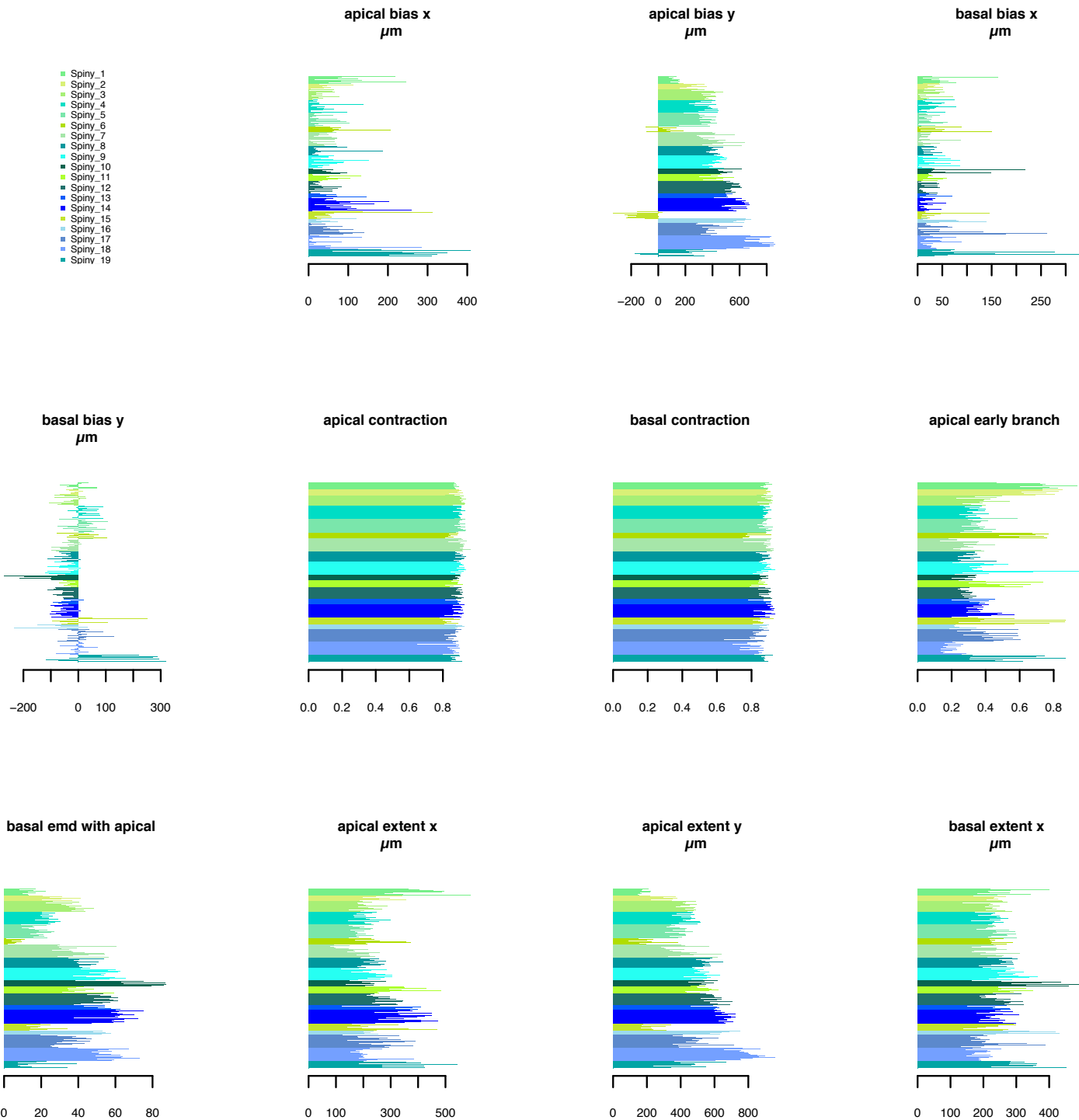
**ME\_Exc\_9**

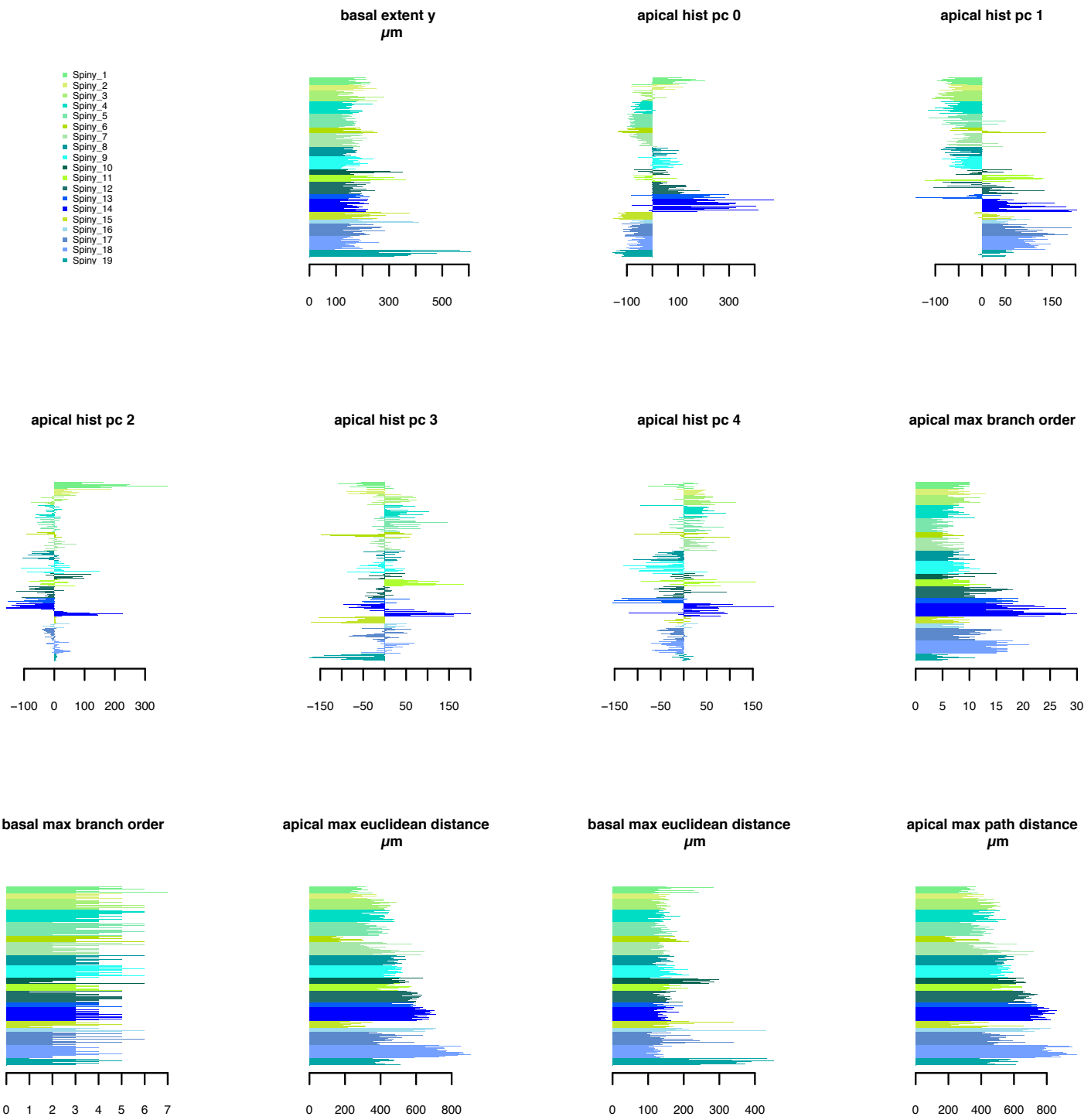
Spiny\_6 Spiny\_6 Spiny\_15 Spiny\_19 Spiny\_19 Spiny\_19 Spiny\_19 Spiny\_19

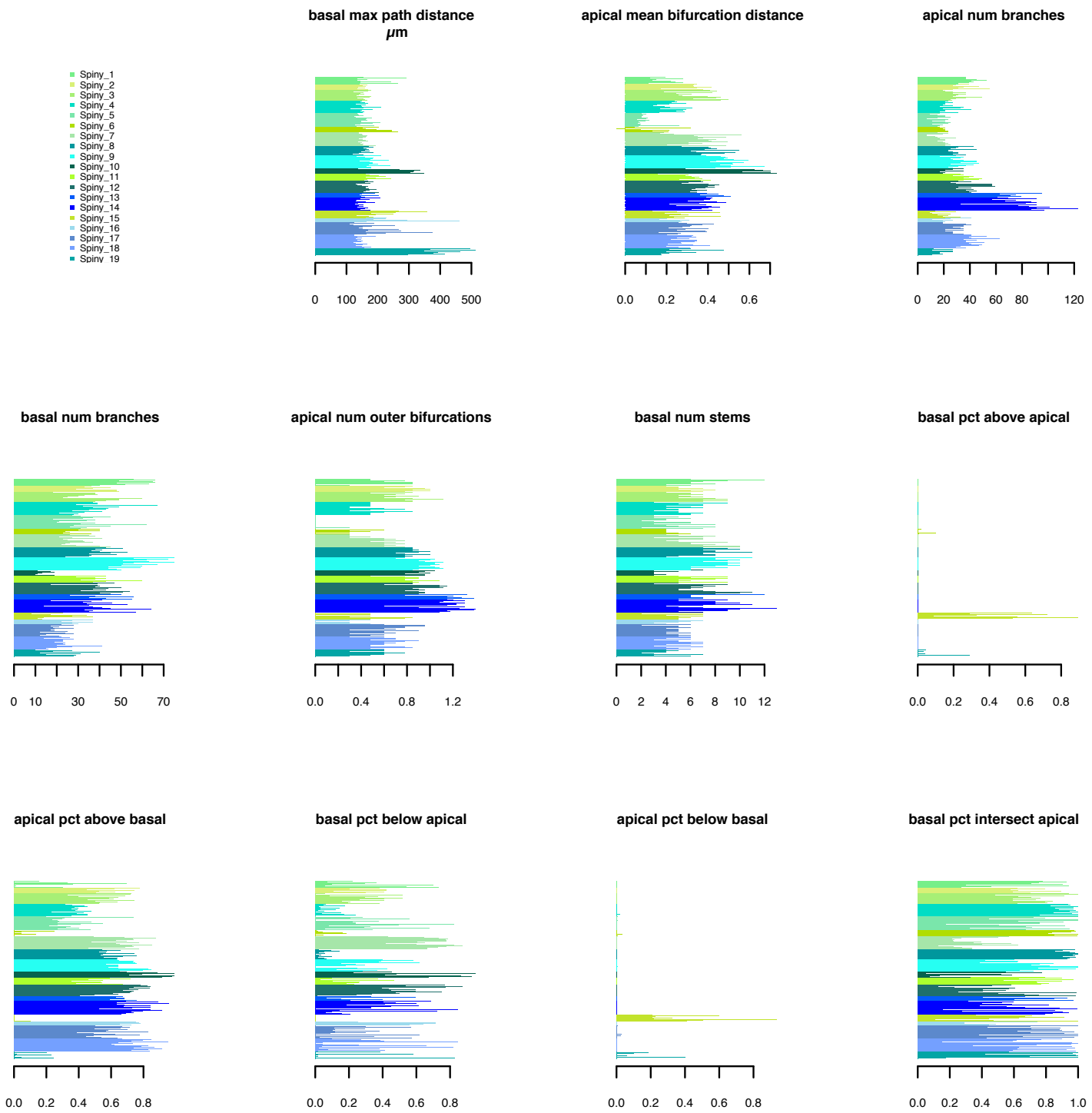


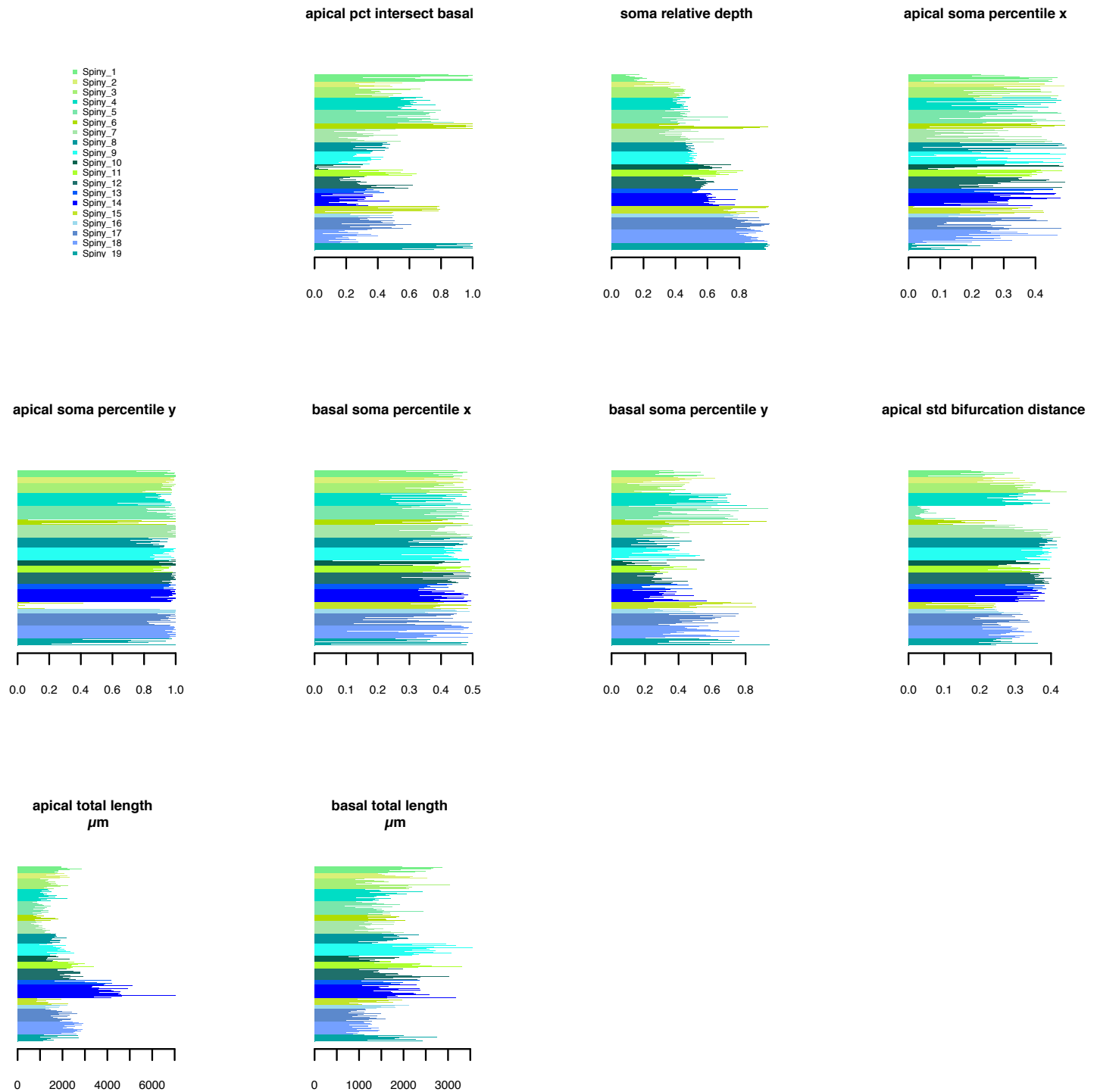
**ME\_Exc\_9**

**Supplementary Figure 18: Spiny neuron morphologies.** 3D reconstructions used in our quantitative analysis are displayed in their approximate laminar location with respect to average cortical layers. Two views of each reconstruction are shown. For each cell, the XY dimension view is on the left and the YZ dimension view is on the right and has an arrow indicating the Z-dimension (in this case, Z is into the depth of the coronal slice). Reconstructions are grouped by me-type and displayed in me-type-specific colors (see Fig. 6). The m-types for each neuron are also shown. Apical dendrites appear in the lighter hue and basal dendrites in the darker hue. We reconstructed neurons with intact, apical dendrites and healthy, relatively intact basal dendrites. Scale bar: 100  $\mu$ m.



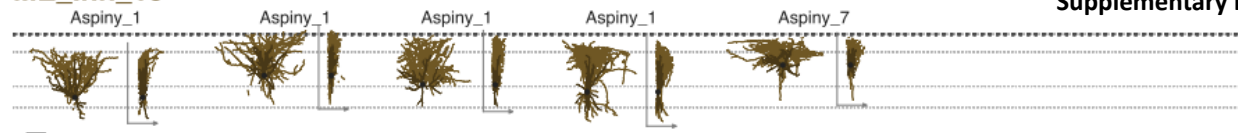




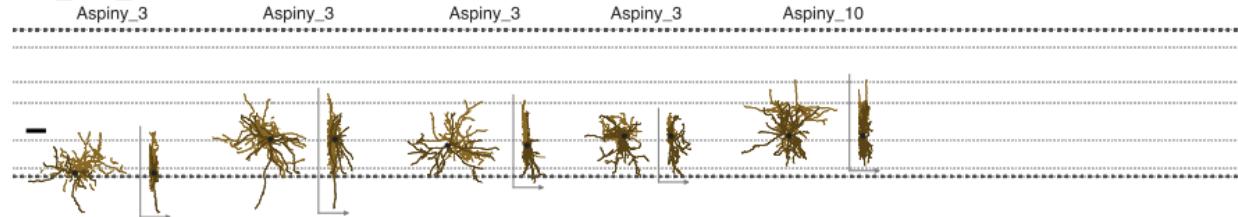


**Supplementary Figure 19: Spiny neuron morphology features by m-type.** Based on 3D reconstructions of the apical and basal dendrites, we extracted 38 morphological features from each neuron. Population histograms of each of feature are shown. Many of the features vary substantially across m-types ( $n = 253$  cells).

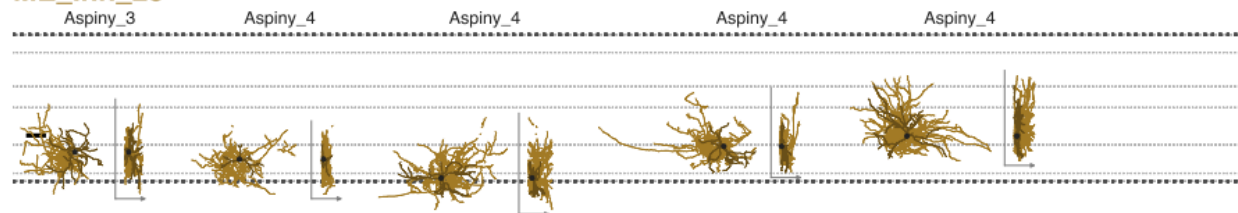
ME\_Inh\_15



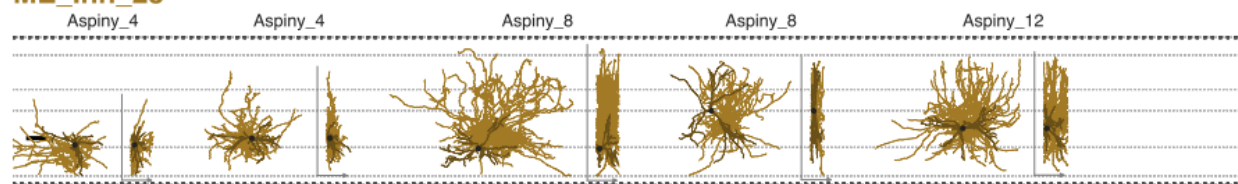
ME\_Inh\_22



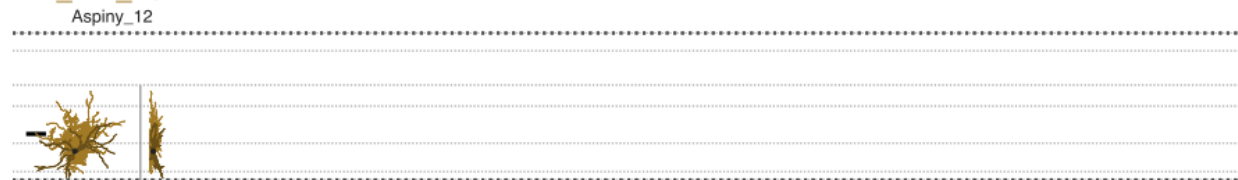
ME\_Inh\_23



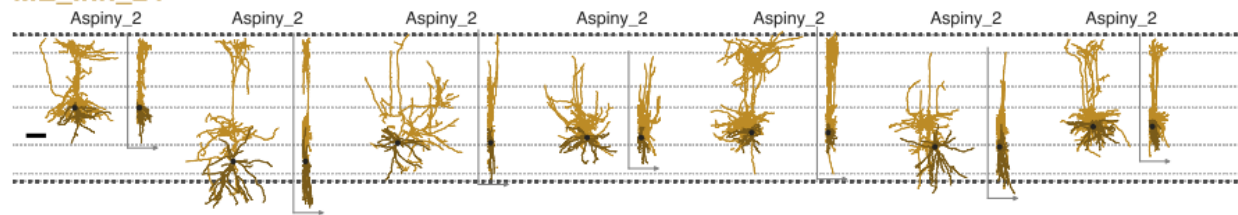
ME\_Inh\_23



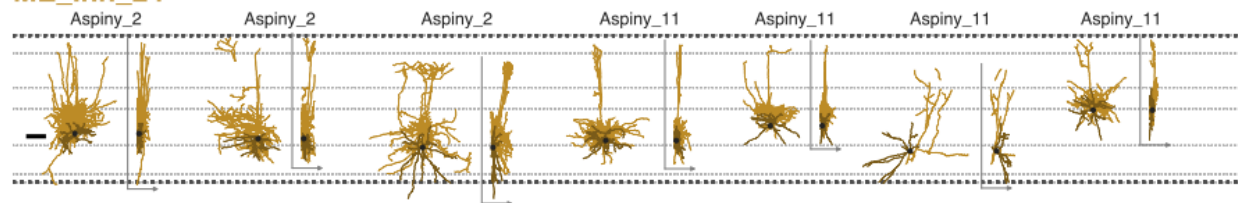
ME\_Inh\_23

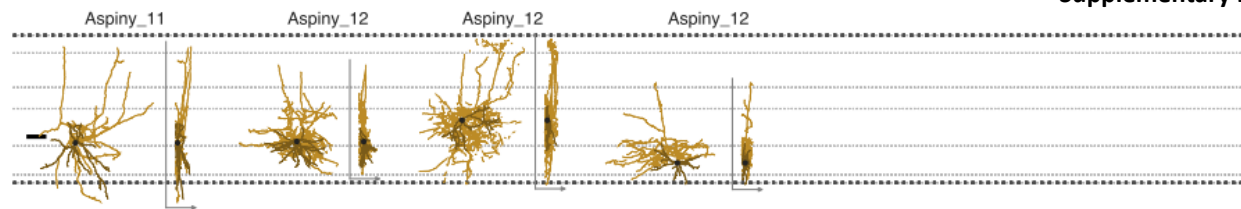
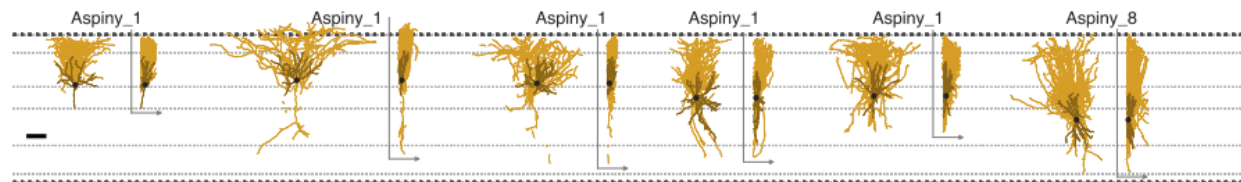
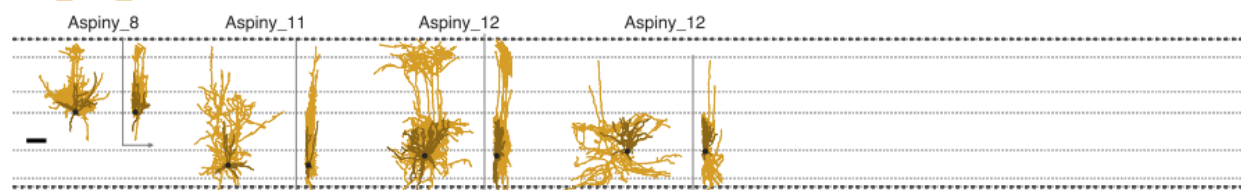
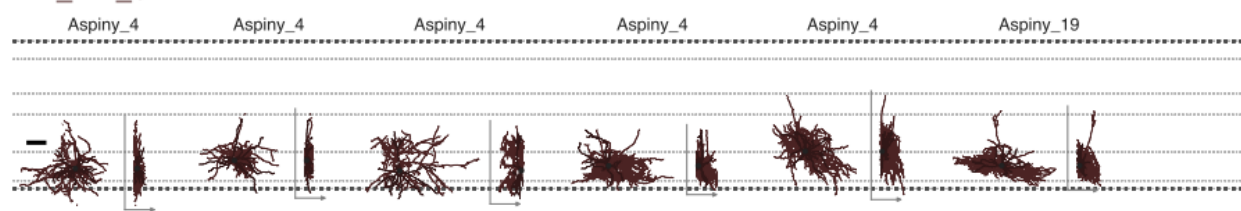
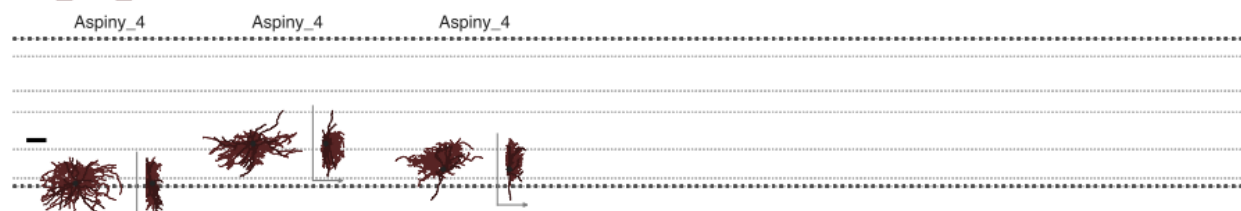


ME\_Inh\_24



ME\_Inh\_24



**ME\_Inh\_24****ME\_Inh\_25****ME\_Inh\_25****ME\_Inh\_26****ME\_Inh\_6****ME\_Inh\_7****ME\_Inh\_8**

**ME\_Inh\_9**

Aspiny\_3

Aspiny\_4

Aspiny\_4

Aspiny\_10

Aspiny\_10

Aspiny\_11

Aspiny\_11

**ME\_Inh\_9**

Aspiny\_12

Aspiny\_12

Aspiny\_12

Aspiny\_19

Aspiny\_19

**ME\_Inh\_10**

Aspiny\_1

Aspiny\_7

Aspiny\_8

Aspiny\_10

Aspiny\_10

Aspiny\_11

**ME\_Inh\_11**

Aspiny\_3

Aspiny\_10

Aspiny\_12

Aspiny\_12

Aspiny\_19

**ME\_Inh\_12**

Aspiny\_4

Aspiny\_8

Aspiny\_8

Aspiny\_9

Aspiny\_9

**ME\_Inh\_13**

Aspiny\_9

Aspiny\_9

Aspiny\_9

Aspiny\_9

**ME\_Inh\_14**

Aspiny\_7

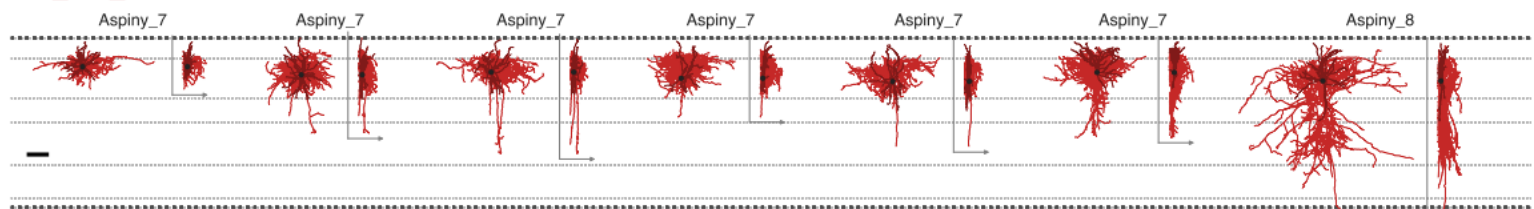
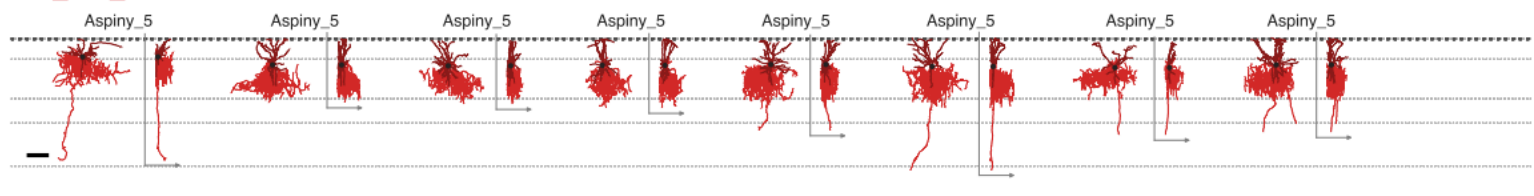
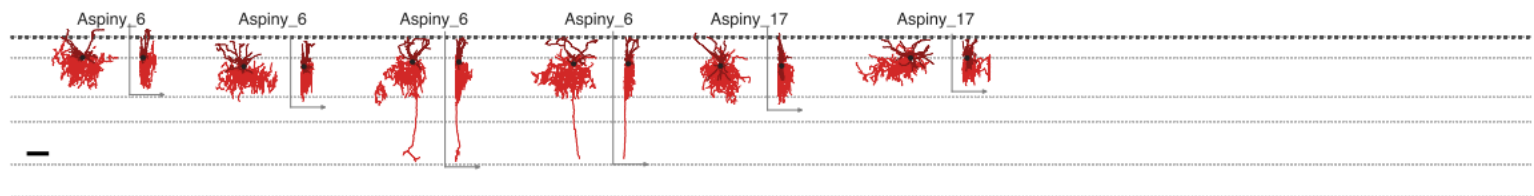
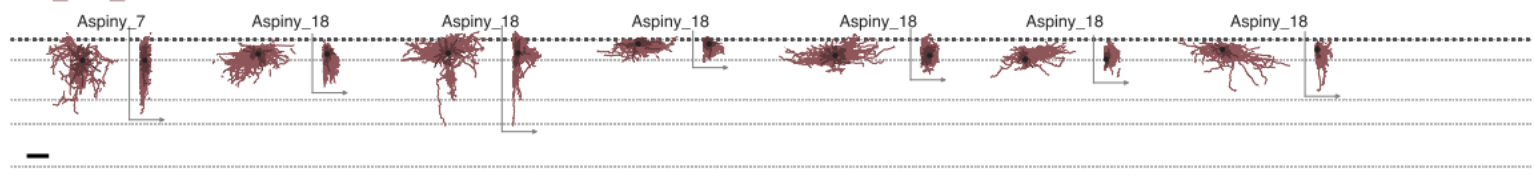
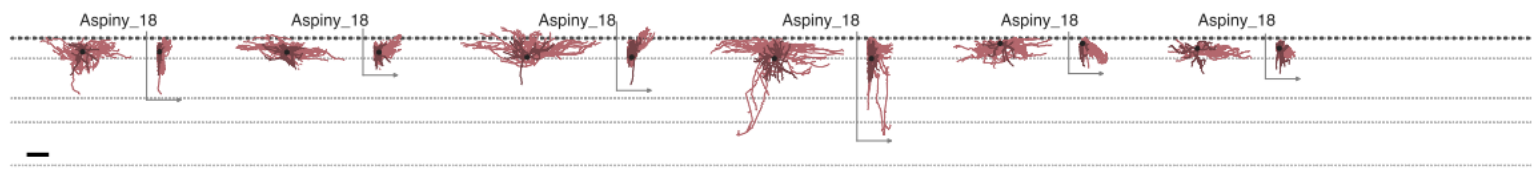
Aspiny\_7

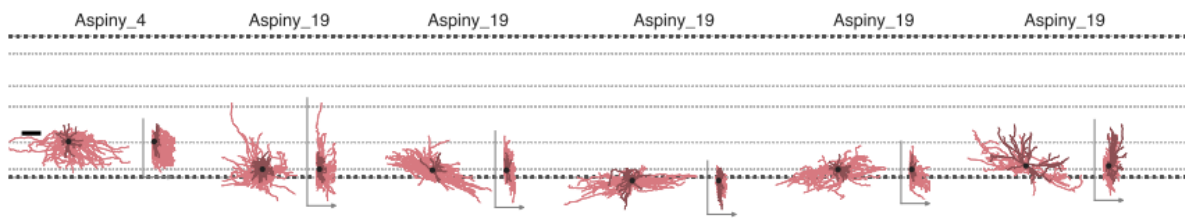
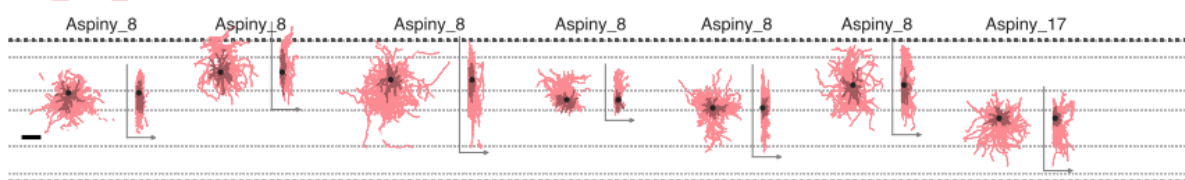
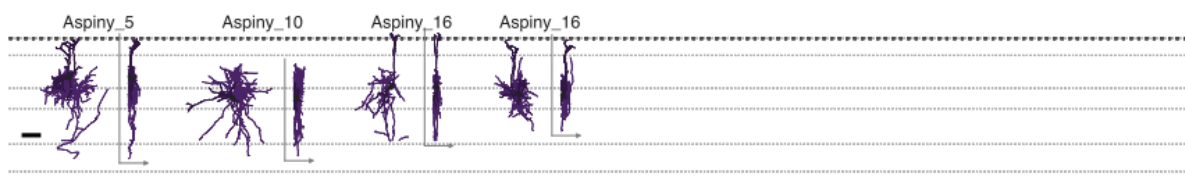
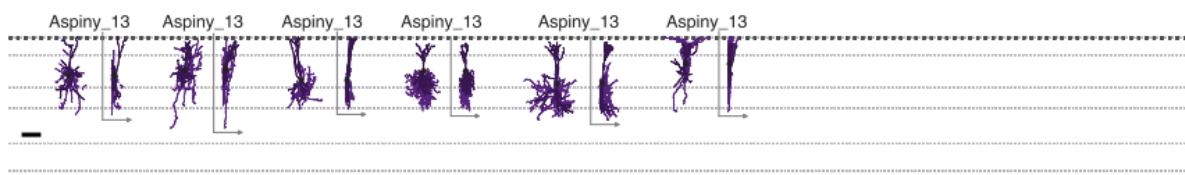
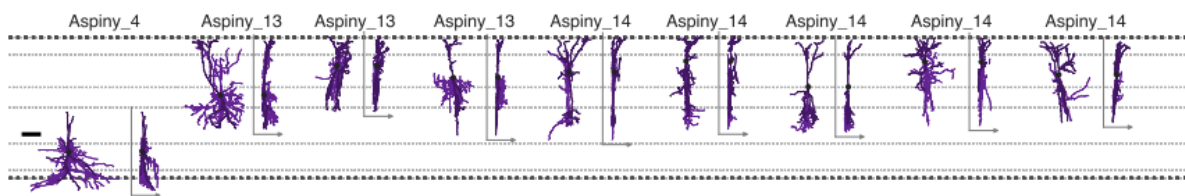
Aspiny\_8

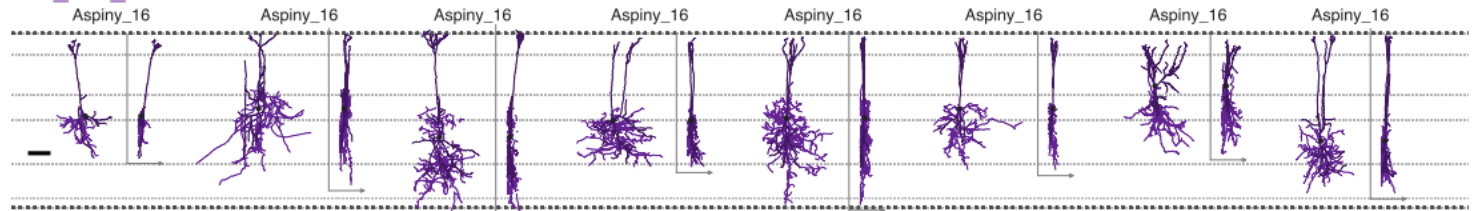
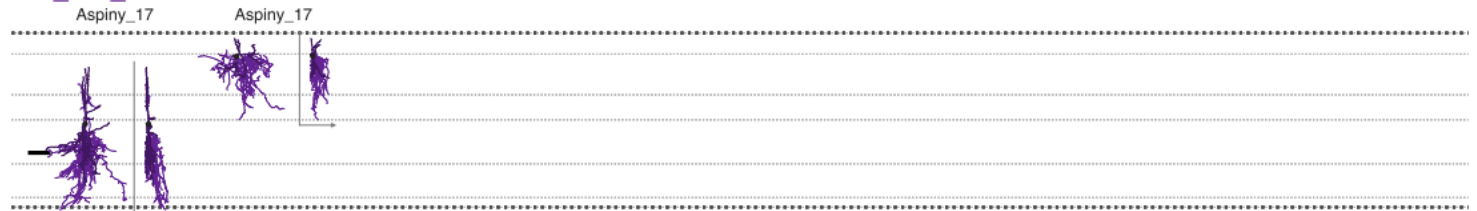
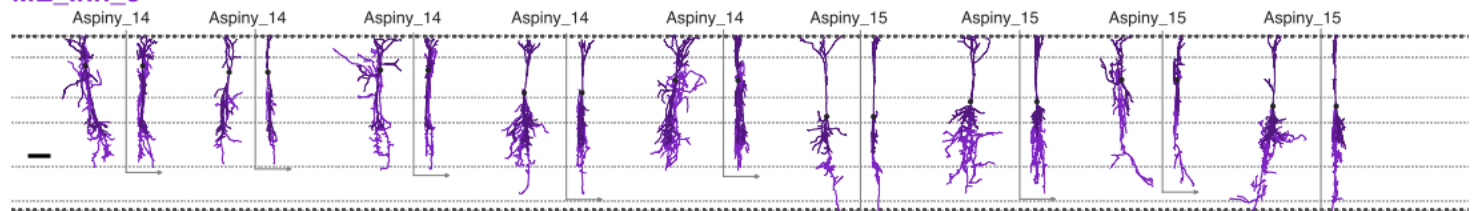
Aspiny\_8

Aspiny\_8

Aspiny\_8

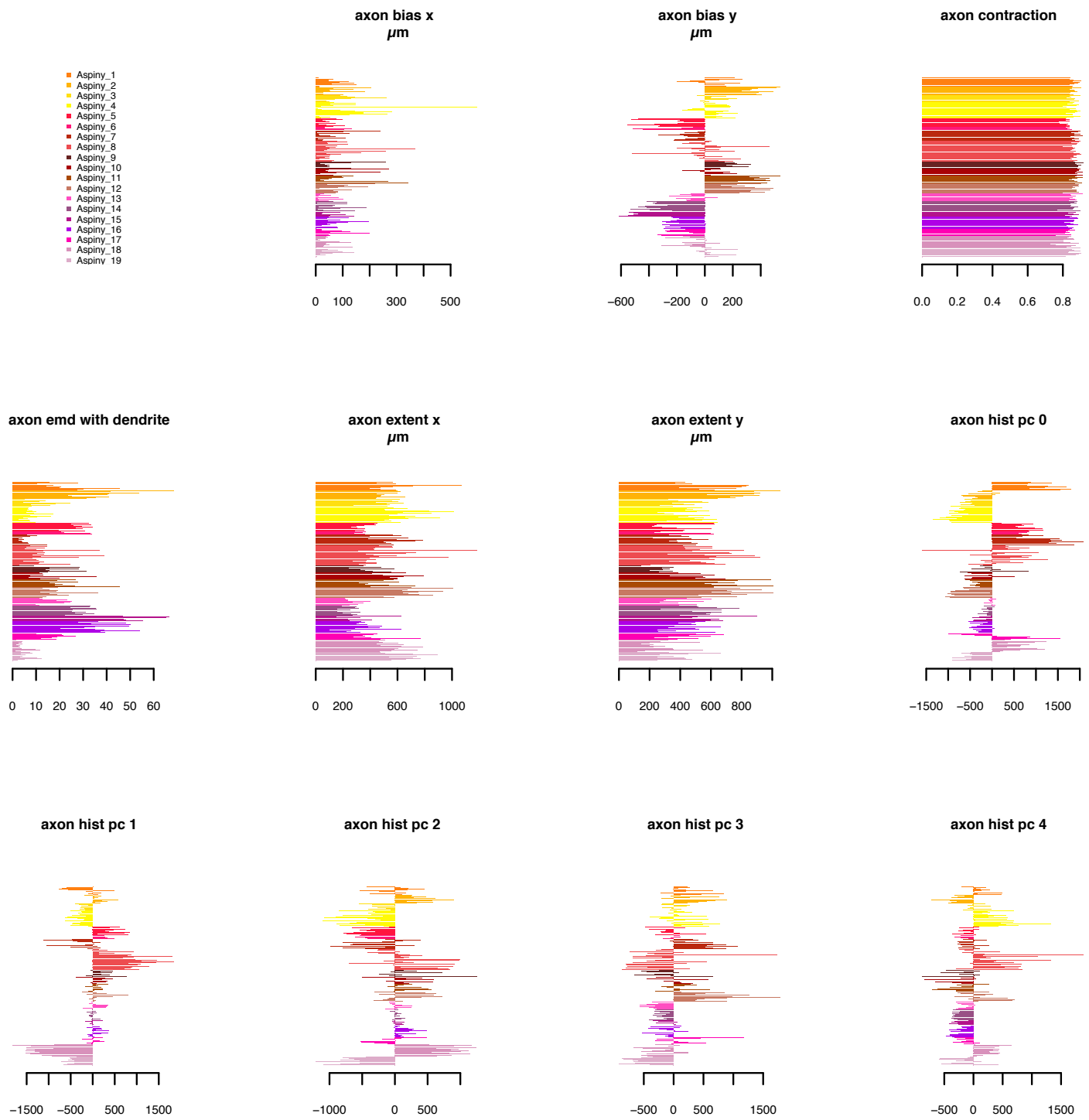
**ME\_Inh\_16****ME\_Inh\_16****ME\_Inh\_21****ME\_Inh\_21****ME\_Inh\_17****ME\_Inh\_17****ME\_Inh\_18**

**ME\_Inh\_19****ME\_Inh\_19****ME\_Inh\_20****ME\_Inh\_20****ME\_Inh\_1****ME\_Inh\_2****ME\_Inh\_3**

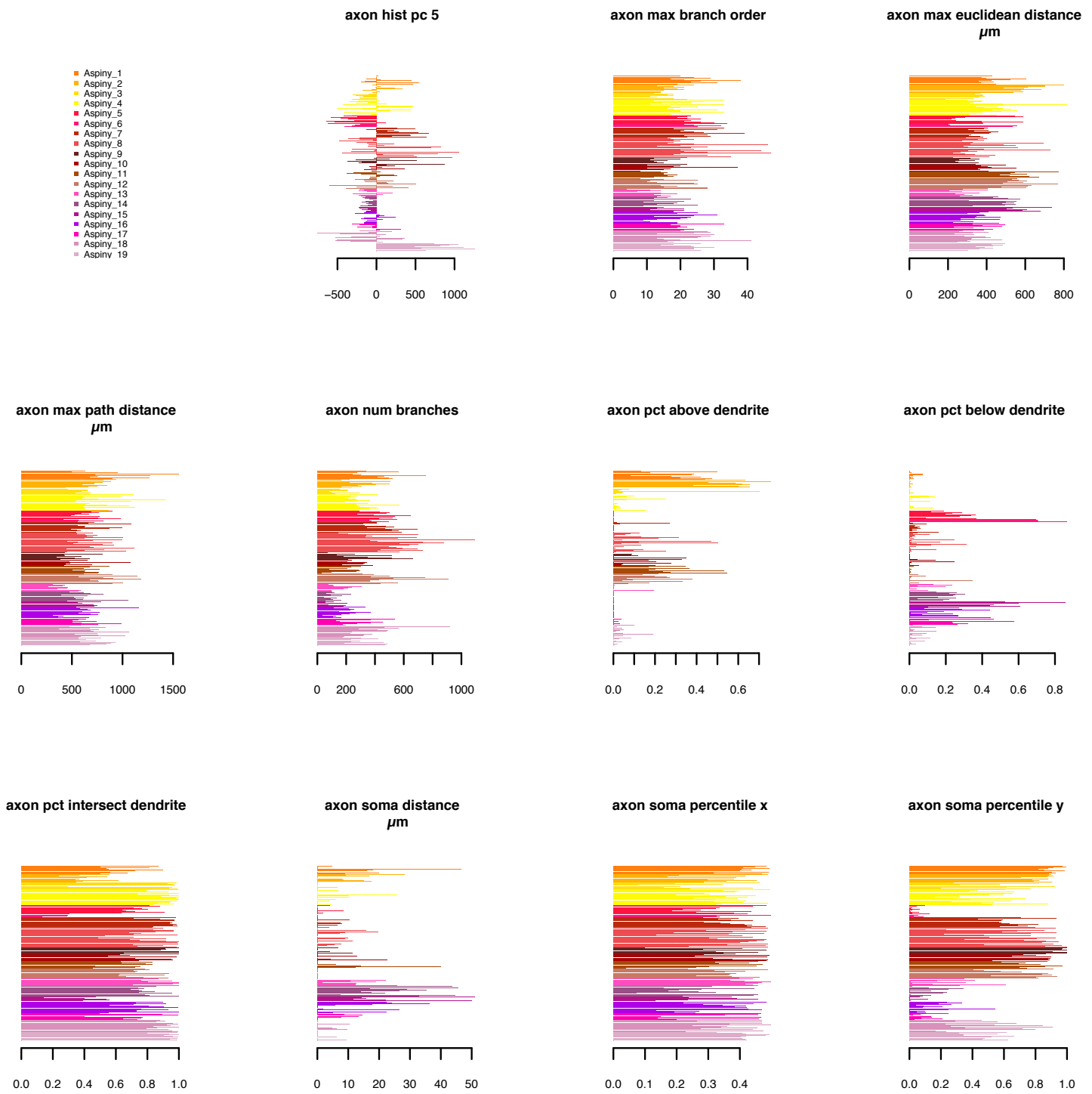
**ME\_Inh\_3****ME\_Inh\_3****ME\_Inh\_4****ME\_Inh\_5****ME\_Inh\_5**

**Supplementary Figure 20: Aspiny and sparsely-spiny neuron morphologies.** 3D reconstructions used in our quantitative analysis are displayed in their approximate laminar location with respect to average cortical layers. Two views of each reconstruction are shown. For each cell, the XY dimension view is on the left and the YZ dimension view is on the right and has an arrow indicating the Z dimension (in this case, Z is into the depth of the coronal slice). Reconstructions are grouped by me-type and displayed in me-type-specific colors (see Fig. 6). Dendrites are displayed in the darker hue and axon in the lighter hue. We reconstructed neurons with healthy, relatively intact dendrites and extensive local axon. Neurons were sampled from all cortical layers and across the major genetically and/or morphologically defined classes in mouse V1Sp.

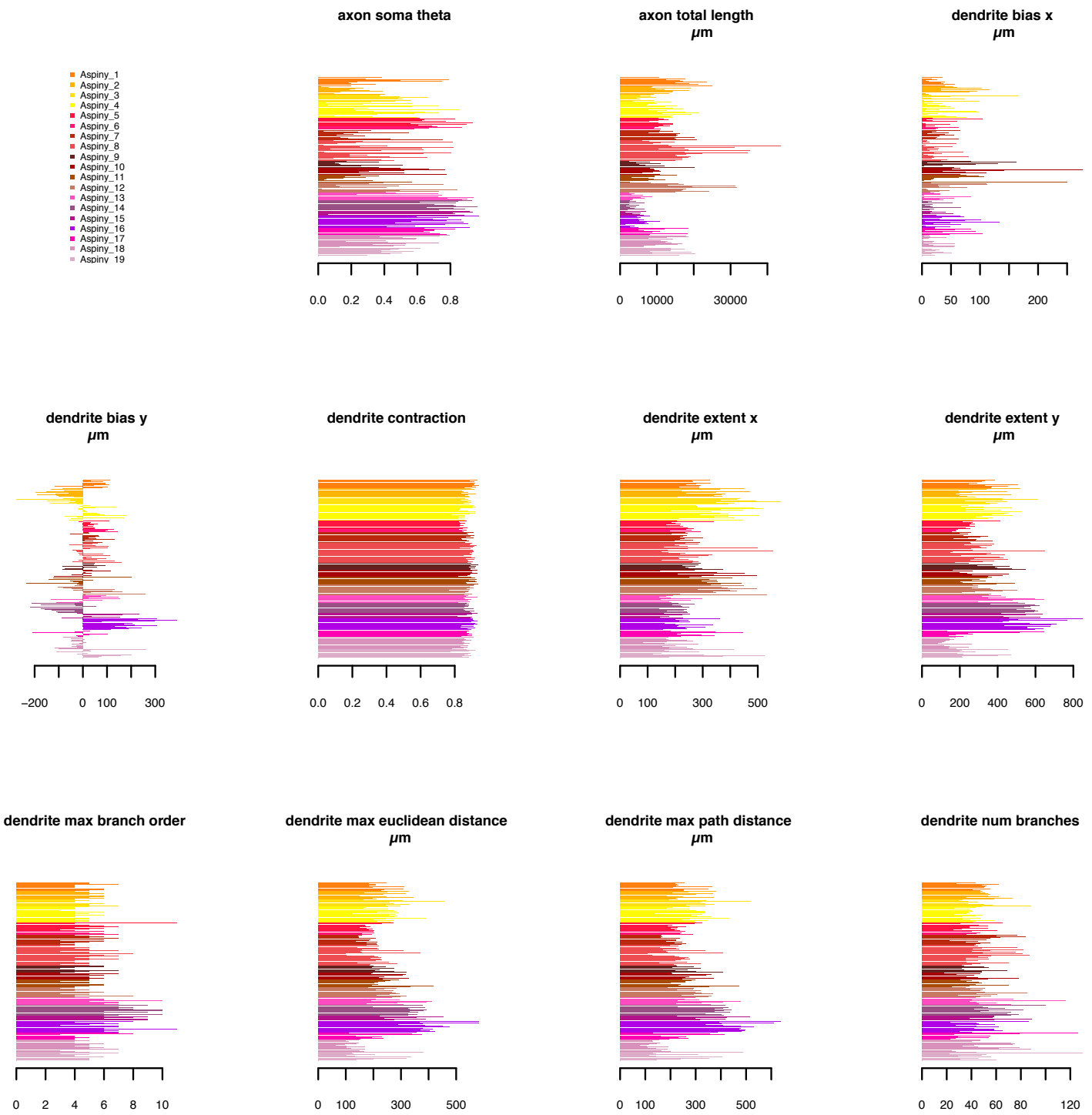
**Supplementary Figure 21 (1)**



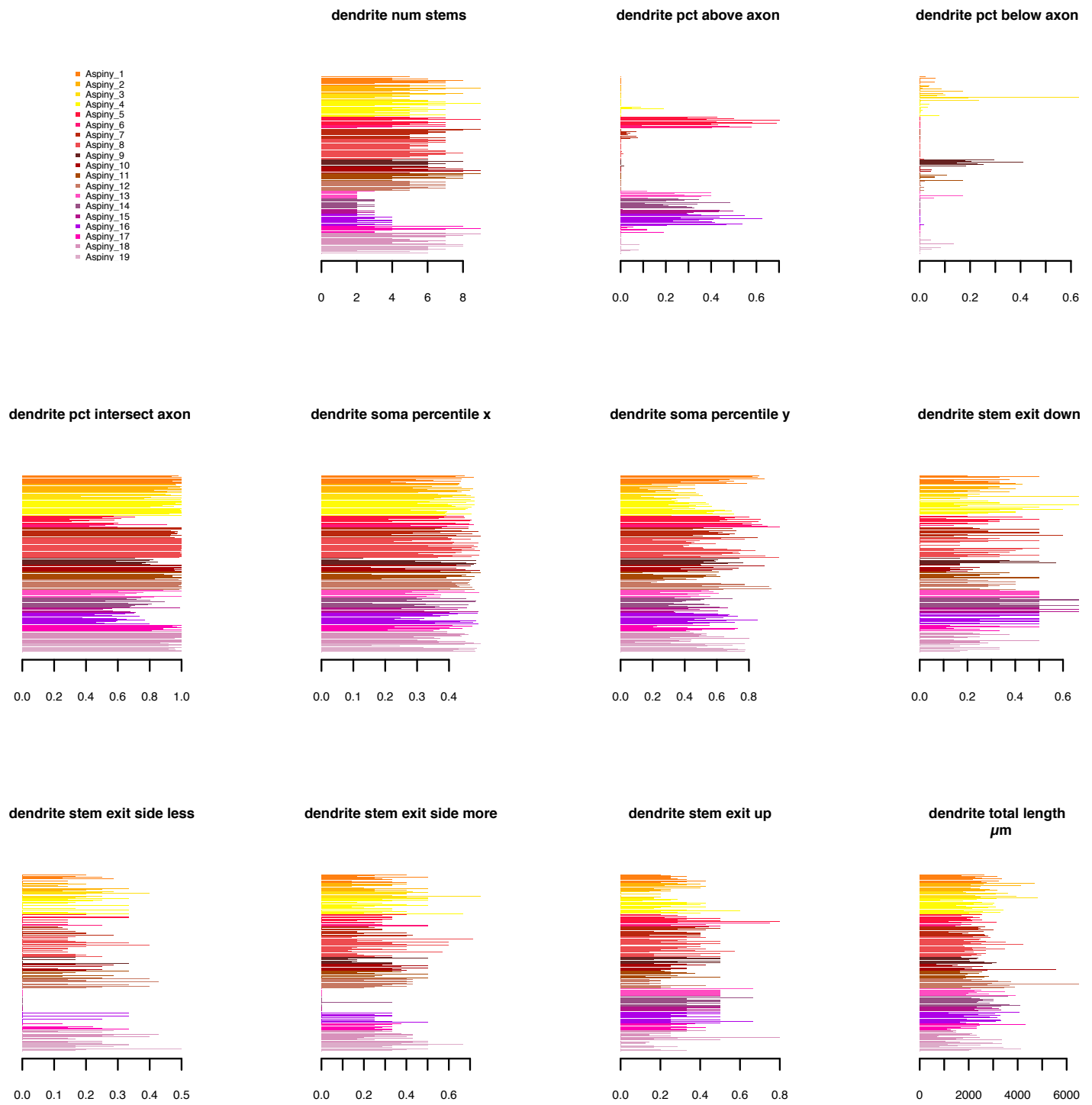
**Supplementary Figure 21 (2)**

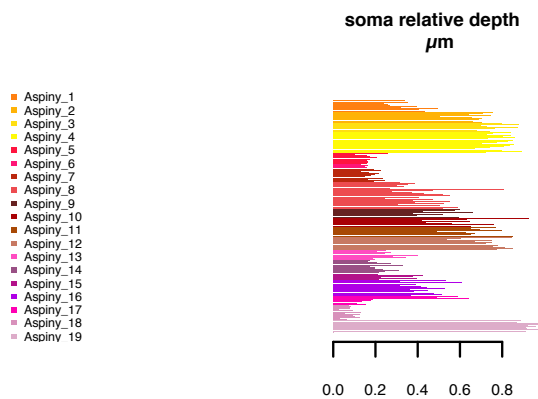


Supplementary Figure 21 (3)



**Supplementary Figure 21 (4)**



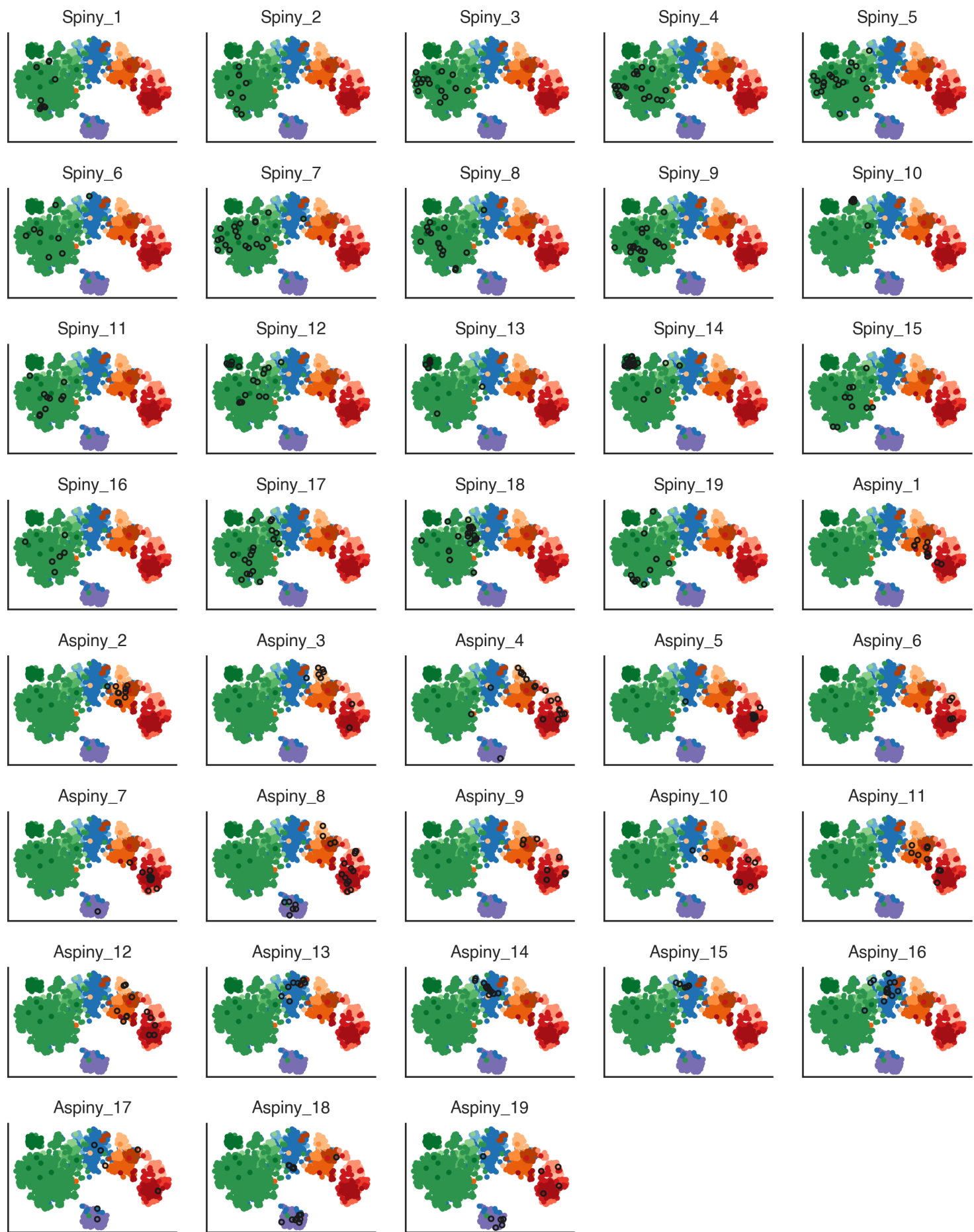


**Supplementary Figure 21: Aspiny and sparsely-spiny neuron morphological features by m-type.** Based on 3D reconstructions of the basal dendrites and local axon, we extracted numerous morphological features from each neuron. Population histograms of 34 representative features are shown. Many of the features vary substantially across m-types ( $n = 207$  cells).

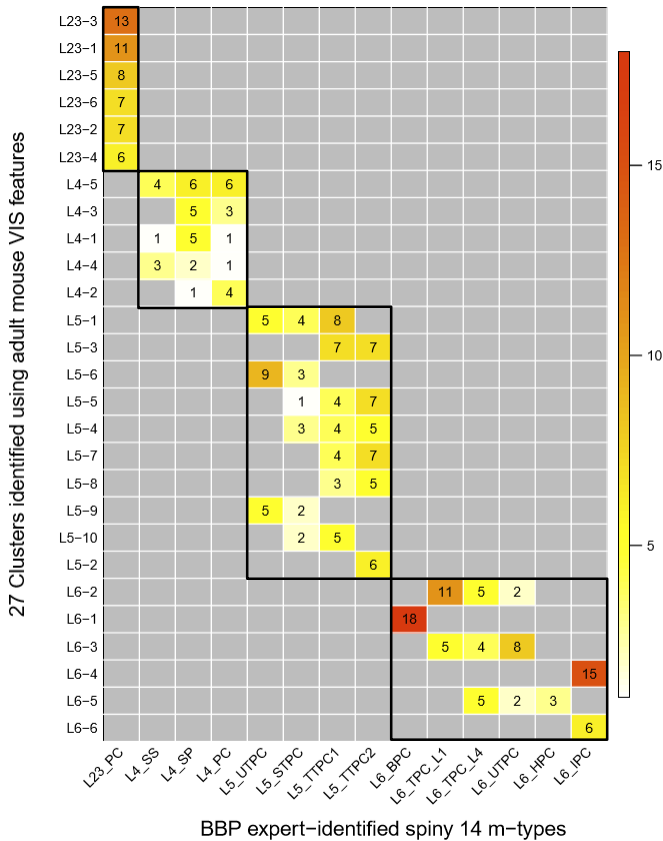


**Supplementary Figure 22: Transgenic lines and m-types.** Fraction of cells from each transgenic line examined (rows) that fall into each m-type (columns). Dot size indicates the fraction of the row falling into a given column, and color indicates m-type.

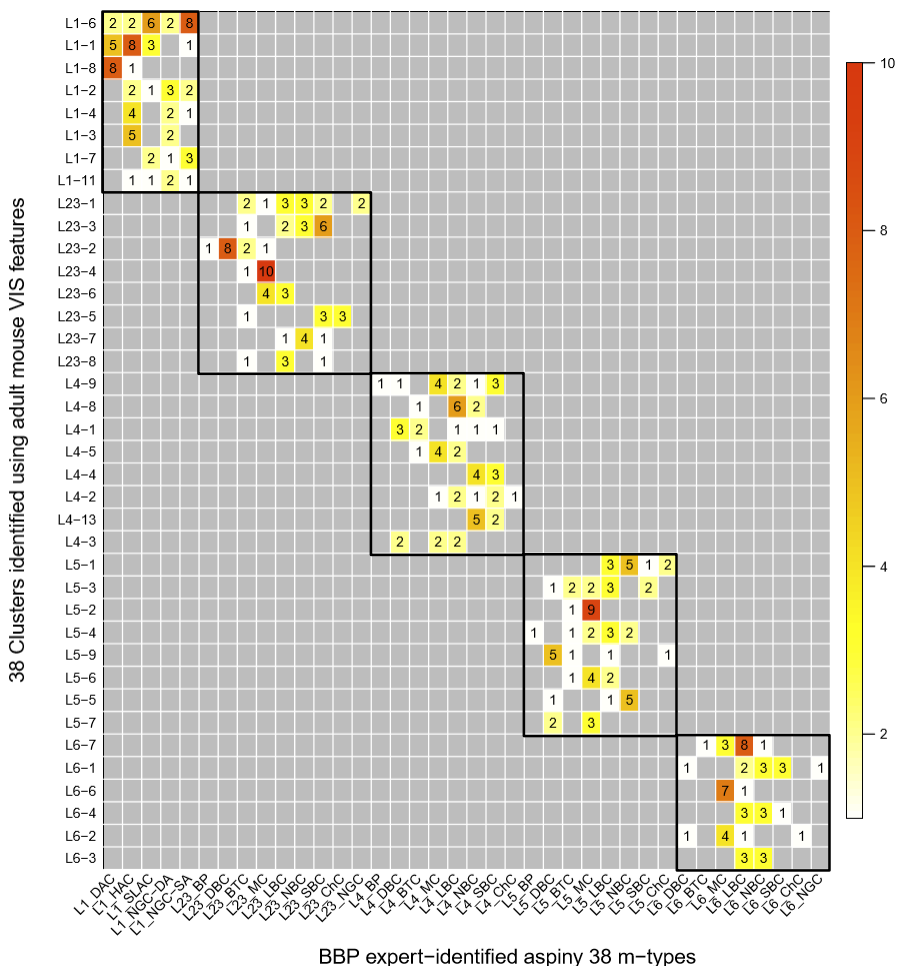
**Supplementary Figure 23**



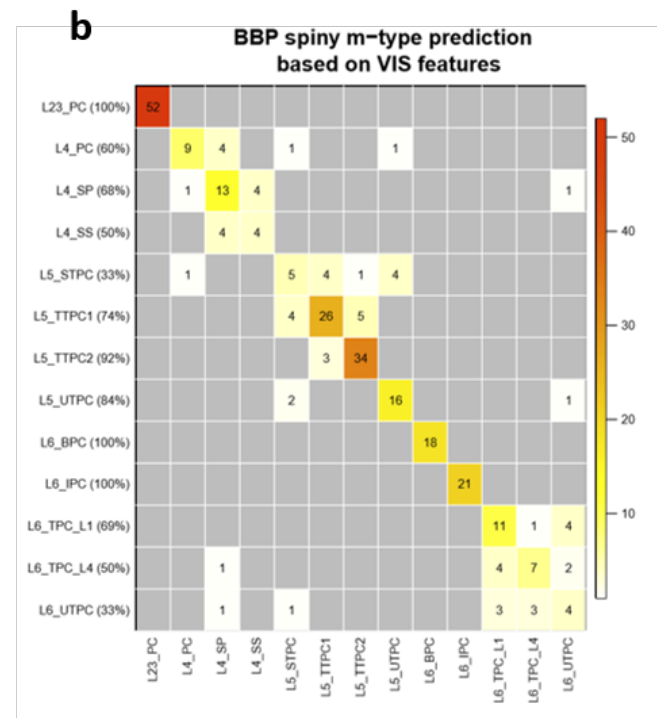
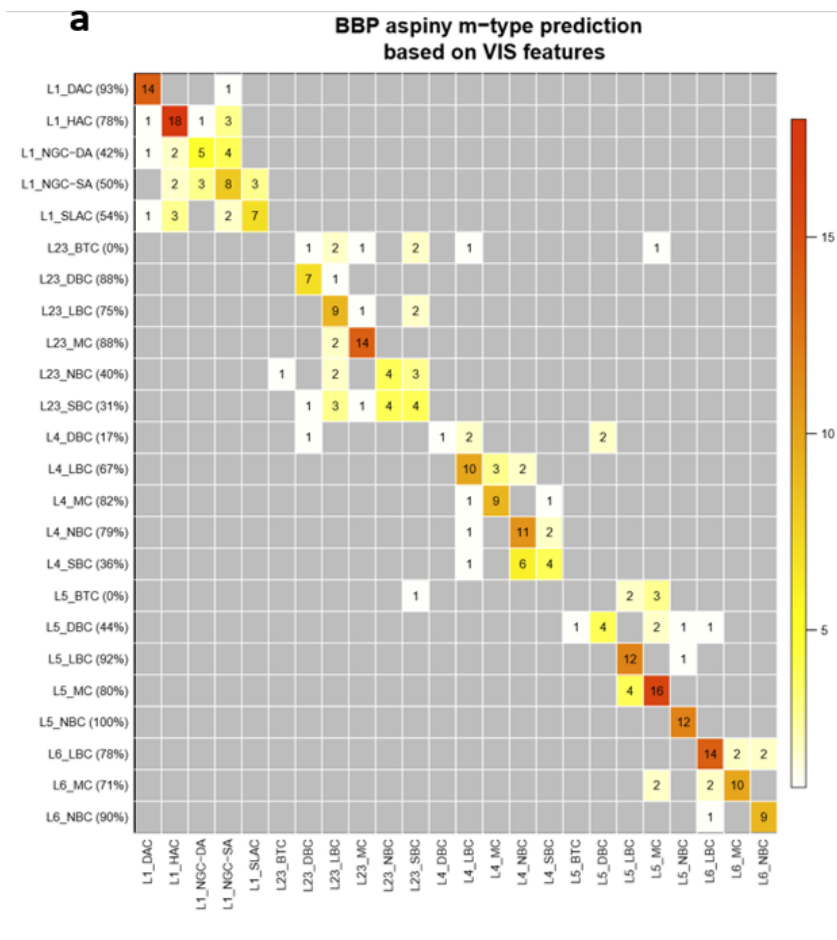
**Supplementary Figure 23: Locations of m-types on the electrophysiological projection.**  
Electrophysiology-based t-SNE plots ( $n = 1,938$  cells) with cells from different m-types highlighted. Colors indicate e-type labels (see Fig. 2). Cells with the indicated m-type are indicated with black circles.



**Supplementary Figure 24: Morphological classification of spiny/excitatory juvenile rat somatosensory cortex neurons and mapping to adult mouse visual cortex neurons.** Using the morphologies available through the Neocortical Microcircuit Collaboration Portal (<http://microcircuits.epfl.ch/#/main>), we tested our ability to use our unsupervised, morphological classification system to objectively identify m-types in neurons from a different age, species and cortical brain region (juvenile, rat, primary somatosensory neurons). Unfortunately, this dataset lacks information about cortical context (e.g., relative soma depth, axon layer distribution), so it was necessary to exclude the context-dependent features that were used in our classification of mouse VIS neurons. Instead, we did a separate clustering analysis on neurons from layers 2/3-6. We found reasonable agreement (Adjusted Rand index = 0.27) between our quantitatively-defined types and the expert-identified neurons in this dataset, with some additional diversity.

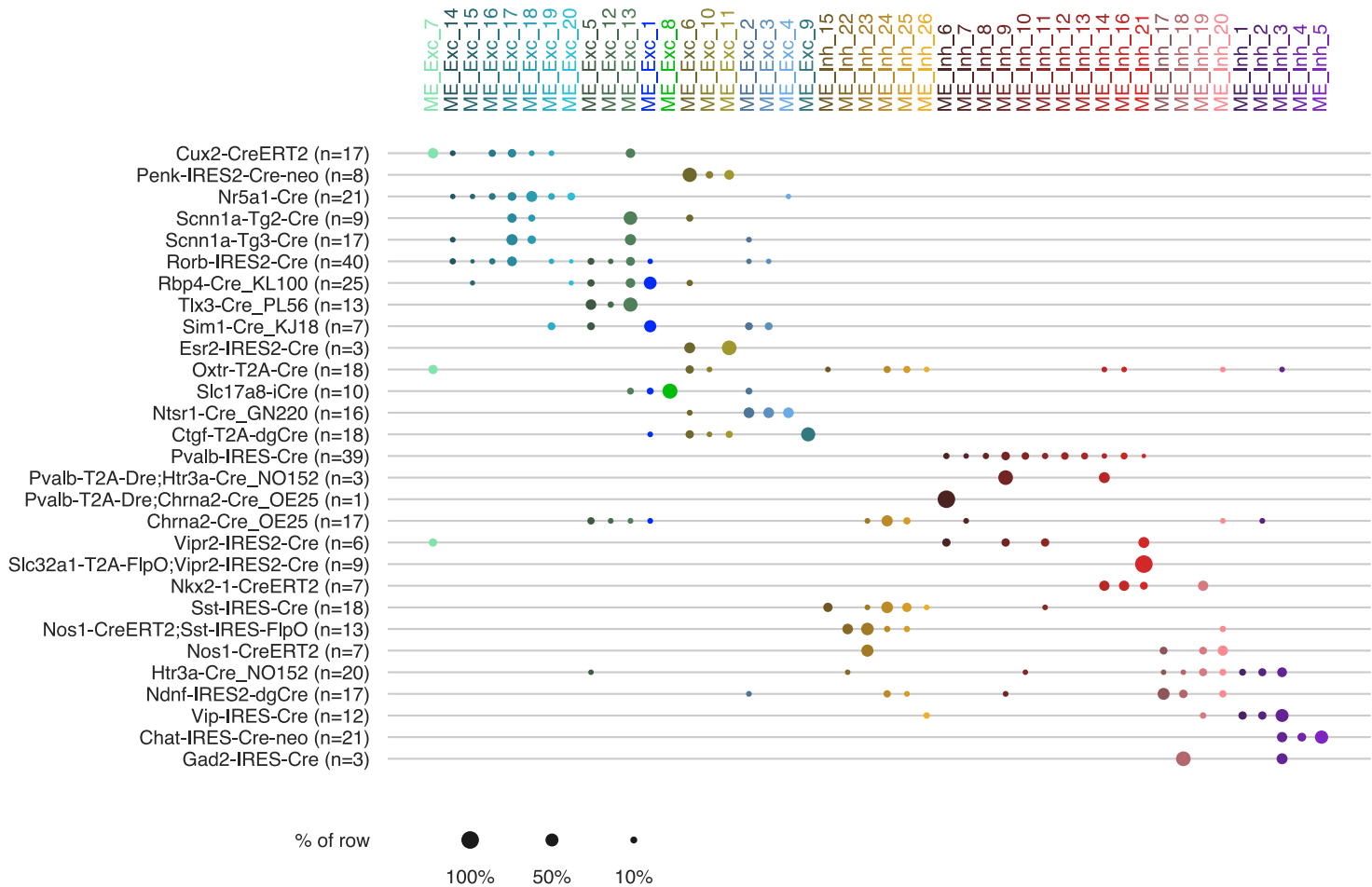


**Supplementary Figure 25: Morphological classification of aspiny/inhibitory juvenile rat somatosensory cortex neurons and mapping to adult mouse visual cortex neurons.**  
Using the morphologies available through the Neocortical Microcircuit Collaboration Portal (<http://microcircuits.epfl.ch/#/main>), we tested our ability to use our unsupervised, morphological classification system to objectively identify m-types in neurons from a different age, species and cortical brain region (juvenile, rat, primary somatosensory neurons). Unfortunately, this dataset lacks information about cortical context (e.g., relative soma depth, axon layer distribution), so it was necessary to exclude the context-dependent features that were used in our classification of mouse VIS neurons. Instead, we did a separate clustering analysis on neurons from layers 1-6. We found reasonable agreement (adjusted Rand index = 0.23) between our quantitatively-defined types and the expert-identified neurons in this dataset, with some additional diversity.

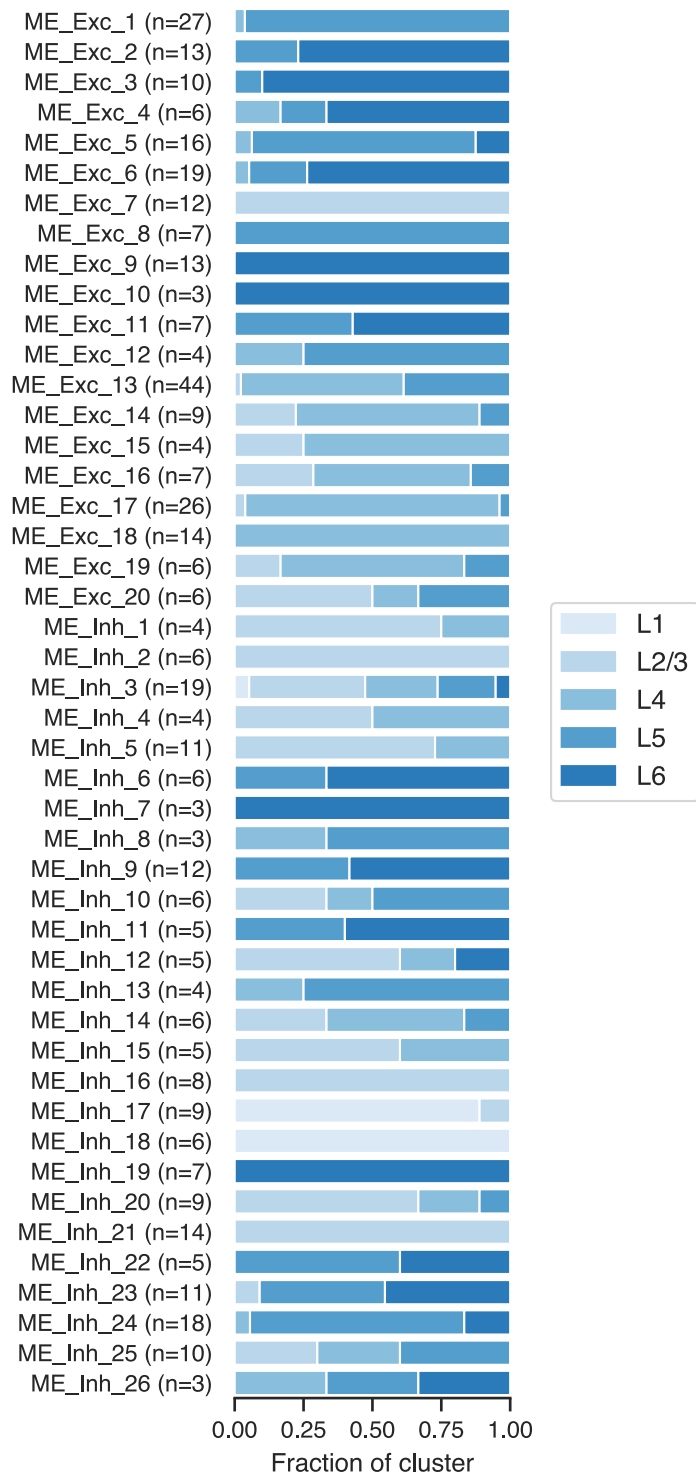


### Supplementary Figure 26: Applicability of morphology features in Supp. Table 3 for morphology analysis of juvenile rat somatosensory neurons.

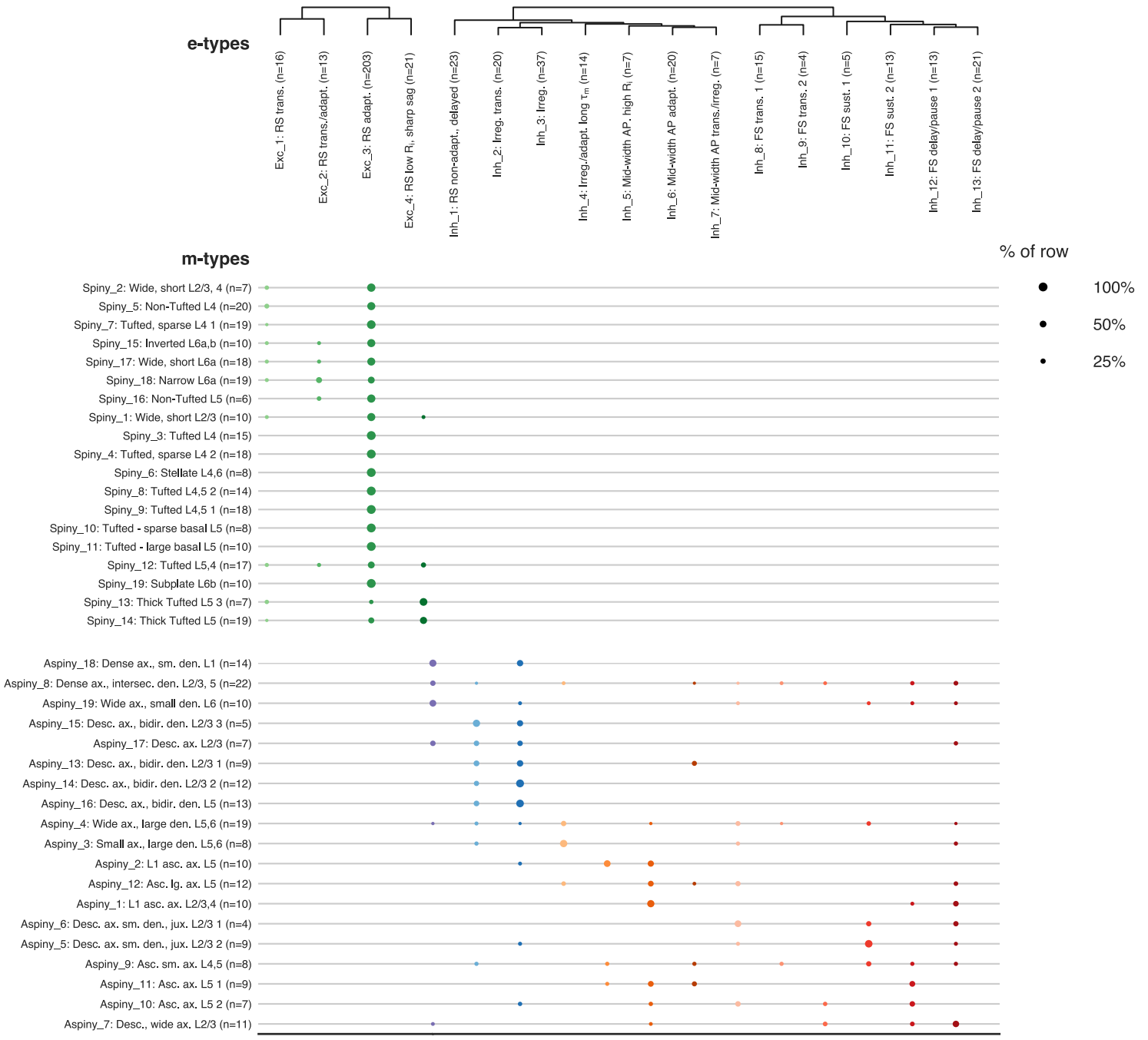
The same morphology features used for mouse visual cortex neurons were calculated for juvenile rat somatosensory neurons. A random forest (RF) classifier was designed using these features to predict the expert-specified m-types where  $n > 3$  neurons, 24 aspiny m-types and 13 spiny m-types. RF classifier's out-of-bag prediction accuracy for spiny/aspiny m-types was 69/62%, which was comparable with the prediction accuracy reported in Markram et al., 2015, around 70% for 43 m-types with 15 features selected for each layer and types. The individual m-type's prediction accuracies are in (a) for 24 m-types in aspiny/inhibitory neurons and (b) for 13 m-types in spiny/excitatory neurons.



**Supplementary Figure 27: Transgenic lines and me-types.** Fraction of cells from each transgenic line examined (rows) that fall into each me-type (columns). Dot size indicates the fraction of the row falling into a given column, and color indicates me-type.

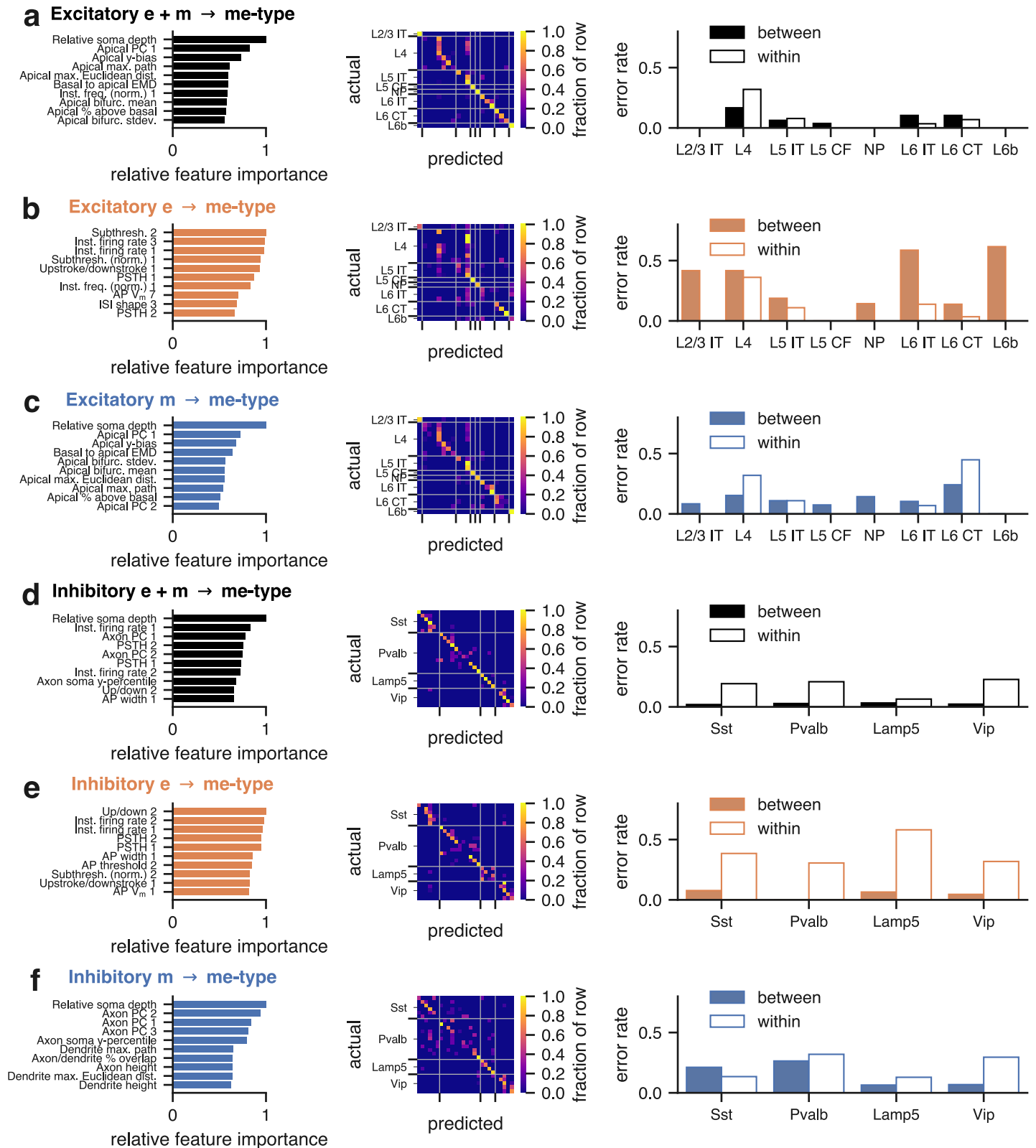


**Supplementary Figure 28: Cortical layer distribution of me-types.** Distribution of cells from each me-type across the cortical layers.



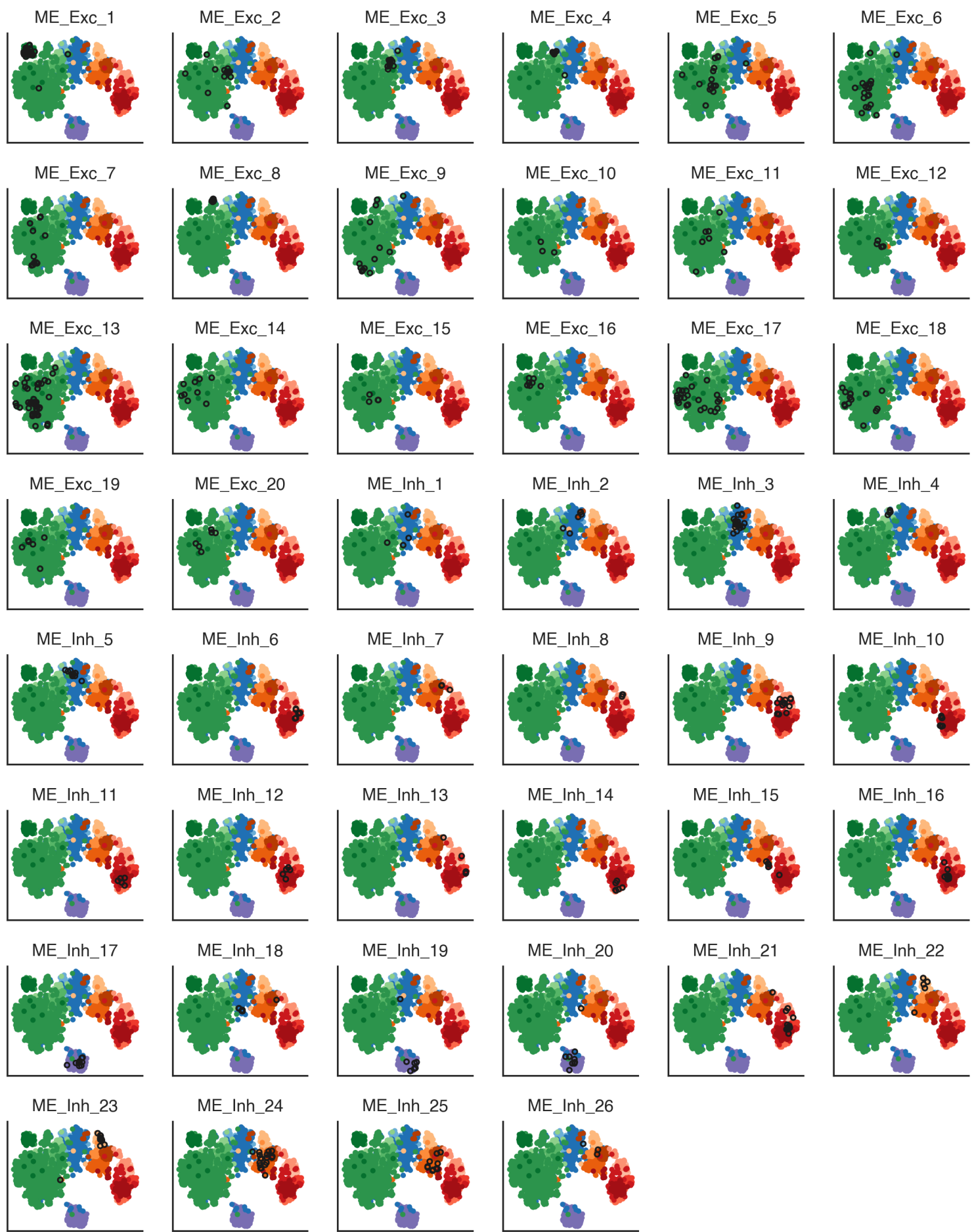
**Supplementary Figure 29: Comparison of e-types and m-types.** Fraction of cells from each m-type (rows) that fall into each e-type (columns). Dot size indicates the fraction of the row falling into a given column, and color indicates e-type.

Supplementary Figure 30



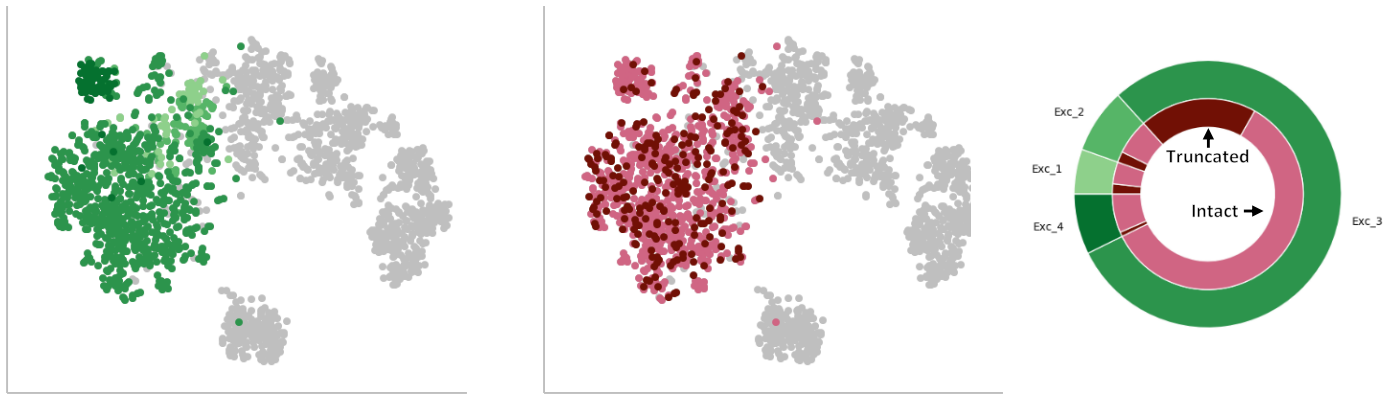
**Supplementary Figure 30: Prediction of me-types by electrophysiological and morphological features.** (a-f) Left: The top 10 features for predicting excitatory (a-c) and inhibitory (d-f) me-types as ranked by relative feature importance determined by a random forest classifier trained on all the features (a, d), only electrophysiological features (b, e), and only morphological features (c, f). Middle: Confusion matrix of actual me-types (rows) vs out-of-bag predictions (columns), grouped by putative transcriptomic subclass (see Fig. 6). Comparison of the classification errors reveals that different subclasses have me-types that are more distinguished by electrophysiological features vs morphological, and vice versa. Right: Prediction error rates between subclasses (filled bars) and within subclasses (hollow bars); note that subclasses with a single associated me-type (L2/3 IT, L5 CF, NP, L6b) do not have a value for within-subclass error rate. Overall, error rates were lower between subclasses vs within subclasses, though between-subclass rates were notably high when predicting excitatory me-types from electrophysiological features alone. IT: intratelencephalic, CF: corticofugal, NP: near-projecting, CT: corticothalamic.

Supplementary Figure 31

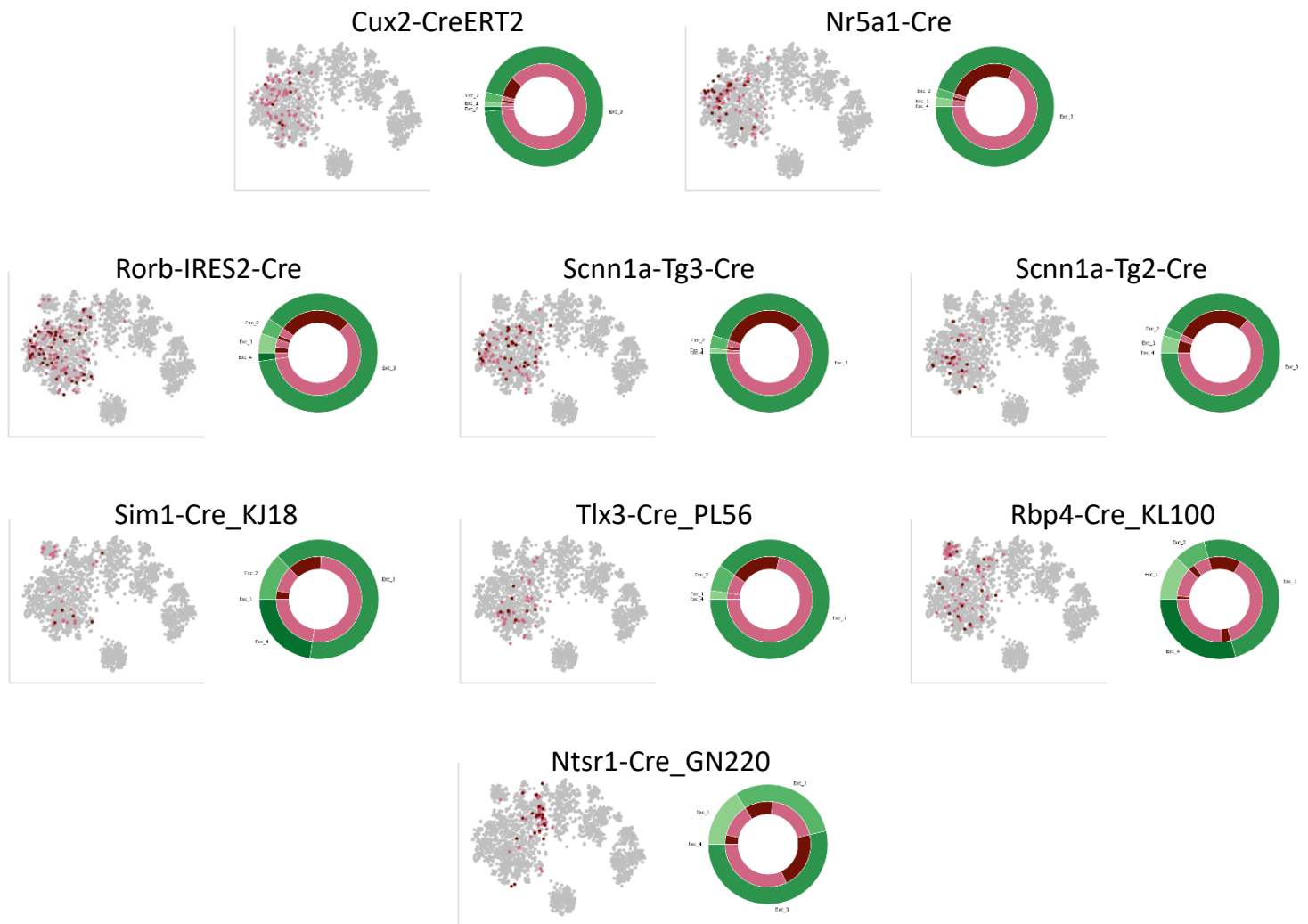


**Supplementary Figure 31: Locations of me-types on the electrophysiological projection.**  
Electrophysiology-based t-SNE plots ( $n = 1,938$  cells) with cells from different me-types highlighted. Colors indicate e-type labels (see Fig. 2). Cells with the indicated me-type are indicated with black circles.

### a. All spiny neurons

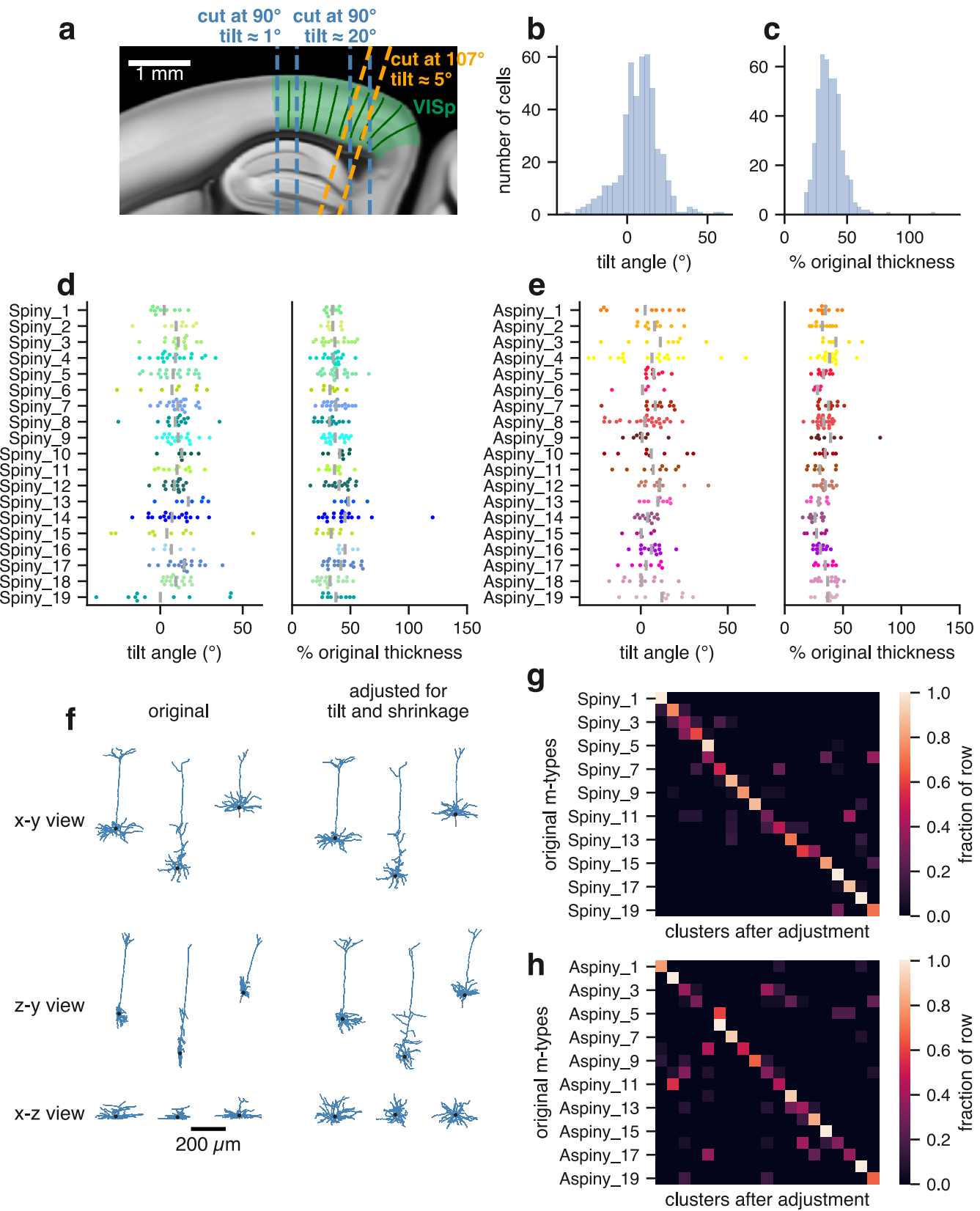


### b. Spiny neurons by Cre line



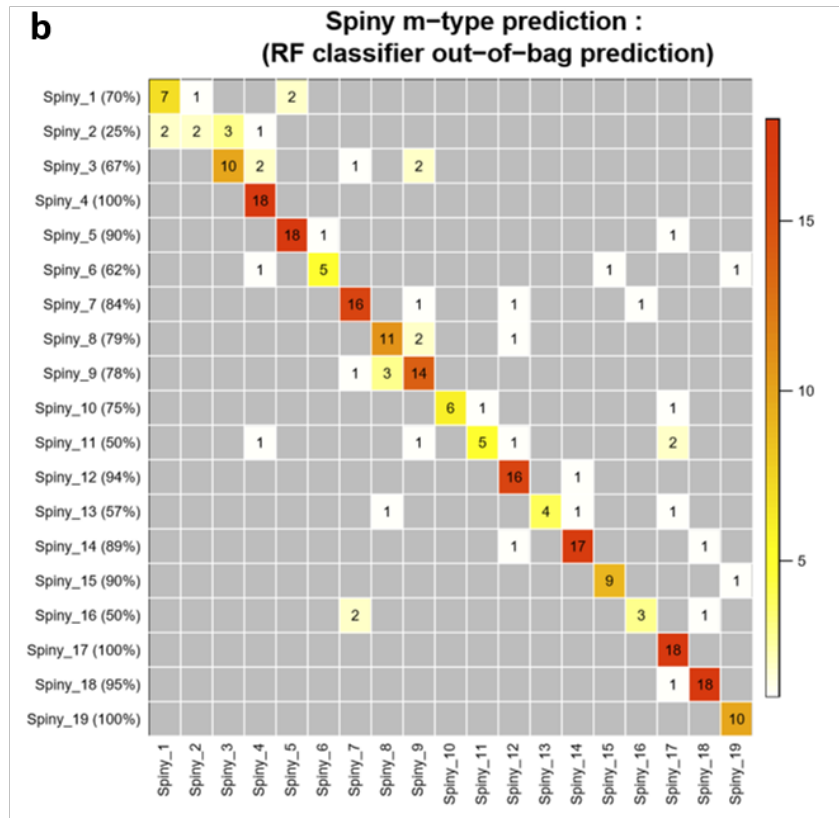
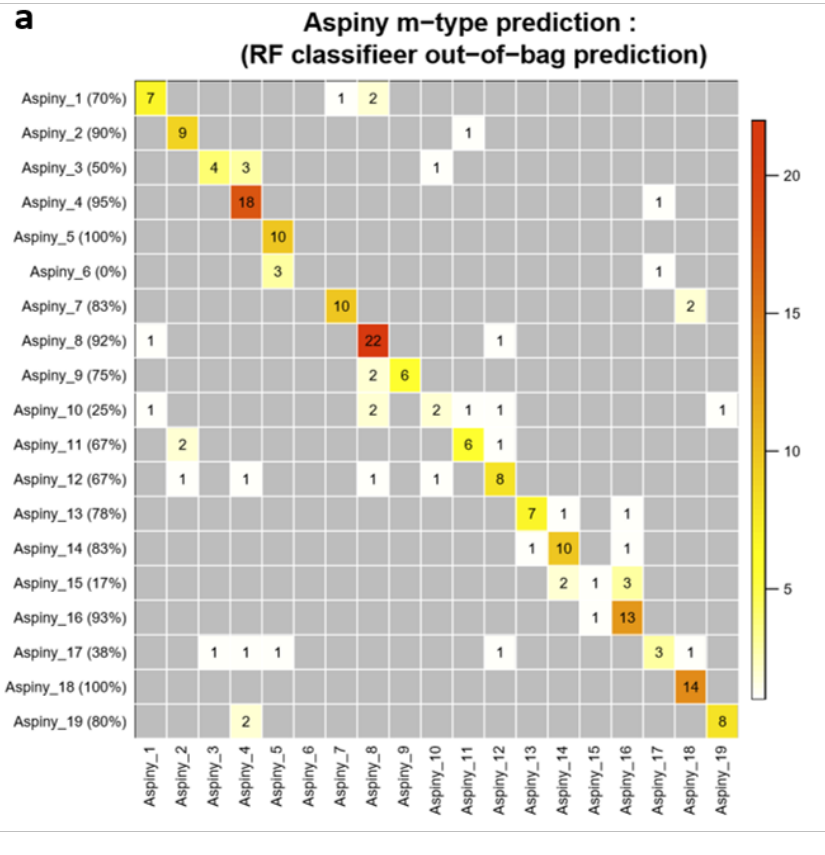
**Supplementary Figure 32: Effect of apical dendrite truncation on spiny neuron electrophysiology classification.** **(a)** Electrophysiology-based t-SNE plots ( $n = 1,938$  total cells, 928 excitatory cells highlighted) show distribution of electrophysiology types (left, green), and cells with their apical dendrite status indicated (center, truncated: dark red, intact: pink). The right shows the proportion of total spiny cells in each electrophysiology type (outer ring, green), as well as the fraction of each of those types that are made up of intact and truncated neurons (inner ring, red). Exc\_4 has the smallest fraction of truncated neurons (10%) vs 32%, 24%, and 25% for Exc\_1, Exc\_2, and Exc\_3 respectively. Also, the region of the t-SNE projection where Exc\_4 is primarily represented (top left), appears to have fewer truncated neurons than the rest of the electrophysiology space. **(b)** Electrophysiology-based t-SNE plots ( $n = 1,938$  cells) and electrophysiology and truncation proportions represented by each major spiny neuron transgenic line.

Supplementary Figure 33



**Supplementary Figure 33: Effect of slice angle and shrinkage on morphological classification.**

**(a)** Parasagittal schematic illustrating how slicing visual cortex leads to a variety of tilt angles between the cut surface of the slice (dashed lines) and the shortest paths between pia and white matter (green solid lines). Rostral direction is to the left. Cutting coronal sections (blue dashed lines) leads to small tilt angles at the rostral end of VISp (green shaded region) but larger ones toward the caudal end. Other slice angles were used (example of 107° shown by orange dashed lines) to reduce the tilt angle in slices toward the caudal end. **(b)** Distribution across reconstructed cells of tilt angles estimated by comparing the images of the slice to the Common Coordinate Framework reference, then calculating the angle between the cut surface and the path connecting pia to white matter at that location. Most cells were recorded from the rostral side of the slice; however, if a cell was recorded from the caudal side, the tilt angle was reversed for that cell. **(c)** Distribution across reconstructed cells of shrinkage in the z-direction (i.e., perpendicular to the cut plane) estimated by either comparing the depth of the soma from the cut surface during recording and after fixation and reconstruction, or by comparing the original slice thickness (350 µm) to the z-extent measured by imaging after fixation. **(d)** Distributions (dots) and averages (gray bars) of tilt angles (left) and shrinkage estimates (right) for each spiny m-type. **(e)** Same as **(d)** but for aspiny m-types. **(f)** Example spiny neuron reconstructions in the original state based directly on the imaged cell (left) and after adjusting the reconstructions for shrinkage and tilt angle (right). Three perspectives are shown to illustrate how the neurons become more radially symmetric after adjustment. Note (particularly in the z-y view) that there are processes cut off by slicing, and the cut is frequently not parallel to the pia-white matter direction. **(g)** Comparison of original spiny m-type classification (rows) and re-classification after adjusting for shrinkage and tilt (columns). **(h)** Same as **(g)** but for aspiny m-types.



**Supplementary Figure 34: Prediction of m-type by morphology features.** Two kinds of classifiers, random Forest (RF) and support vector machine (SVM), were built based on all morphology features. SVM classification gave 89/79% prediction accuracy in leave-one-out cross validation for spiny/aspyne neurons, respectively. RF classification provided 79/70% out-of-bag prediction accuracy. The accuracy for individual m-types is reported for **(a)** 19 aspyne/inhibitory types and **(b)** 19 spiny/excitatory types. 3 out of 4 neurons in the Aspyne\_6 cluster were predicted to be neighboring Aspyne\_5 m-type; both m-types contain chandelier cells.

**Supplementary Table 1. Electrophysiological data sets.**

Name	Description	Type	Sparse principal components used (exc. / inh. / all)
AP V <sub>m</sub>	V <sub>m</sub> of first AP from short pulse, long step, and ramp; includes 3 ms after AP threshold	Waveform	7 / 6 / 6
AP dV/dt	Time derivative of (1)	Waveform	8 / 8 / 8
ISI shape	Average of ISI voltage trajectories, aligned to the threshold of the initial AP and normalized in duration	Waveform	3 / 3 / 3
Subthr. (abs.)	Concatenated responses to hyperpolarizing current steps (from -10 pA to -90 pA)	Waveform; steps from -90 pA to -10 pA	2 / 2 / 2
Subthr. (norm.)	Response to largest amplitude hyperpolarizing current step, aligned to baseline membrane potential and normalized by maximum voltage deflection	Waveform	4 / 5 / 4
PSTH	AP counts in 50 ms bins, divided by bin width	Binned (50 ms); steps from rheobase to rheobase + 100 pA	6 / 6 / 6
Inst. firing rate	Instantaneous firing rate across long steps	Binned (20 ms); steps from rheobase to rheobase + 100 pA	6 / 5 / 5
Up/down	Upstroke/downstroke ratio across long steps	Binned (20 ms); steps from rheobase to rheobase + 100 pA	2 / 2 / 2
AP peak	AP peak across long steps	Binned (20 ms); steps from rheobase to rheobase + 100 pA	2 / 2 / 2
AP fast tr.	AP fast trough across long steps	Binned (20 ms); steps from rheobase to rheobase + 100 pA	2 / 2 / 2

AP thresh.	AP threshold across long steps	Binned (20 ms); steps from rheobase to rheobase + 100 pA	2 / 5 / 4
AP width	Width at half-height across long steps	Binned (20 ms); steps from rheobase to rheobase + 100 pA	3 / 2 / 2
Inst. freq. (norm.)	Instantaneous firing rate across long steps, normalized to maximum rate for each step	Binned (20 ms); steps from rheobase to rheobase + 100 pA	7 / 8 / 8

**Supplementary Table 2: Description of morphological features**

Note that here “y” is in the pia-to-white-matter direction, “x” is across the face of the slice, and “z” is into the slice. Units are indicated with parentheses; other features are unitless.

Feature Name	Feature Description
<b>Branching Pattern Features (calculated for all compartment types except where noted)</b>	
Height	Total extent in the y-direction ( $\mu\text{m}$ )
Width	Total extent in the x-direction ( $\mu\text{m}$ )
{x, y}-bias	Difference in extent in x or y in one direction from the soma and the other. Values are signed for y-bias and unsigned for x-bias. ( $\mu\text{m}$ )
Max. branch order	The maximum number of bifurcations encountered between the soma and all neurite tips
Max. Euclidean distance	The direct-line distance from the soma to the most distal node ( $\mu\text{m}$ )
Max. path distance	The path distance from the soma to the furthest neurite tip ( $\mu\text{m}$ )
Mean contraction	The average of the ratios of the summed euclidean distance between bifurcations, and between bifurcations and tips, to the summed path distance between same
Number of branches	The number of individual branches in the morphology
Number of outer bifurcations	The number of bifurcations found in the outer region of a tree, defined as outside a sphere with a radius of 50% the max. Euclidean distance. This feature was shifted by one and log-scaled for analysis. <i>Apical only</i>
Mean bifurcation distance	Average relative position of bifurcations projected to a line connecting the soma to the furthest node. <i>Apical only</i>
St. dev. bifurcation distance	Standard deviation of relative positions of bifurcations projected to a line connecting the soma to the furthest node. <i>Apical only</i>
Early branch	Ratio of the maximum length of all the “shorter” branches to the maximum path length. “Shorter” branches are defined as those with the smaller path length at each bifurcation. <i>Apical only</i>
Total length	The combined length of all branches ( $\mu\text{m}$ )

### **Stem Features**

---

Axon-soma distance	The path distance from the axon root to the soma surface ( $\mu\text{m}$ ). <i>Axon only</i>
Axon-soma theta	The relative radial position of the point where the neurite from which the axon derives exits the soma. <i>Axon only</i>
Number of stems	The number of stems sprouting from the soma. <i>Basal only</i>
Stem exit histogram (up/down/sides)	Normalized histogram of stem exit directions (defined by four quadrants). The side with more stems were aligned for each neuron to prevent "handedness." <i>Inhibitory basal only</i>

### **Overlap/Separation Features**

---

% above/overlap/below	% of nodes of a given compartment type above/overlapping/below the full y-extent of another compartment type
EMD	Earth mover's distance metric calculated between the normalized and aligned depth profile histograms of one compartment type and another

### **Location Features**

---

Relative soma depth	Distance between the pia and the soma, normalized by the distance between pia and white matter
---------------------	--

### **Profile Features**

---

Aligned histogram principal components (PCs)	Components that exceed 5% explained variance from PCA performed on a depth-wise compartment histogram where the depth of each layer has been aligned to the overall average (5 $\mu\text{m}$ bins). <i>Apical (5 components) and axon (6 components) only</i>
Soma {x, y}-percentile	Percentile location of the x- or y-coordinate of the soma within the distribution of all x- or y-coordinates of the compartment nodes. For x-percentiles, the results were symmetrized (ranging only from 0 to 0.5) to prevent "handedness"

**Supplementary Table 3: Comparison between me-types and existing literature.**

The me-types are ordered first by inferred transcriptomic subclass, then by number. IT: intratelencephalic, CF: corticofugal, NP: near-projecting, CT: corticothalamic, RS: regular spiking, FS: fast-spiking, AP: action potential, PC: principal cell,  $R_i$ : input resistance,  $\tau_m$ : membrane time constant.

	me-type	Inferred subclass	Description	Relationship to previously described types
1	<b>ME_Exc_7</b>	L2/3 IT	Wide, short L2/3; RS adapting	Pyramid-L2/3 <sup>5,6</sup> , pyramid L2/3 type I and type II <sup>7</sup>
2	<b>ME_Exc_14</b>	L4	Tufted (sparse) L4; RS adapting	Simple tufted <sup>7</sup>
3	<b>ME_Exc_15</b>	L4	Tufted (sparse) L4; RS adapting	Simple tufted <sup>7</sup>
4	<b>ME_Exc_16</b>	L4	Tufted & tufted (sparse) L4; RS adapting	Simple tufted <sup>7</sup> , slender tuft <sup>8</sup> , tall-simple <sup>7</sup> , L4 pyramidal cell <sup>5</sup>
5	<b>ME_Exc_17</b>	L4	Tufted (very sparse) L4; RS adapting	Simple tufted <sup>7</sup> ; pyramid <sup>9</sup>
6	<b>ME_Exc_18</b>	L4	Non-tufted L4; RS adapting	Star pyramid <sup>9</sup>
7	<b>ME_Exc_19</b>	L4	Stellate L4, L6 & non-tufted L4; RS adapting	Spiny stellate <sup>9</sup> , star pyramid <sup>9</sup>
8	<b>ME_Exc_20</b>	L4	Non-tufted L4; RS adapting & RS transient	Star pyramid <sup>9</sup>
9	<b>ME_Exc_5</b>	L5 IT	Tufted & non-tufted L5; RS adapting	Simple tufted <sup>7</sup> , slender tuft <sup>5,8</sup> , tall-simple <sup>7</sup> , tufted pyramid <sup>5</sup> , untufted pyramid <sup>5</sup>
10	<b>ME_Exc_12</b>	L5 IT	Tufted & tufted (large basal) L5; RS adapting	Simple tufted <sup>7</sup> , slender tuft <sup>8</sup> , tall-simple <sup>7</sup> , tufted pyramid <sup>5</sup>
11	<b>ME_Exc_13</b>	L5 IT	Tufted L5; RS adapting	Simple tufted <sup>7</sup> ; pyramid <sup>9</sup>
12	<b>ME_Exc_1</b>	L5 CF	Thick-tufted L5; RS low $R_i$ , sharp sag	Thick tufted <sup>5,6,10-12</sup> ; tall-tufted <sup>7</sup>
13	<b>ME_Exc_8</b>	NP	Tufted (sparse basal) L5; RS adapting (large sag)	L5 corticocortical, non-striatal/local pyramid <sup>13</sup>
14	<b>ME_Exc_6</b>	L6 IT	Wide, short L6a & tufted (large basal) L5; RS adapting	L6 corticocortical <sup>14</sup>
15	<b>ME_Exc_10</b>	L6 IT	Inverted L6a,b; RS adapting	Inverted pyramid <sup>5,14</sup>
16	<b>ME_Exc_11</b>	L6 IT	Inverted L6a,b; RS adapting	Inverted pyramid <sup>5,14</sup>
17	<b>ME_Exc_2</b>	L6 CT	Narrow L6a; RS adapting	L6 corticothalamic <sup>6,14,15</sup>
18	<b>ME_Exc_3</b>	L6 CT	Narrow L6a; RS transient/adapting	L6 corticothalamic <sup>6,14,15</sup>
19	<b>ME_Exc_4</b>	L6 CT	Narrow L6a; RS transient	L6 corticothalamic <sup>6,14,15</sup>

20	<b>ME_Exc_9</b>	L6b	Subplate L6b	Subplate <sup>14,16</sup>
21	<b>ME_Inh_15</b>	Sst	L1-innervating ascending axon L2/3, L4; mid-width AP adapting & FS pausing	Martinotti cells <sup>5,17-22</sup>
22	<b>ME_Inh_22</b>	Sst	Small axon, large dendrites L5, L6; irregular/adapting, long $\tau_m$	Non-Martinotti cells (long-range projecting) <sup>23</sup>
23	<b>ME_Inh_23</b>	Sst	Wide axon, large dendrites L5, L6; irregular/adapting, long $\tau_m$	Non-Martinotti cells (long-range projecting) <sup>23</sup>
24	<b>ME_Inh_24</b>	Sst	Large ascending axon L5, L6; mid-width AP adapting & transient	Martinotti cells <sup>5,17-22,24</sup>
25	<b>ME_Inh_25</b>	Sst	L1-innervating ascending axon L2/3, L4 & ascending large axon L5; mid-width AP adapting	Martinotti cells <sup>5,17-22,24</sup>
26	<b>ME_Inh_26</b>	Sst	Ascending small axon L5, L4; mid-width AP transient/irregular	Martinotti and non-Martinotti cells <sup>5,17-22,24</sup>
27	<b>ME_Inh_6</b>	Pvalb	Wide axon, large dendrites L6; FS transient & sustained	Basket cells <sup>5,20,23,25</sup>
28	<b>ME_Inh_7</b>	Pvalb	Wide axon, large dendrites L6; FS transient	Basket cells <sup>5,20,23,25</sup>
29	<b>ME_Inh_8</b>	Pvalb	Dense axon, intersecting dendrites L5, L4; FS transient	Basket cells <sup>5,20,23,25</sup>
30	<b>ME_Inh_9</b>	Pvalb	Ascending axon L5, L6; FS transient & pausing	Basket cells <sup>5,20,23,25,26</sup>
31	<b>ME_Inh_10</b>	Pvalb	Ascending axon; FS delayed & sustained	Basket cells <sup>5,20,23,25</sup>
32	<b>ME_Inh_11</b>	Pvalb	Ascending axon L5, L6; FS delayed/pausing	Basket cells <sup>5,20,23,25,26</sup>
33	<b>ME_Inh_12</b>	Pvalb	Small axon, intersecting dendrites; FS delayed/pausing	Basket cells <sup>5,20,23,25</sup>
34	<b>ME_Inh_13</b>	Pvalb	Ascending small axon L5, L4; FS transient & sustained	Basket cells <sup>5,20,23,25</sup>
35	<b>ME_Inh_14</b>	Pvalb	Dense axon, intersecting dendrites L4, L2/3; FS	Basket cells <sup>5,20,23,25</sup>

			sustained & delayed/pausing	
36	<b>ME_Inh_16</b>	Pvalb	Descending dense, wide axon L2/3; FS delayed/pausing	Basket cells <sup>5,20,23,25</sup>
37	<b>ME_Inh_21</b>	Pvalb	Descending axon, small juxtaposed dendrites L2/3; FS transient, sustained, & delayed/pausing	Chandelier cells, axo-axonic cells <sup>5,18,20,23,25,27,28</sup>
38	<b>ME_Inh_17</b>	Lamp5	Dense axon, small dendrites L1; RS non- adapting, delayed	Neurogliaform cell <sup>5,20,29,30</sup>
39	<b>ME_Inh_18</b>	Lamp5	Dense axon, large dendrites L1; irregular	Neurogliaform cell <sup>5,20,29,30</sup>
40	<b>ME_Inh_19</b>	Lamp5	Dense axon, small dendrites L6; RS non- adapting, delayed	Neurogliaform cell <sup>5,20,29,30</sup>
41	<b>ME_Inh_20</b>	Lamp5	Dense axon, small dendrites L2/3, L4; RS non- adapting, delayed	Neurogliaform cell <sup>5,20,29,30</sup>
42	<b>ME_Inh_1</b>	Vip	Descending axon, bidirectional dendrites L2/3, L4; irregular/sustained	Bipolar cell, bitufted cell, double bouquet cell, horsetail cell <sup>5,19– 21,31,32</sup>
43	<b>ME_Inh_2</b>	Vip	Descending axon, bidirectional dendrites L2/3; transient & irregular, sharp sag	Bipolar cell, bitufted cell, double bouquet cell <sup>5,19–21,31,32</sup>
44	<b>ME_Inh_3</b>	Vip	Descending axon, bidirectional dendrites; irregular	Bipolar cell, bitufted cell, double bouquet cell <sup>5,19–21,31,32</sup>
45	<b>ME_Inh_4</b>	Vip	Descending axon, bidirectional dendrites L2/3, L4; transient	Bipolar cell, bitufted cell, double bouquet cell <sup>5,19–21,31,32</sup>
46	<b>ME_Inh_5</b>	Vip	Descending axon, bidirectional dendrites L2/3; irregular	Bipolar cell, bitufted cell, double bouquet cell <sup>5,19–21,31,32</sup>

## a. Aspiny m-types

feature name	Gini index
soma relative depth	12.36
axon hist pc 1	11.54
axon hist pc 0	9.71
axon bias y	8.24
axon emd with dendrite	8.17
axon hist pc 2	6.81
axon soma percentile y	6.22
dendrite bias y	6.09
axon hist pc 3	6.02
axon hist pc 4	5.93
axon pct above dendrite	5.36
axon pct intersect dendrite	5.2
dendrite pct above axon	4.95
dendrite extent y	4.89
dendrite pct intersect axon	4.85
axon num branches	4.74
axon max euclidean distance	4.63
dendrite max euclidean distance	4.6
axon total length	4.57
axon extent x	4.52
axon hist pc 5	4.41
axon pct below dendrite	4.03
axon extent y	3.99
dendrite soma percentile y	3.48
dendrite extent x	3.46
dendrite num stems	3.03
axon contraction	2.96
axon soma theta	2.96
dendrite contraction	2.94
axon max path distance	2.86
dendrite bias x	2.69
dendrite stem exit side more	2.69
dendrite total length	2.41
axon soma percentile x	2.38
dendrite stem exit up	2.37
axon max branch order	2.36
dendrite pct below axon	2.33
dendrite num branches	2.16
axon soma distance	2.15
axon bias x	1.91
dendrite soma percentile x	1.88
dendrite stem exit down	1.86
dendrite stem exit side less	1.33
dendrite max branch order	1.28

## b. Spiny m-types

feature name	Gini index
soma relative depth	19.32
apical dendrite bias y	14.36
apical dendrite extent y	14.18
apical dendrite total length	12.48
apical dendrite std bifurcation distance	11.38
apical dendrite hist pc 0	10.81
dendrite emd with apical dendrite	10.03
apical dendrite hist pc 1	9.65
apical dendrite mean bifurcation distance	9.35
apical dendrite pct above dendrite	8.77
apical dendrite num branches	7.78
dendrite pct below apical dendrite	7.55
apical dendrite early branch	7.46
dendrite pct intersect apical dendrite	6.99
apical dendrite num outer bifurcations	6.93
dendrite num branches	6.34
apical dendrite pct intersect dendrite	6.25
apical dendrite hist pc 4	6.04
dendrite total length	5.38
apical dendrite max branch order	5.3
apical dendrite soma percentile y	5.19
apical dendrite hist pc 2	4.95
apical dendrite hist pc 3	4.51
dendrite max euclidean distance	4.22
dendrite extent y	3.55
dendrite extent x	2.86
apical dendrite extent x	2.78
apical dendrite bias x	2.77
dendrite contraction	2.76
dendrite soma percentile y	2.56
apical dendrite pct below dendrite	2.37
apical dendrite contraction	2.26
dendrite bias y	2.23
apical dendrite soma percentile x	2.06
dendrite bias x	1.79
dendrite num stems	1.59
dendrite soma percentile x	1.36
dendrite pct above apical dendrite	1.13
dendrite max branch order	0.64

**Supplementary Table 4: Feature importance for m-type prediction.** The importance of each morphological feature was assessed by training a random forest classifier to predict m-types. The feature importance is characterized in terms of Gini index (higher values have greater importance).

## **Supplementary Note**

### **Description of morpho-electrical (me) types and comparison with prior cell type studies**

#### *Excitatory neuron me-types*

We assessed the electrophysiological and morphological properties of the me-types derived from our study and correlated them with prior cell type knowledge (Supplementary Table 4). For excitatory me-types, the majority of neurons had similar electrophysiological properties (see Exc\_3 “RS adapt.”, Fig. 2) with distinct morphological properties across the cortical layers. We identified a single L2/3 me-type (ME\_Exc\_7), which had a short, widely branching apical dendrite (m-types Spiny\_1,2, Fig. 3). Similar neurons have been described as Type I and II neurons in rat somatosensory cortex<sup>7</sup>.

Seven L4 me-types were identified in this study; we note that we heavily sampled L4 (34.3% of reconstructed spiny neurons) as this layer had previously received relatively little attention in mouse VISp. The me-types ME\_Exc\_14 to 17 had apical dendrites that were relatively unbranched in L2/3 and ended with a tuft of dendritic branches in L1; they were distinguished between each other by varying degrees of apical tuftedness (m-types 3,4,7,8, Fig. 3). ME\_Exc\_18 and 20 neurons had a star pyramid morphology<sup>5,6,33,34</sup> characterized by the absence of a L1 tuft (m-type Spiny\_5). ME\_Exc\_19 neurons lacked a pronounced apical dendrite and most closely resembled spiny stellates, which have profuse spines and a very short apical dendrite. Spiny stellates are found in abundance in primary visual cortex in the cat and primate<sup>35,36</sup>, and primary somatosensory cortex in rat where they are the main L4 excitatory m-type<sup>37</sup>. However, we found only a small number of them in mouse VISp, which agrees with previous findings in mouse and rat visual cortex<sup>34,38</sup>. These cells were primarily in L4, but examples were also found in L2/3 and 6 (Supplementary Fig. 28).

Five L5 me-types were identified and associated with three transcriptomic subclasses. The L5 IT me-types ME\_Exc\_5, 12, and 13 resemble what has been previously described as layer 5 subgroup 1B neurons in mouse visual cortex<sup>11</sup> and tall-simple<sup>7</sup> and slender tufted<sup>5,6</sup> neurons in mouse and rat somatosensory cortex, respectively (m-types Spiny\_9 and 12, Fig. 3). The L5 CF me-type (ME\_Exc\_1) had electrophysiological and morphological properties distinct from the L5 IT me-types. ME\_Exc\_1 was closely associated with the Exc\_4 e-type (see Fig. 5c), which had low input resistance, sharp sag, and displayed the most prominent bursting behavior (Supplementary Fig. 9) among excitatory e-types. These neurons had a larger number of branches and increased apical tuft width, often described as thick tufted neurons<sup>5-7,11,12</sup> (m-types Spiny\_13, 14). The L5 NP me-type (ME\_Exc\_8) was distinguished from other tufted L5 me-types by long, sparse basal dendrites. These neurons, labeled in the Slc17a8-Cre line, are likely the recently described local, non-striatal projecting neurons<sup>13</sup>. These neurons have not been described in other large-scale studies of excitatory cortical diversity in rat<sup>5,6</sup> and may be a unique cell type in mouse cortex. Although they were not associated with a unique e-type, ME\_Exc\_8 cells were found near each other on an island in the electrophysiology-based t-SNE projection (Fig. 6e, Supplementary Fig. 31), indicating high consistency within this type and some distinctiveness compared to other excitatory cells.

In L6, we identified seven me-types. The three L6 CT-associated me-types (ME\_Exc\_2, 3, and 4), were often labeled by Ntsr1-Cre (Supplementary Fig. 27) and found predominantly in

L6a. The three types were each associated with a different e-type (see Fig. 5c); ME\_Exc\_3 and 4 had majorities of cells from e-types Exc\_2 and 1, respectively, which had transient or strongly adapting firing (Supplementary Fig. 11). Neurons in these three me-types had narrow dendritic profiles that ended in L1 (ME\_Exc\_2 and 3) or L2/3 (ME\_Exc\_4). This dendritic phenotype (m-type Spiny\_18, Fig. 3) matched that described for Ntsr1+ neurons that project to the thalamus<sup>14,26</sup>. The L6 IT-associated types (ME\_Exc\_6, 10, and 11) had relatively short apical dendrites with a large width-to-height ratio. ME\_Exc\_6 had apical dendrites oriented to the pia (m-type Spiny\_17). ME\_Exc\_10 and 11 neurons had apical dendrites oriented toward the white matter, often called inverted pyramids<sup>5,14</sup>. These me-types were enriched in the Penk-Cre line (Supplementary Fig. 27) and resembled the short, wide branching cortico-cortical projecting neurons<sup>14</sup> (m-type Spiny\_15, Fig. 3). There was one L6b me-type (ME\_Exc\_9). These neurons, frequently labeled by the Ctgf line (Supplementary Fig. 27) have been previously described as “subplate” neurons with short, irregularly oriented apical dendrites<sup>16</sup> (m-type Spiny\_19, Fig. 3).

#### *Inhibitory neuron me-types*

Among the inhibitory me-types, we found six types associated with the Sst transcriptomic subclass (ME\_Inh\_15, 22 to 26). Four of these (ME\_inh\_15, ME\_Inh\_24 to 26) had ascending axons that frequently innervated L1, characteristic of Martinotti cells<sup>21,22,24</sup>, and were found in L2/3 to L6. These neurons had adapting, transient, or irregular firing and had APs wider than Pvalb-associated types but narrower than other interneurons. ME\_Inh\_24 contained more T-shaped Martinotti and non-Martinotti cells, while ME\_Inh\_25 had more “fanning out” morphologies, which have been proposed to have different roles in sensory processing<sup>17</sup>. ME\_Inh\_22 and 23 were primarily found in L5-L6 (Supplementary Fig. 28) and had non-Martinotti morphologies. They exhibited adapting or irregular firing with long membrane time constants and little sag (see Inh\_4, Fig. 2) and had wider APs than other Sst me-types. These cells were mostly labeled by an Sst/Nos1 intersectional strategy, which suggests they are likely long-range projecting GABAergic interneurons<sup>1,18,39,40</sup> (see also Fig. 7h).

All eleven me-types associated with the Pvalb subclass (ME\_Inh\_6 to 14, 16, and 21) exhibited fast-spiking (FS) firing characteristics, with narrow APs, steep f-I curves, and little firing-rate adaptation. With their large boutons and unique cartridge-like axon structure, chandelier cells (ChCs) are some of the most reliably expert-identified inhibitory neurons<sup>19</sup>, and the ME\_Inh\_21 can be clearly identified as ChCs here with minimally branched, L1-restricted dendrites and highly branched, L2/3-restricted axons. ChCs with a single axon branch that traveled beyond the main axon bundle down to layer 4/5 were found in this type as well; though this morphology has been observed before<sup>25,27</sup>, it has not been described for mouse visual cortex. Many of the other Pvalb me-types had basket-cell-like morphologies (multipolar dendrites overlapping with a relatively small axon cluster) with laminar biases across the me-types (Supplementary Fig. 28). We also noted that transient firing at lower stimulus amplitudes appeared more common in me-types biased toward deeper layers. Some of the deeper me-types (e.g., ME\_Inh\_9) contained neurons with a larger ascending axon spanning multiple layers, resembling fast-spiking translaminar cells described previously in mouse visual cortex<sup>26</sup>.

The four Lamp5-associated me-types (ME\_Inh\_17 to 20) exhibited small, dense multipolar dendrites and highly branched axons, described previously as neurogliaform cells (NGCs)<sup>20,23,29,32</sup>. They were strongly tied to specific cortical layers, with ME\_Inh\_17 and 18 in L1,

ME\_Inh\_20 in L2/3, and ME\_Inh\_19 in L6. The two L1 me-types had different electrophysiological properties. While cells in ME\_Inh\_17 all had the Inh\_1 e-type, with long delays in firing at amplitudes near rheobase (Supplementary Fig. 8) and little firing-rate adaptation (Supplementary Fig. 11), ME\_Inh\_18 cells had the Inh\_3 e-type (shared with Vip cells) with less regular firing. ME\_Inh\_19 and 20 neurons also primarily had the Inh\_1 e-type (see Fig. 5d).

There were five me-types linked to the Vip subclass (ME\_Inh\_1 to 5). These neurons most closely resembled neurons previously described as bipolar, bitufted, small basket or double bouquet cells<sup>20,31,32</sup> due to a small number of bidirectionally-oriented primary dendrites and a sparse, mainly descending, axon. Most cells were found in L1 through L4 (Supplementary Fig. 28). We note that single bouquet cells were not observed in L1 for this study, though they had been previously described in mouse VISp<sup>20</sup>. ME\_Inh\_3 appeared to be enriched for small basket cell-like Vip+ neurons with wider axons and multipolar dendrites, while ME\_Inh\_5 was enriched for cells with a narrow axon profile more similar to bipolar cells, though the neurons often had more than two primary dendrites<sup>18</sup>. Neurons in these me-types had relatively wide APs compared to other interneurons and fired transiently or irregularly. ME\_Inh\_2 and 4 had higher proportions of transient cells than the other three, and the former had more pronounced sag during hyperpolarizing steps than the latter.

## REFERENCES

1. Tasic, B. *et al.* Shared and distinct transcriptomic cell types across neocortical areas. *Nature* **563**, 72–78 (2018).
2. Oh, S. W. *et al.* A mesoscale connectome of the mouse brain. *Nature* **508**, 207–214 (2014).
3. Langfelder, P., Zhang, B. & Horvath, S. Defining clusters from a hierarchical cluster tree: the Dynamic Tree Cut package for R. *Bioinformatics* **24**, 719–720 (2008).
4. Boldog, E. *et al.* Transcriptomic and morphophysiological evidence for a specialized human cortical GABAergic cell type. *Nat. Neurosci.* **21**, 1185–1195 (2018).
5. Markram, H. *et al.* Reconstruction and Simulation of Neocortical Microcircuitry. *Cell* **163**, 456–492 (2015).
6. Oberlaender, M. *et al.* Cell Type–Specific Three-Dimensional Structure of Thalamocortical Circuits in a Column of Rat Vibrissal Cortex. *Cereb. Cortex* **22**, 2375–2391 (2012).
7. Larsen, D. D. & Callaway, E. M. Development of layer-specific axonal arborizations in mouse primary somatosensory cortex. *J. Comp. Neurol.* **494**, 398–414 (2006).
8. Oberlaender, M. *et al.* Three-dimensional axon morphologies of individual layer 5 neurons indicate cell type-specific intracortical pathways for whisker motion and touch. *Proc. Natl. Acad. Sci. U. S. A.* **108**, 4188–93 (2011).
9. Staiger, J. F. *et al.* Functional Diversity of Layer IV Spiny Neurons in Rat Somatosensory Cortex: Quantitative Morphology of Electrophysiologically Characterized and Biocytin Labeled Cells. *Cereb. Cortex* **14**, 690–701 (2004).
10. Hattox, A. M. & Nelson, S. B. Layer V Neurons in Mouse Cortex Projecting to Different Targets Have Distinct Physiological Properties. *J. Neurophysiol.* **98**, 3330–3340 (2007).
11. Tsiola, A., Hamzei-Sichani, F., Peterlin, Z. & Yuste, R. Quantitative morphologic classification of layer 5 neurons from mouse primary visual cortex. *J. Comp. Neurol.* **461**, 415–428 (2003).
12. Economo, M. N. *et al.* Distinct descending motor cortex pathways and their roles in movement. *Nature* **563**, 79–84 (2018).
13. Kim, E. J., Juavinett, A. L., Kyubwa, E. M., Jacobs, M. W. & Callaway, E. M. Three Types of Cortical Layer 5 Neurons That Differ in Brain-wide Connectivity and Function. *Neuron* **88**, 1253–1267 (2015).
14. Vélez-Fort, M. *et al.* The Stimulus Selectivity and Connectivity of Layer Six Principal Cells Reveals Cortical Microcircuits Underlying Visual Processing. *Neuron* **83**, 1431–1443 (2014).
15. Olsen, S. R., Bortone, D. S., Adesnik, H. & Scanziani, M. Gain control by layer six in cortical circuits of vision. *Nature* **483**, 47–52 (2012).
16. Marx, M. & Feldmeyer, D. Morphology and Physiology of Excitatory Neurons in Layer 6b of the Somatosensory Rat Barrel Cortex. *Cereb. Cortex* **23**, 2803–2817 (2013).
17. Muñoz, W., Tremblay, R., Levenstein, D. & Rudy, B. Layer-specific modulation of neocortical dendritic inhibition during active wakefulness. *Science* **355**, 954–959 (2017).
18. He, M. *et al.* Strategies and Tools for Combinatorial Targeting of GABAergic Neurons in Mouse Cerebral Cortex. *Neuron* **92**, 555 (2016).
19. DeFelipe, J. *et al.* New insights into the classification and nomenclature of cortical

- GABAergic interneurons. *Nat. Rev. Neurosci.* **14**, 202–216 (2013).
- 20. Jiang, X. *et al.* Principles of connectivity among morphologically defined cell types in adult neocortex. *Science* **350**, aac9462 (2015).
  - 21. Kawaguchi, Y. & Kubota, Y. Physiological and morphological identification of somatostatin- or vasoactive intestinal polypeptide-containing cells among GABAergic cell subtypes in rat frontal cortex. *J. Neurosci.* **16**, 2701–15 (1996).
  - 22. Wang, Y. *et al.* Anatomical, physiological and molecular properties of Martinotti cells in the somatosensory cortex of the juvenile rat. *J. Physiol.* **561**, 65–90 (2004).
  - 23. Tremblay, R., Lee, S. & Rudy, B. GABAergic Interneurons in the Neocortex: From Cellular Properties to Circuits. *Neuron* **91**, 260–292 (2016).
  - 24. McGarry, L. M. *et al.* Quantitative classification of somatostatin-positive neocortical interneurons identifies three interneuron subtypes. *Front. Neural Circuits* **4**, 12 (2010).
  - 25. Woodruff, A. R., Anderson, S. A. & Yuste, R. The Enigmatic Function of Chandelier Cells. *Front. Neurosci.* **4**, 201 (2010).
  - 26. Bortone, D. S., Olsen, S. R. & Scanziani, M. Translaminar Inhibitory Cells Recruited by Layer 6 Corticothalamic Neurons Suppress Visual Cortex. *Neuron* **82**, 474–485 (2014).
  - 27. Miyamae, T., Chen, K., Lewis, D. A. & Gonzalez-Burgos, G. Distinct Physiological Maturation of Parvalbumin-Positive Neuron Subtypes in Mouse Prefrontal Cortex. *J. Neurosci.* **37**, 4883–4902 (2017).
  - 28. Somogyi, P. *et al.* Identified axo-axonic cells are immunoreactive for GABA in the hippocampus and visual cortex of the cat. *Brain Res.* **332**, 143–9 (1985).
  - 29. Jiang, X., Wang, G., Lee, A. J., Stornetta, R. L. & Zhu, J. J. The organization of two new cortical interneuronal circuits. *Nat. Neurosci.* **16**, 210–218 (2013).
  - 30. Ascoli, G. A. *et al.* Petilla terminology: nomenclature of features of GABAergic interneurons of the cerebral cortex. *Nat. Rev. Neurosci.* **9**, 557–568 (2008).
  - 31. Prönneke, A. *et al.* Characterizing VIP Neurons in the Barrel Cortex of VIPcre/tdTomato Mice Reveals Layer-Specific Differences. *Cereb. Cortex* **25**, 4854–4868 (2015).
  - 32. Kubota, Y. *et al.* Selective Coexpression of Multiple Chemical Markers Defines Discrete Populations of Neocortical GABAergic Neurons. *Cereb. Cortex* **21**, 1803–1817 (2011).
  - 33. Schubert, D., Kötter, R., Zilles, K., Luhmann, H. J. & Staiger, J. F. Cell Type-Specific Circuits of Cortical Layer IV Spiny Neurons. *J. Neurosci.* **23**, 2961–2970 (2003).
  - 34. Peters, A. & Kara, D. A. The neuronal composition of area 17 of rat visual cortex. I. The pyramidal cells. *J. Comp. Neurol.* **234**, 218–241 (1985).
  - 35. Anderson, J. C., Douglas, R. J., Martin, K. A. C. & Nelson, J. C. Synaptic output of physiologically identified spiny stellate neurons in cat visual cortex. *J. Comp. Neurol.* **341**, 16–24 (1994).
  - 36. Yabuta, N. H., Sawatari, A. & Callaway, E. M. Two functional channels from primary visual cortex to dorsal visual cortical areas. *Science* **292**, 297–300 (2001).
  - 37. Narayanan, R. T., Udvary, D. & Oberlaender, M. Cell Type-Specific Structural Organization of the Six Layers in Rat Barrel Cortex. *Front. Neuroanat.* **11**, 91 (2017).
  - 38. Xu, X. *et al.* Primary visual cortex shows laminar-specific and balanced circuit organization of excitatory and inhibitory synaptic connectivity. *J. Physiol.* **594**, 1891–1910 (2016).
  - 39. Paul, A. *et al.* Transcriptional Architecture of Synaptic Communication Delineates

- GABAergic Neuron Identity. *Cell* **171**, 522–539.e20 (2017).
40. Tasic, B. *et al.* Adult mouse cortical cell taxonomy revealed by single cell transcriptomics. *Nat. Neurosci.* **19**, 335–346 (2016).